Development and uncertainty characterization of 3D particle location from refocused and perspective shifted plenoptic images

by

Elise Munz Hall

A dissertation submitted to the Graduate Faculty of
Auburn University
in partial fulfillment of the
requirements for the Degree of
Doctor of Philosophy

Auburn, Alabama
August 3, 2019

Keywords: plenoptic camera, light field imaging, particle tracking, optical diagnostics, explosion analysis

Approved by

Brian S. Thurow, Chair, W. Allen and Martha Reed Professor of Aerospace Engineering
Dudley S. Nichols, Assistant Professor of Aerospace Engineering
David E. Scarborough, Assistant Professor of Aerospace Engineering
Stanley J. Reeves, Professor of Electrical Engineering
Daniel R. Guildenbecher, Principal Member of the Technical Staff, Sandia National Laboratories

Abstract

In recent years, the development of non-invasive 3D diagnostics has become a significant area of research due to the wide variety of available techniques and the multitude of engineering problems that benefit from these measurements. This dissertation is motivated by the need to measure explosively generated fragment fields in 3D and utilizes a plenoptic camera to measure fragment or particle characteristics. Plenoptic imaging is an implementation of light field imaging in which a camera is modified by the insertion of a microlens array between the main lens and the image sensor which allows instantaneous collection of 3D data from a single snapshot by extracting the volumetric information in post-processing.

This work details the development of algorithms to determine 3D position and in-plane size and shape of particles by exploiting the refocusing and perspective shift capabilities of a plenoptic camera. These algorithms are validated using a large experimental data set in which a static particle field is translated to provide known depth displacements at varied magnification and object distances. Examination of these results to determine quantitative measures of uncertainty indicates improved accuracy and precision is achieved through the use of perspective shifting as compared to the refocusing based method at significantly reduced computational costs. The perspective shift method is further applied to fragment localization and sizing in a lab scale fragmenting explosive and measurement of the secondary droplet field created by the impact of a drop of water on a thin film of water. In tandem with the development of these particle location algorithms a method of volumetric calibration of a plenoptic camera is implemented and tested.

Acknowledgments

Though only my name is listed as the author, this dissertation could not have been completed without the guidance, input, and support of many others. I am tremendously grateful for them all and especially those listed below.

Thank you to my advisor, Dr. Brian Thurow for everything you have taught me over the course of my collegiate education from early undergraduate classes to research guidance. In particular, thank you for your emphasis on technical communication and presentation skills, the development of which has always been difficult for me. Thank you for the opportunities to teach, attend conferences, and participate in extracurriculars which has allowed me to learn so much more than what falls in curriculum checkboxes.

Thank you to Dr. Daniel Guildenbecher for your hands-on guidance throughout my graduate career and for providing an example of excellence in research. Thank you for allowing me to work in your lab over the last four years and especially for the opportunity to continue to do so as a postdoc. Likewise, thank you to the rest of the 865 crew for your patience, humor, and welcoming attitudes during my time as an intern, I look forward to seeing you all soon.

Thank you to Dr. Stanley Reeves for eliminating my fear of electrical engineering through some of my favorite classes, which have been foundational to my research. Thank you to Dr. David Scarborough and Dr. Stephen Nichols for your input throughout my PhD and to all of you for serving on my PhD committee. Thank you to Dr. Edward Thomas for serving as my University Reader and for keeping Taylor in line over on the other side of campus.

Thank you to the AFDL past and present for your support, guidance, and friendship. Thank you to Dr. Tim Fahringer for holding in the eye rolls, teaching me to code, and running a 5K once. Thank you to Kyle Johnson for teaching me to teach and listening to my endless complaints. Thank you to you both for providing me footsteps to follow throughout grad school. Thank you to Dr. Chris Clifford for invaluable technical discussions and guidance. Thank you to Jeffrey Bolan for creating LFIT and providing an example of PowerPoint wizardry I will always strive to achieve. Thank you to Jenna Klemkowsky Davis for being my officemate, travel buddy, confidant, and best friend throughout grad school.

Thank you to my siblings, Bryce, Karlyle, and Siena Munz, for coming to Auburn and living across the street. I have been so fortunate to share my college experience with you. Thank you to my parents, Dr. Lida Munz and Larry Munz, for your support and patience throughout my life and of my education. You are best role models I could ask for in all aspects of your lives and I strive toward your examples of selflessness. Thank you to my husband, Taylor Hall, for your encouragement, unwavering support, and endless effort. Thank you to all of my family for serving as a constant reminder and example of the important things in life.

Funding

Sandia National Laboratories is a multimission laboratory managed and operated by National Technology and Engineering Solutions of Sandia, LLC, a wholly owned subsidiary of Honeywell International Inc., for the U.S. Department of Energy's National Nuclear Security Administration under contract DE-NA0003525.

Table of Contents

List of Tables

List of Figures

List of Abbreviations

f	main lens focal length
l_i	image distance
l_i'	object distance
l_o	virtual image distance
l_o'	virtual object distance
L	light field
L'	virtual light field
M	nominal magnification
M_e	effective magnification
mm	millimeters
nm	nanometers
(u,v)	aperture plane light field coordinates
(s,t)	microlens plane light field coordinates
(s_m,t_m)	measured microlens plane light field coordinates
(s_c,t_c)	calculated microlens plane light field coordinates
(x,y,z)	object space coordinates
α	ratio of virtual image distance to image distance
μm	microns
μs	microseconds
AFDL	Advanced Flow Diagnostics Laboratory

DOF	Depth of Field
DIH	Digital In-line Holography
DLFC	Direct Light Field Calibration
LFIT	Light Field Imaging Toolkit
VDW	Volumetric Dewarping
PIV	Particle Image Velocimetry
PTV	Particle Tracking Velocimetry
RMSE	root mean square error
2D	two-dimensional
3D	three-dimensional
4D	four-dimensional

I. Introduction and motivation

In recent years, research interest in the development of non-invasive, instantaneous diagnostic techniques for three-dimensional (3D) measurements of fragment fields has increased for a wide variety of applications. This dissertation is specifically motivated by the need for measurements of explosively generated fragments, though similar applications exist in the measurement of sprays such as those found in fuel injection systems and even in the analysis of debris fragments generated by natural events like hurricanes. The instantaneous and random nature of these events results in a small window of time in which a large amount of information is available. The ability to gather as much detailed information about these fragments as possible in 3D is a critical component of understanding these phenomena toward the specific goal of explosion mitigation. To design effective containment structures and materials, engineers need all available information about the expected size, shape, and velocity of the fragments generated by an explosion.

Several challenges exist in the measurement of these 3D fragment fields using currently available diagnostic tools. First, the arrangement of the fragments is unknown and in the collection of optical measurements from a single viewing angle, some fragments may be obscured; the magnitude of this problem increases with dense fragment fields. Second, the high-speed motion of an explosion requires diagnostics that capture as much information as possible as quickly as possible. This, in combination with the generally intolerable expense of many repetitions of an explosive test makes reliable instantaneous measurement capabilities vital. Finally, the size and shape of these fragments is of interest but highly unpredictable, motivating the development of diagnostics with the flexibility to accurately measure these characteristics for a variety of fragments in a single explosion.

The motion of explosively generated fragments has been examined for nearly a century using pressure and acceleration measurements and by examining the post explosion locations of fragments to determine general information about the velocities and directions of these fragments [1–3]. Not only is the resolution and accuracy of these methods limited, but these methods are also time consuming and expensive due to extensive experimental requirements. One of the most popular methods for large scale explosives testing is arena testing. In execution of this technique, an explosive is surrounded by large screens of corrugated cardboard with aluminum electrodes on each side allowing measurement of impact velocity on each screen. The fragments are then embedded in bundles of Celotex (a type of insulation) several feet thick which are placed behind each piece of cardboard. The fragments must then be manually recovered, measured, and correlated with the entry holes [4,5]. Obviously, this is an expensive and labor-intensive process.

Recent technological advances have allowed the development and application of various optical diagnostics for explosion analysis. Today, advanced techniques allow the non-invasive measurements of 3D particle fields, which have shown successful measurement of 3D features of explosions but also brought to light measurement limitations. Scanning techniques using high speed cameras to image a volumetric region can provide a 3D representation, but are limited by the non-instantaneous time of image capture [6]. The use of tomography has been shown to provide valuable 3D information and is a well-developed technique due to extensive use in a variety of applications, however, the requirement of multiple cameras to capture volumetric information results in a complicated experimental setup that creates a roadblock in applications with limited optical access. Tomography is also limited to a narrow volume depth relative to the field of view [7,8]. Holography provides a simplification in the use of only a single camera, but still requires carefully aligned coherent illumination and the measurable volume size is limited by the lens size. This illumination allows the interference pattern-based post processing, but also introduces a limitation in applications in which density gradients create unwanted interference patterns, such as shock waves on high velocity fragments [9–12].

In this dissertation, the application of an emerging technology, the plenoptic camera, to the measurement of 3D particle and fragment fields is investigated and algorithms that utilize the computational refocusing and perspective shift capabilities of plenoptic imaging are developed. Plenoptic imaging is an attractive diagnostic tool due to experimental configuration benefits that can reduce the previously identified limitations, such as the requirement of only a single camera and the flexibility allowed by the use of various illumination sources. However, as it is a developing technique, its limitations are largely uncharacterized and there are still significant areas of unexplored algorithm development to make full use of the available information in the raw data for the specific application of particle measurements.

In previous related work, the plenoptic camera has been used to measure 3D particle positions from a series of computationally refocused images used as a volumetric representation of the scene in different experimental applications. These experiments and analysis confirmed the viability of making quantitative depth measurements from computationally refocused plenoptic images and highlighted new challenges in development of the diagnostic [13], which have motivated avenues of algorithm development and uncertainty characterization that will be investigated in this dissertation.

This dissertation is motivated by three general limitations of that previous work. First, errors resulting from lens distortion necessitate the development and implementation of a volumetric calibration to achieve quantitative measurements. Second, the creation of a series of refocused images with the required density and subsequent measurement of particles from this volumetric representation is an exceedingly computationally expensive process. This motivates the use of the perspective shift capability of the plenoptic camera because the arrangement of the raw plenoptic data into this format requires orders of magnitude less computational expense. It is also hypothesized that the metrics used to determine particle location from perspective views will allow identification at more extreme depths than those measured from refocused images. Third, because plenoptic imaging remains a developing technology it is necessary to characterize the measurement uncertainty achievable and how it is affected by physical limitations of the system as well as by algorithmic limitations of each processing method. This uncertainty characterization can then be used to guide determinations not only of the applicability of plenoptic imaging to a given experimental condition as compared to other techniques, but also to make determinations about the method with which the raw plenoptic data should be processed. Specific research objectives of this dissertation are as follows:

- Optimized use of the available raw plenoptic data available to allow maximum precision and accuracy of particle measurements
- Development of a volumetric calibration scheme and integration of the calibration procedure into the data processing stream
- Algorithmic exploration and development of 3D particle location using refocusing and perspective shifting towards improved measurements, reduced computational expense, and increased flexibility of identifiable particle characteristics
- Determination of the uncertainty characteristics of plenoptic imaging for the measurement of particles and fragments with varied size and shape

- Assessment of the applicability of plenoptic imaging to the measurement of explosively generated fragments and similar experimental configurations

The strategy used to achieve these research objectives is shown in the flow chart in Figure 1. This process begins with the development of a polynomial based volumetric calibration method. Then algorithms are developed using the refocusing and perspective shift capabilities of plenoptic imaging. Due to the straightforward nature of creating a volumetric representation from a series of refocused images, the depth from focus method is implemented first chronologically. An uncertainty characterization of the measurements resulting from each method is conducted and the results are compared. Refinements and further analysis are made based on these results and the contributions of various error sources to the particle measurements is assessed. Finally, particle measurements in experimental applications are conducted. The remainder of this chapter serves as an overview of this dissertation.

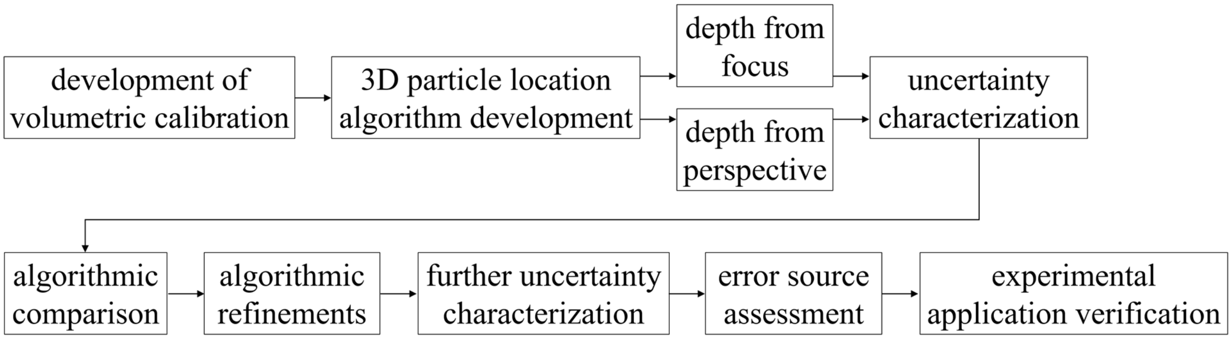

Figure 1. Flow chart outlining the research strategy implemented in this work.

Chapter II provides background information and a literature review of the previous research and topics relevant to this work. The development of light field imaging and specifically plenoptic cameras is discussed including historical and current applications of these technologies. An explanation of the reconstruction methods used to decode raw plenoptic image data is provided as a foundation for the algorithm development in later chapters. An overview of particle tracking as it relates to determination of particle location is included, a review of efforts in explosion analysis is given, and finally relevant motivating experimental efforts for this work are summarized.

Chapter III discusses three methods of the volumetric calibration for a plenoptic camera. The development and mechanics of each method is explained. The success of each method is examined experimentally, and they are compared by metrics of accuracy, computational efficiency, and logistical requirements and feasibility. Direct Light Field Calibration is deemed most appropriate method given the requirements of this work and is applied in a demonstration of a spherical calibration here as well providing an example of the use of this type of calibration in a varied application space.

Chapter IV presents a method for determination of particle location using refocused plenoptic images. A description of the algorithmic development and implementation is provided. This method is examined using a well-controlled experimental system from which experimental uncertainty is characterized. The resulting uncertainty is also examined in reference to theoretical limitations and expected trends. Finally, limitations of this method are presented.

Chapter V presents a method for determination of particle location using perspective shifted plenoptic images. A detailed description of the algorithmic development is provided, and the computational requirements of the method are presented.

Chapter VI examines similar well controlled experiments to those in Chapter IV using the perspective shift method and provides measurement uncertainty characterization of this method and compares it to the refocusing based results. Additional experimental configurations are also examined to expand the particle type parameters based on the motivating applications and examine the in-plane size uncertainty of the perspective shift method.

Chapter VII considers the expected propagation of error through the measurement system and deconstructs possible error inducing mechanisms. Several sources of error are examined, and synthetic and experimental calibration coefficients and images are considered to qualitatively and quantitatively assess the effects of each.

Chapter VIII examines the application of the perspective shift algorithm to two experiments. First, the secondary droplet field created by the impact of a drop of water on a thin film of water is measured and compared to measurements of the same experimental data set made using refocused images. Second, the fragment field created by a lab-scale detonator is examined providing qualitative verification of the application of these measurements to explosion analysis.

Chapter IX summarizes the conclusions and contributions of this work and provides suggestions of avenues for future work based on these findings.

II. Background

The algorithms and uncertainty characterizations developed in this work are focused on application of a plenoptic camera, an implementation of light field imaging, to a variety of experimental configurations for the measurement of 3D particle and fragment positions. This chapter explains the basics of the plenoptic imaging implemented in this work, provides an overview of the development of light field imaging, and surveys the development and current state of the art in other related research areas relevant to this dissertation.

A. Light field imaging and the plenoptic camera

A plenoptic camera is created from a standard scientific camera that is modified by a microlens array placed between the main lens and the image sensor. These microlenses redirect the incoming light rays to different image sensor locations according to the angle of propagation of the light, thereby encoding the 3D volumetric information of the imaged scene onto a 2D image sensor.

Figure 2 provides a schematic depiction of the basic components and arrangement of a plenoptic camera [14]. The gray region indicates the path of the cone of light rays emanating from an example point in object space. This light is focused through the main lens aperture, redirected by the microlens array, and finally incident on the image sensor. The overarching goal of the current work is consideration of the various methods of decoding this 2D image and determination of the information pertinent to measurement of 3D particle locations within an experimental scene to develop algorithms to execute those measurements.

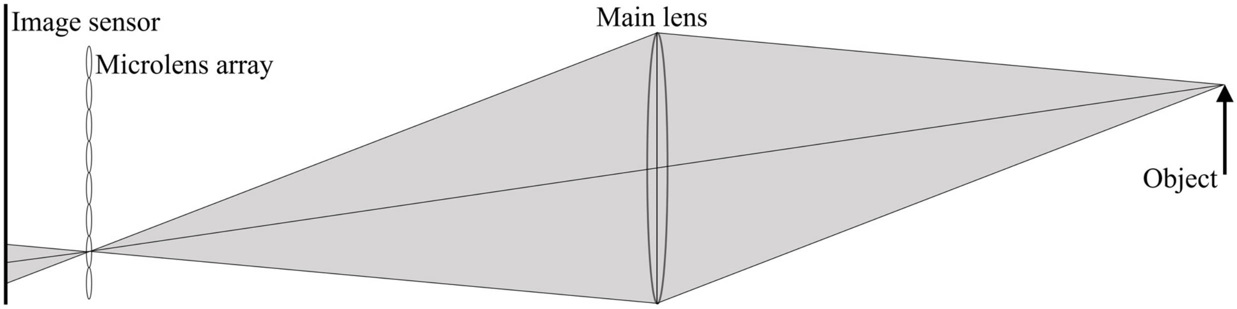

Figure 2. Schematic depiction the general plenoptic camera configuration, adapted from Ng et al. [14].

i. Historical development

Plenoptic imaging is an implementation of light field imaging, a field that originated conceptually as early as 1908 [15] but was not experimentally examined until the more recent development of high resolution digital image sensors in the early 1990's. Adelson and Bergen [16] formally defined the plenoptic function as a representation of the light at every angle, (θ,ϕ), at every wavelength, λ, at every time, t, at every point in space within some region of consideration, (x,y,z) as,

$$P = P\left(\theta,\phi,\lambda,t,x,y,z\right). \tag{1}$$

They consider this 7D function an idealized concept, not a physically measurable quantity [16]. A year later, Adelson and Wang created what they termed a plenoptic camera, a device intended to measure a subset of the plenoptic function limited by the viewpoints within the physical lens aperture, the wavelengths measured by the image sensor, and the time of image capture. This was the first practical implementation of a plenoptic camera and was assembled using a relay lens configuration [17]. This was followed by a handheld portable version of the plenoptic camera developed by Ng et al. in 2005 that removed the relay lens [14]. These works provided the springboard for the rapid development of plenoptic imaging in recent years in a variety of fields.

Critical to these developments was simplification of the plenoptic function by assumptions relevant to practical application of image capture. The first assumption was that an image is captured at a single instant; therefore, time is considered constant. Second, changes in wavelength are not considered by the image sensors used; therefore, wavelength is considered constant. These two assumptions reduce the function to 5D. The function is further reduced to 4D in free space as radiance is constant along a straight line; therefore, one of the spatial coordinates is constant. This finally results in a light field defined by two angular and two spatial dimensions [17]. For simplicity of sampling and computational efficiency, this light field is often described using a two plane parameterization where the position of a light ray is fully defined by the coordinates of its intersection on two parallel planes. In practice, these two planes are the aperture plane and the microlens plane, as is shown schematically in Figure 3 [18].

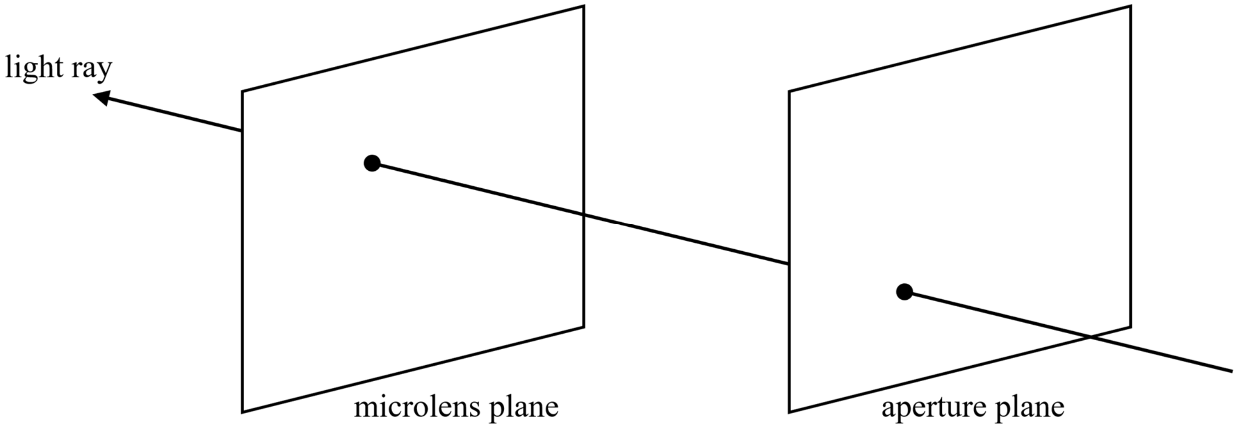

Figure 3. Schematic depiction of the two plane parametrization, adapted from Levoy and Hanrahan [18].

ii. Implementations and applications

Much of the early development in light field imaging remained within the computational photography and computer vision community and development in this area of plenoptic imaging remains a robust research area today with wide ranging applications. In particular, light field imaging has been used for image based modeling to allow creation of photorealistic computer graphics towards a goal of fast visualization of 3D scenes [19,20]. Plenoptic imaging has also been exploited for depth estimation of objects and features in a scene. The interpretation of 2D images as part of the 4D plenoptic function in this case allows the creation of views from arbitrary camera positions [18,21]. The camera configurations in these applications range from large camera arrays to gantry mounted moving cameras to single camera lens array systems [22].

Additionally, light field imaging and plenoptic cameras have been widely applied as a scientific measurement tool. Combining plenoptic imaging with existing optical diagnostics has allowed for extension of these measurements to 3D while maintaining experimental flexibility and simplicity often lost in other 3D techniques. In particular, various studies have examined application of plenoptic imaging to particle measurements using particle image velocimetry (PIV) and particle tracking velocimetry (PTV) for many applications at a wide range of scales [23–28]. Extensive work has been done in the development of these techniques including reconstruction of a 3D volume of a gaussian vortex ring from simulated plenoptic data using the multiplicative algebraic reconstruction technique computed tomography algorithm by Fahringer et al. [23]. Skupsch and Brücker developed a method using multiple plane illumination to implement PIV with a processing method based on synthetic aperture PIV which allowed quasi-simultaneous velocity measurements at multiple depth planes with high spatial resolution [28]. Bajpayee and Techet extended light field imaging to 3D PTV and showed improved accuracy and computational efficiency as compared to PTV implementations based on synthetic experimental benchmarking [29]. Light field imaging has been integrated into a microscopic PIV system by Truscott et al. and was shown to accurately measure in-plane velocities in a 3D volume [26].

Numerous recent studies have worked to apply plenoptic imaging to particle based measurements, a few are listed here. Ostmann et al. used a plenoptic camera for PTV to determine 3D particle trajectories in a swirling flow in an experimental configuration with limited optical access [27]. Chen et al. applied volumetric pulsed laser illumination in combination with a plenoptic camera to visualize the liquid fuel spray development in a spark-ignition direct-injection engine [30]. Chen and Sick later applied plenoptic imaging for 3D3C PTV measurement of air flow in an engine steady-state flow bench [25]. Johnson et al. obtained volumetric velocity measurements in the wake of a hemispherical roughness element using a plenoptic camera. This study identified various 3D flow phenomena indicating the ability of the plenoptic camera to resolve particle motion in the out of plane direction [24].

Others have applied plenoptic imaging to measurements of scalar fields. Nien et al. developed a method for the measurement of translucent objects using a plenoptic camera and a model based reconstruction method [31]. Klemkowsky et al. demonstrated qualitative observation of the depth dependent density gradients present in flames and in a heated jet by applying background oriented schlieren with a plenoptic camera [32]. Danehy et al. used three bandpass filters placed in front of a plenoptic camera to obtain separate 2D images on a single image sensor which were processed to determine 2D temperature distributions of various known calibration heat sources [33].

The plenoptic cameras used throughout the current work were constructed by the Advanced Flow Diagnostics Laboratory (AFDL) at Auburn University using an Imperx Bobcat B6620 29MP, which has a CoaXPress KAI-29050 CCD image sensor (6600 × 4400 pixels, 5.5 µm pixel pitch) and is modified by the addition of a microlens array with 471 × 362 hexagonally arranged microlenses positioned approximately 308 µm (the microlens focal length) from the image sensor using a custom adjustable mount as shown in Figure 4 (left). The pitch of the individual microlenses is 77 µm. After plenoptic processing, the resolution of the output images is approximately 900 × 600 pixels. This change in resolution is a result of the resampling of the raw image data from the hexagonal microlens arrangement to a rectangular arrangement, allowing for creation of a standard rectangular image and is not intended as a super resolution technique and does not increase the actual data resolution. A photo of the plenoptic camera is shown in Figure 4 (right) with a coin indicating scale and demonstrating the compact size of the camera.

Figure 4. Photo of the microlens array in the custom mount designed by the AFDL (left) and photo of the plenoptic camera constructed by the AFDL equipped with a 60 mm Tamron main lens (right).

B. Plenoptic data structure and reconstruction methods

Volumetric information can be extracted from a raw plenoptic image in two distinct formats in post processing, computational refocusing, which changes the apparent focal plane of the image and perspective shifting, which changes the apparent angle from which the scene is viewed. Before examining the creation of these volumetric representations, the data structure of a raw plenoptic image is examined here, displayed schematically in Figure 5, using the conventional two plane parameterization [18]. The images in the top row show a raw plenoptic image of the explosively generated fragment field from an RP-80 detonator. This is followed by inset images that show the individual sub aperture images, or the view of the main lens aperture from each individual microlens. A two plane parameterization is used to fully define the position of the light rays in 3D space. The spatial position of the incoming light rays is described by location on the microlens plane, defined in (s,t) coordinates. The angular position of the incoming light rays is described by location on the main lens aperture plane, defined in (*u*,*v*) coordinates [18]. These coordinate systems are depicted in the first and second inset images and identified by red and blue in the schematic, respectively. In the current work, the computation of refocused and perspective shifted images is executed using functionalities of the Light Field Imaging Toolkit (LFIT), a collection of open source MATLAB functions for plenoptic processing developed by the AFDL [34].

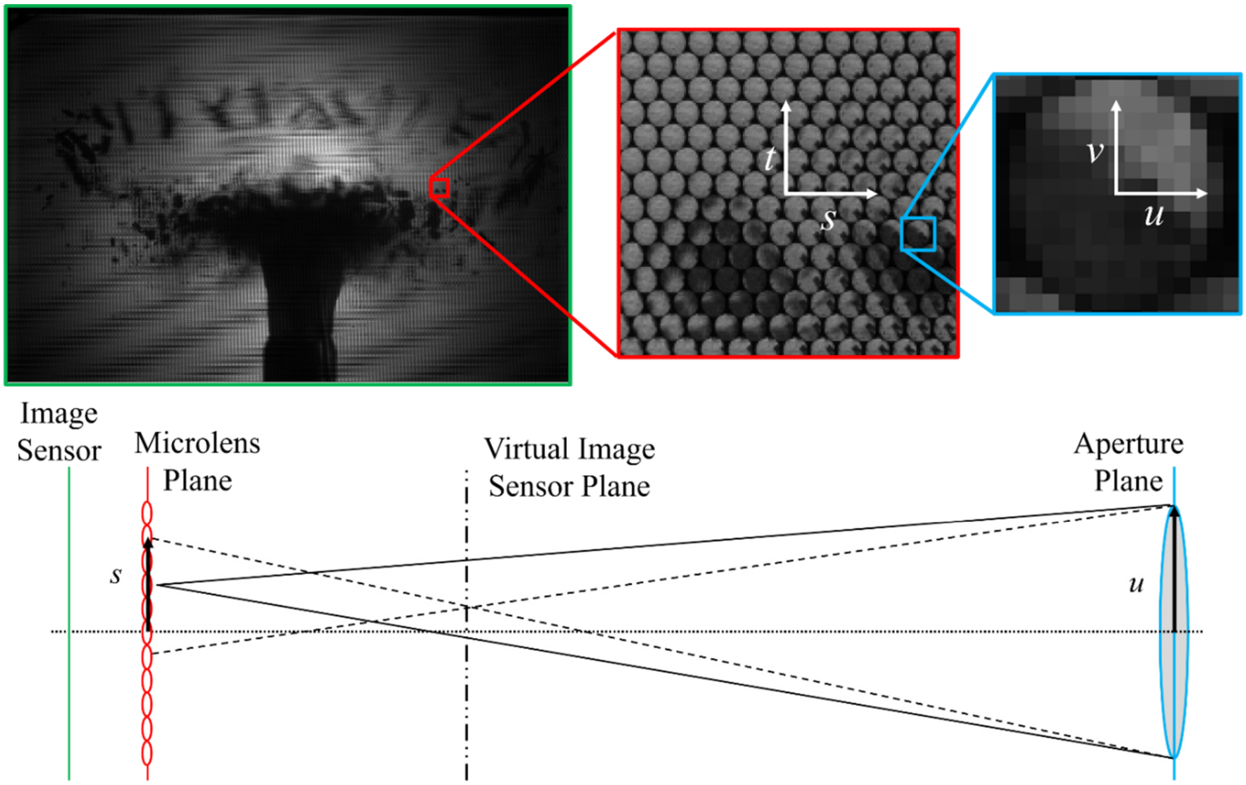

Figure 5. Raw plenoptic image and insets depicting the microlens array (top), schematic of light field data structure (bottom).

The microlens and aperture planes define the 4D light field, *L*(*u*,*v*,*s*,*t*), which defines the amount of light travelling in all directions through all points in space. Decoding these sub aperture images to create synthetic images is based on the relationship between the light field and the synthetic light field *L'*. In the implementation discussed here, *L'* is defined by the location of the light ray on the aperture plane and the virtual image sensor plane, defined by (*s'*,*t'*) coordinates. *L* and *L'* are related by,

$$L'(u,v,s',t') = L\left(u,v,u+\frac{s'-u}{\alpha},v+\frac{t'-v}{\alpha}\right), \tag{2}$$

where α is a parameter relating the location of the virtual image sensor plane relative to the aperture plane as compared to the location of the microlens plane relative to the aperture plane, as defined by Ng et al. [14].

i. *Computational refocusing*

Computational refocusing is achieved by executing a shifted integration of the image pixel intensities over the entirety of the sub aperture images as shown in the example in Figure 6 where the raw image from Figure 5 was refocused to two different depths. The creation of a refocused image is defined by Ng et al. [14] as,

$$E(s',t') = \iint L\left(u,v,u+\frac{s'-u}{\alpha},v+\frac{t'-v}{\alpha}\right)A(u,v)\,du\,dv\,, \tag{3}$$

where $A(u,v)$ is the aperture location and $E(s',t')$ is the resulting refocused image.

This process is depicted schematically in Figure 7. Light rays emanating from an object located at the nominal focal plane are depicted in blue; these rays propagate through the aperture plane and are focused onto a single point on the microlens array. These rays are then incident on the image sensor pixels behind the corresponding microlens, thus, integrating over the pixels behind each microlens produces an image focused at the nominal focal plane. In contrast, light rays emanating from an object located at a refocused plane, shown in orange, are focused at the virtual image sensor plane. These rays are then incident on multiple microlens and multiple sub aperture images, therefore, executing a shifted version of the integration over the pixels behind each microlens produces an image computationally refocused to the plane of interest.

Refocusing provides a straightforward volumetric representation of a scene. Particle location can be determined from a series of refocused images, termed a focal stack, using metrics of edge sharpness and intensity. A significant drawback of this method of particle location is in the large computational requirement of the integration to create a single refocused image and the large number of refocused depths required to make a sufficiently dense depth sampling. Additionally, determination of independent depths of objects that overlap in the in-plane dimensions can be difficult without the use of advanced image segmentation schemes which are outside the scope of the current work.

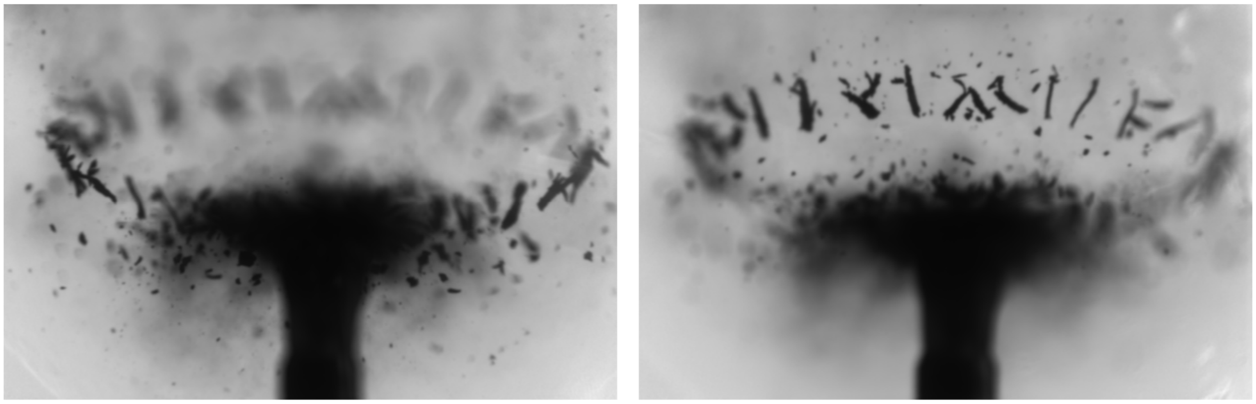

Figure 6. Refocused images with focus computationally shifted to the foreground (left) and background (right).

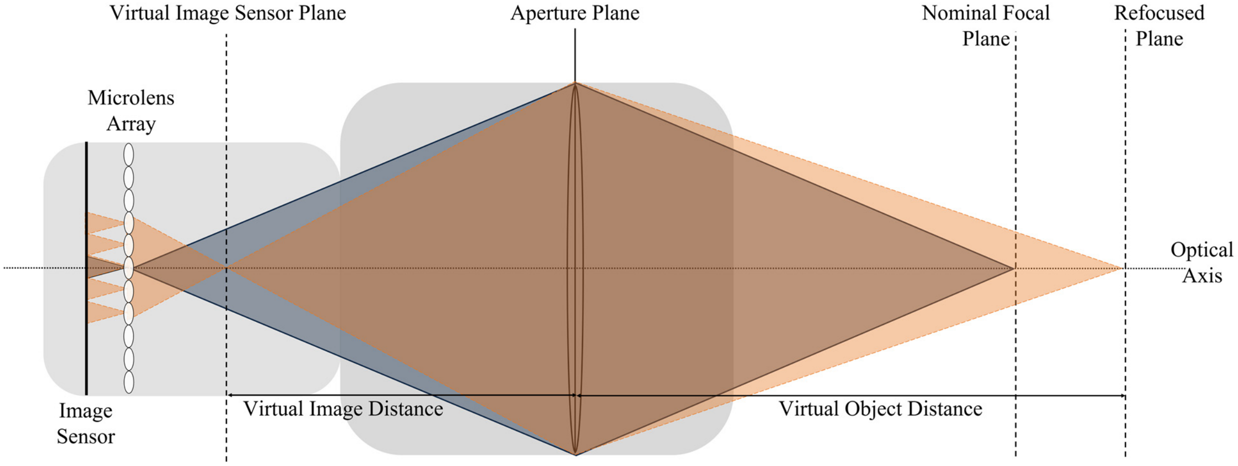

Figure 7. Schematic depiction of computational refocusing.

ii. Perspective shift

Shifting the perspective from which the imaged scene is viewed is achieved by combining the pixel from the same main lens aperture location within each sub aperture image. The resulting image can be compared to the image that would have been captured using a pinhole aperture at the selected main lens aperture location, resulting in an image with a large apparent depth of field. Figure 8 gives an example of perspective shifted images where the viewing angle has been shifted in the vertical direction, again from the raw image in Figure 5. The creation of a perspective shifted image at a selected aperture location, (u_0,v_0), is defined by Ng et al. [14] as,

$$E(s',t') = L\left(u_0, v_0, s', t'\right). \tag{4}$$

This process can be conceptually described as simply selecting the corresponding pixel from behind each microlens, or from each sub-aperture image, and arranging these pixels based on the position of the microlenses. The creation of these perspective shifted images is significantly less computationally expensive than refocusing. Object depth can then be determined by creating a variety of perspective views from different aperture locations and comparing the position in which an object appears in each view. This requires a robust method of identifying the corresponding object in each view, a non-trivial task that will be discussed in detail in Chapter V.

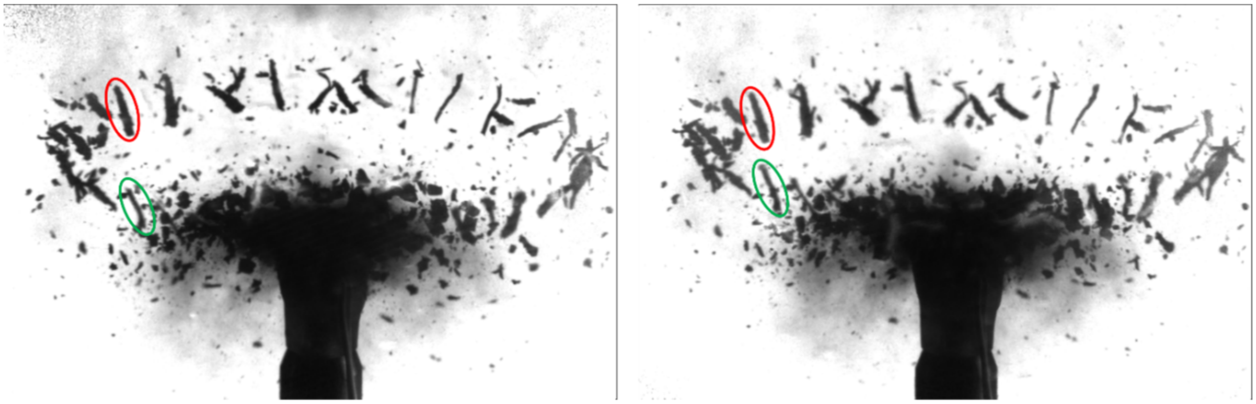

Figure 8. Perspective shifted images with the viewing angle shifted up (left) and down (right).

iii. Combination of cues

Though refocused and perspective shifted images produce two distinct representations of a 3D scene, cues from both methods can be combined in determination of object location to allow optimized use of the available information and avoid limitations of each reconstruction method. For a detailed compilation of the strengths and weaknesses of measurements from refocusing and perspective shifting, see Tao et al. [35]. Two of these differences are of particular relevance to the particle and fragment measurements in the current work. First is the performance of each in cases of occlusions. Refocusing is more easily affected by occlusions but also more stable to occlusions than perspective shifting. Wang et al. examined the identification of occluded regions in detail and used perspective and refocusing information to correctly identify depth in these regions [36]. Second is the elevated noise level in perspective shifted images as a result of the small effective aperture. The algorithm development in this dissertation considers these and other characteristics of each method and uses aspects of both in the final 3D particle location implementation.

C. Particle tracking

The goal of this work is the measurement and improvement of 3D particle location; however, an understanding of the relevant particle tracking methods, algorithms, and limitations remains critical to allow appropriate particle location results which can be used in later particle tracking. The development of PTV began in the mid 20th century and has continued alongside PIV with interest rapidly increasing beginning in the 1990's as a result of the availability of advanced imaging technology.

i. PTV vs. PIV

PTV is often described as low-density PIV, however, this can be a misleading comparison as there is also a fundamental difference in how measurements are made with each processing method. In PIV, particles are measured in groups by cross correlation, requiring a sufficiently large number of particles in each group or region. In PTV, individual particles are matched between frames, a process that becomes increasingly complex as particle density increases [37,38]. This differentiation is shown schematically in Figure 9 where, on the left, examples of two particle image frames are shown. The results of each technique are then shown on the right; in the PTV example a vector is determined for each particle matched between the two frames and in the PIV example a single vector is representative of the motion in region. It should be noted that these schematics are not necessarily representative of a difference in the achievable velocity resolution between the two methods. In practice, when the particle density is high enough to allow successful cross correlation in PIV, the particles are generally too closely spaced to allow successful matching of a substantial percentage of the individual particles in PTV.

Despite these basic differences PTV and PIV are not incompatible, and the most appropriate technique is highly dependent on experimental parameters. Kim et al. compared tomographic PIV and 3D PTV for a microfluidic flow of a confined shear driven liquid droplet over a moving surface and determined that tomographic PIV provided more reliable results [39]. Pereira et al. determined that in some cases PTV can provide a benefit over PIV in 3D applications due to increased spatial resolution. Additionally, in the case of a neural network based PTV scheme the use of a mean flow estimate from PIV can improve results [40]. Cowen and Monismith used a combination of PIV and PTV techniques by using the results of a large window PIV pass as inputs, i.e. displacement guesses, for a PTV algorithm, thus limiting the possible matches between images [41]. Truscott et al. have also suggested that PIV and PTV techniques could be combined to improve results in light field μPIV [26]. Weineke has developed an iterative particle reconstruction method that reconstructs 3D particle locations similarly to MART but represents particles as 3D positions rather than blobs, combining aspects of both PIV and PTV [42].

Other works have used PIV and PTV simultaneously but independently to measure multiphase flows. Bröder and Sommerfeld measured the velocities in a bubble column using PIV to measure the liquid phase and PIV followed by a PTV pass to measure the gas phase. The use of fluorescing tracer particles in the liquid phase and optical interference filters with band widths corresponding to the emitting wavelength of the particles and of the applied Nd-YAG laser allowed separation of the signal from the two phases [43]. Zhang et al. measured wind-blown sand by using PIV to measure the gas phase, seeded with oil, and PTV to measure the sand particles; the phases were separated using a digital phase mask technique [44].

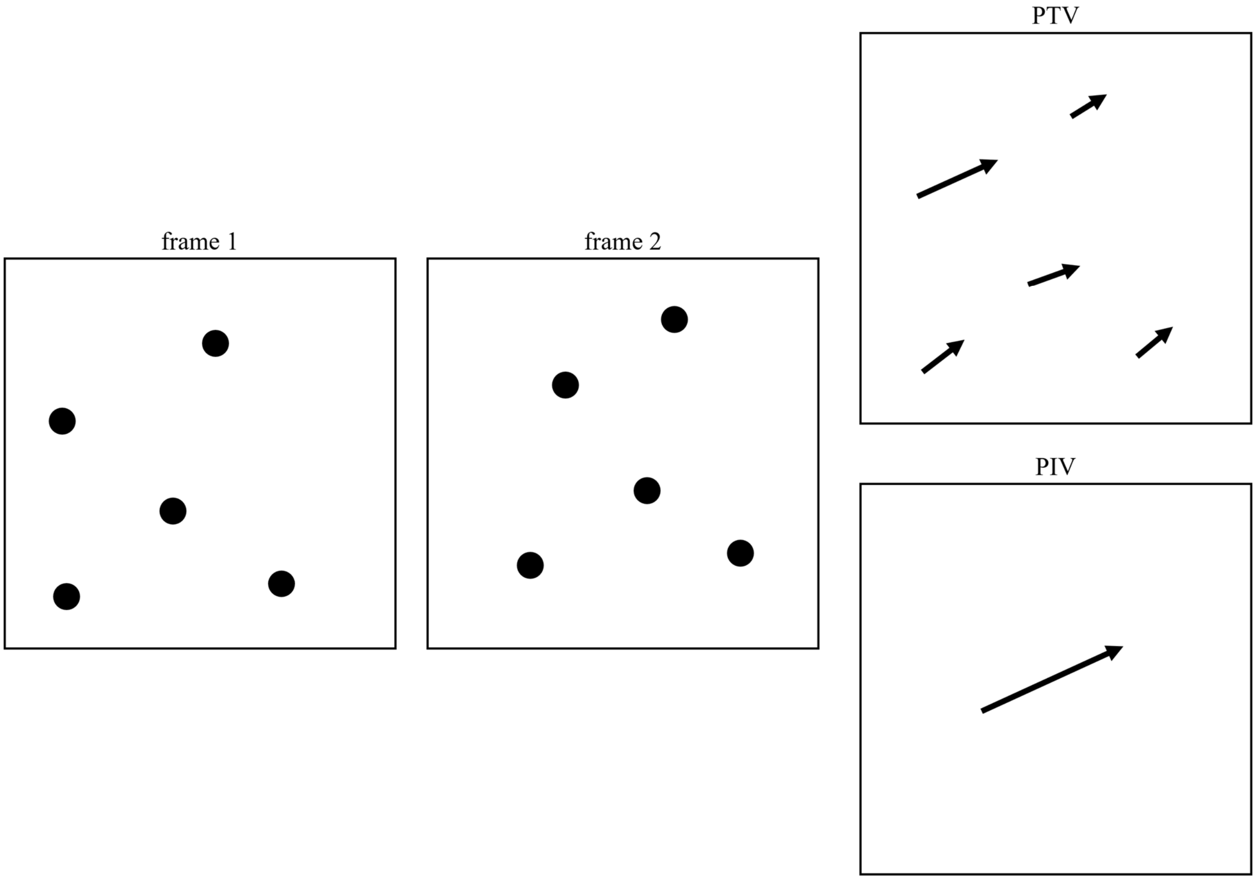

Figure 9. Schematic example of the difference in PTV and PIV, adapted from Stitou and Riethmuller [45].

ii. Correspondence problem

Generally, the focus of PTV algorithm development is on what is termed the correspondence problem, or the matching of particles between frames. In the current work, techniques developed for matching particle images in image frames separated in time are adapted to the problem of matching particle images in varied perspective views. Specifically, the use of qualified search criteria is explored. Traditional PTV methods use known flow field information to limit search areas, for instance a widely cited method of particle tracking developed by Hassan and Canaan relies on the, generally valid, assumption that given the small time step between images in a sequence, the acceleration and change in angle of travel of a particle is small. Given this, a set of possible tracks is considered and the one with the smallest variance in these parameters is selected [46]. In the current work, the known relationships between view locations is examined as a limiting factor.

Additionally, clustering methods are considered to allow matching of particle images in all views simultaneously. Ohmi and Li use a form of clustering in their relaxation method which considers the motion of neighboring particles in determination of the validity of a particle match [47]. In the current work a clustering method is selected, *k*-means clustering, that minimizes the potential function, or the average squared distance between points in a cluster. This method has been widely used since it was introduced by Lloyd in 1982 as a general method for quantizing a real random variable [48].

The general *k*-means algorithm is as follows:

1. A set of *k* initial cluster centers, *c*, is selected from the pool of all points, *X*. The *k*-means variation used here also strategically selects these initial centers to improve performance.

2. Each of the remaining points *X* is assigned to the closest center *c*.

3. The center of mass of each of these clusters is calculated and defined as the new center of the cluster.

4. Steps 2 & 3 are repeated until the centers no longer change [49].

A simple example of the *k*-means algorithm is given in Figure 10 where points are divided in to three clusters. The square on the left shows an initial configuration where crosses mark the three points selected as initial cluster centers. Each remaining point is color coded based on the cluster it is assigned to by on proximity to the nearest center. The square on the right then shows the new centers calculated as the center of each cluster. The points here are then reassigned by proximity to the new centers.

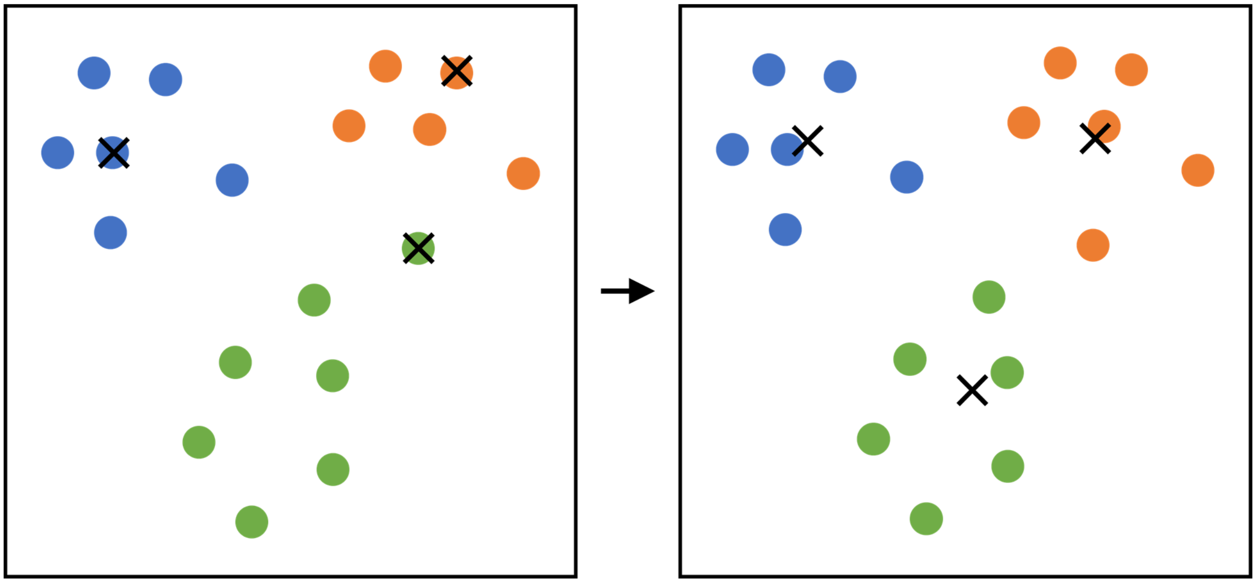

Figure 10. Schematic depiction of *k*-means clustering, adapted from Vattani [50].

The popularity of *k*-means is a result of the guaranteed termination of the method as well as its simplicity and speed, however, there is no inherent guarantee of accuracy. Since its introduction *k*-means has been applied in a variety of fields and many researchers have created modified versions of the original implementation. One such example comes from Arthur and

Vassilvitskii, who developed the *k*++ means algorithm which strategically selects the initial seed points such that each selected center is most likely to be far away from any existing centers. This improves both algorithmic speed and resulting cluster accuracy [49].

The *k*-means++ selection of initial seed points is as follows:

1. One center, c_1 is chosen uniformly at random from X.
2. A new center c_i is chosen such that $x \in X$ with probability $D(x)^2 / \sum_{x \in X} D(x)^2$, where $D(x)$ is the shortest distance from a data point to the closest center already chosen.
3. Step 2 is repeated until k centers have been selected [49].

iii. Implementations and applications

In addition to those works discussed in the previous subsections, PTV has been implemented in many other configurations for a wide ranging application space and with a variety of processing algorithms. A few of these are listed here. The early development of 3D PTV began in 1993 when Maas et al. developed a method for photogrammetric determination of particle coordinates in 3D using a multi camera system [51]. This work was followed by the development of a fully automated tracking scheme by Malik et al. that used these coordinates to determine velocity vectors in a 3D volume. The algorithm was validated in both turbulent and non-turbulent experimental flows [52]. Labonté applied a neural network to PTV in an effort to solve the correspondence problem efficiently. That work showed that neural networks can outperform the nearest neighbor algorithm with the added benefit of parallelizability. In addition, the data sets used in this work were made publicly available to allow valid comparisons with future methods [53]. Kim and Lee used a micro digital holographic PTV system to measure a laminar water flow inside a micro tube with a diameter of 100 µm. The velocity profiles measured in this study showed good agreement with theoretical profiles and showed improvement over previous studies as a result of adaptations in the experimental configuration [54].

D. Explosion analysis

The motivating application of this dissertation is the measurement of explosive fragments in 3D, however the development of techniques towards these measurements has been of interest for over a century. The scope of data that could be obtained from these studies has, of course, changed dramatically over that time. In 1913, Hopkinson developed a method for the measurement of the duration and pressure of the impact of a bullet by measuring the motion of a suspended rod impacted by the bullet. The experiments conducted in that study were used to confirm theoretical predictions of the pressure produced by the impact of several different configurations of lead bullets [1]. This early work examining a single ballistic object is obviously a substantially different application from, and in many ways a simplification of, the highly 3D, multiple-fragment explosions of interest in this work, but clearly highlights the difficulty of the measurement.

An example of a diagnostic system more closely related to the current work is the Vulnerability and Lethality Testing System (VALTS), which was used at Eglin Air Force Base, Florida, beginning in 1971 for large scale arena testing of the effectiveness of explosive munitions. This facility allowed the measurement of average fragment velocities, fragment dispersion, pressure front velocities, and pressure profile velocities from data collected by large screens placed around the munition. The specific composition of these screens varied, but in general two conducting surfaces separated by an insulator allowed an impacting fragment to complete an electric circuit. The time that circuit was completed was recorded to allow determination of fragment velocity [4]. Later, the Fragment Field Analysis Testing (FRAT) system was developed to address some shortcomings of VALTS. Improvements included the ability to distinguish between repeated contacts of the same fragment and the impact of multiple fragments and the ability to record multiple impacts on the same screen simultaneously [5]. Still, the use of recording screens limits the measurements of fragments to the instant of impact and measurements of fragment characteristics such as shape and size must be obtained by manual collection and cataloging of individual fragments post explosion. Figure 11 shows a photo of the arena setup used in the FRAT system, in this demonstration test an eight screen configuration was used [5].

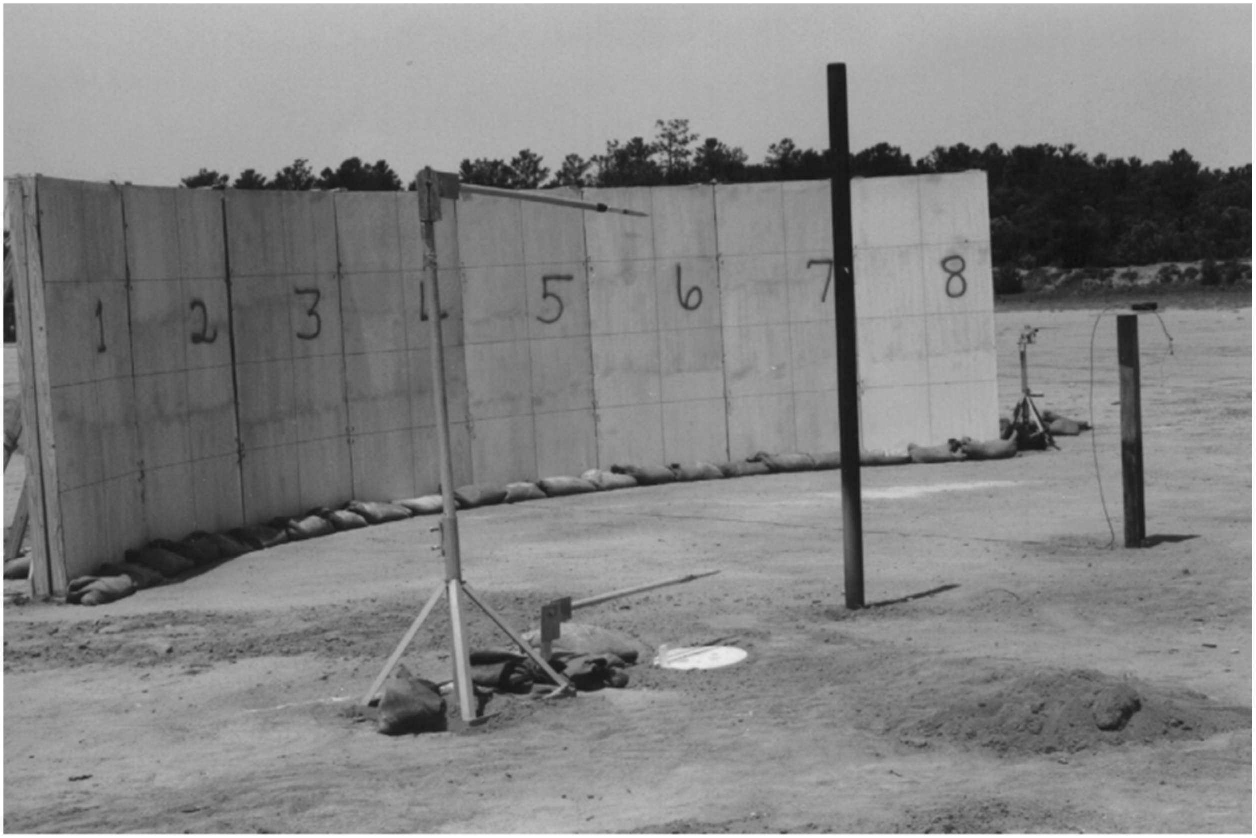

Figure 11. FRAT eight screen configuration demonstration, from Barnard and Nebolsine [5].

Other systems using accelerometers and pressure transducers have been developed for the measurements of small scale explosions. Some studies have been dedicated to the development of instrumentation specifically designed to withstand nearby explosions, such as Yiannakopulous who developed an accelerometer adaptor for this purpose [3]. Brett et al. used these diagnostics to investigate the interaction between submerged surfaces and an underwater explosion. The experimental configuration used in that work is shown in Figure 12 which schematically depicts the floating platform used to mount pressure transducers and accelerometers around the explosive [2].

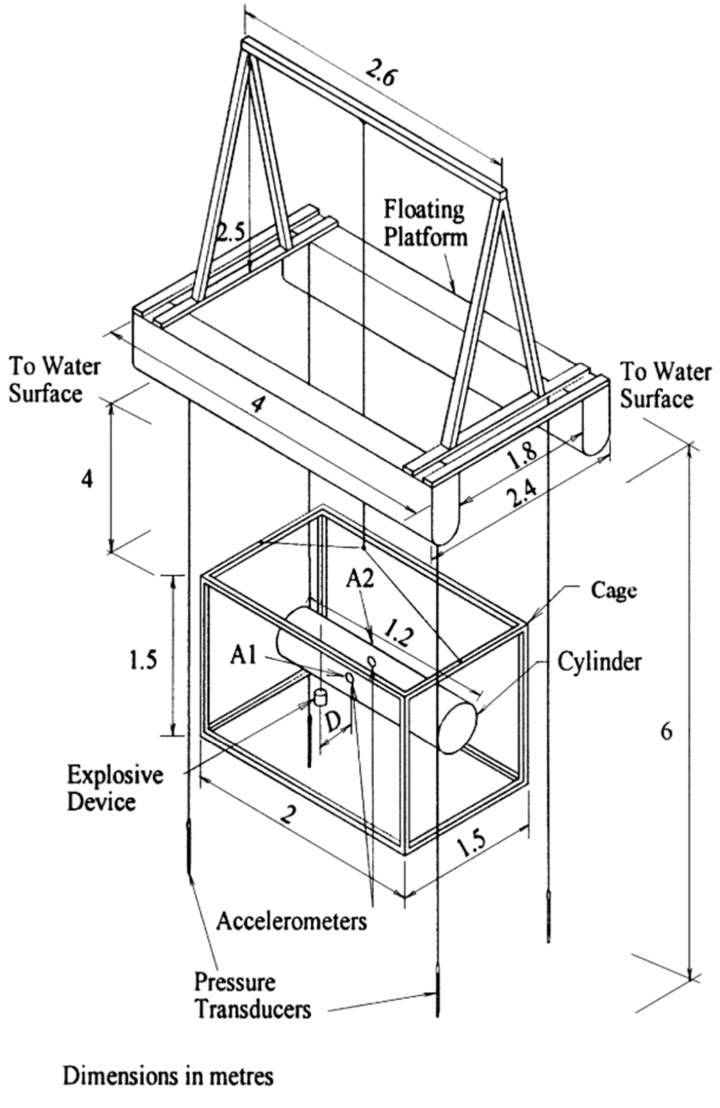

Figure 12. Experimental configuration for submerged explosion testing, from Brett et al. [2].

There are two important takeaways from the experimental configurations shown in Figure 11 and Figure 12 that are of particular interest to the motivation of this dissertation. First, arena testing configurations, like FRAT [5], are large, complex, experimental systems. This means tests are expensive and time consuming, both factors that significantly limit the feasibility of conducting repeated tests. Second, the spatial resolution of measurements in these systems is extremely limited. In the example in Figure 12, only four pressure transducers and two accelerometers are used, therefore, variations in pressure or acceleration in large regions between these sensors could go unmeasured and result in an incomplete picture of the explosive behavior.

These complexities and limitations have motivated the application in recent years of an array of optical diagnostics to explosion analysis. These techniques allow measurements at varied temporal stages throughout the explosions and collection of a large amount of data from a single explosive event with reduced instrumentation. Many of these efforts are focused towards the goal of full field 3D measurements. Bowden et al. studied the initiation of plastic bonded explosives by the impact of hypervelocity metal fragments by using Digital In-line Holography (DIH) to measure fragment size and shape during the explosion. The fragments then impacted polystyrene foam and computed tomography was used to analyze post-test particle distribution [55]. Yeager et al. examined the fragment impact response of plastic bonded explosives using a combination of diagnostics. Witness plates and high-speed video were used to characterize distribution of the particles and DIH was used to measure the size and shape of fragments moving at velocities of between 2.2 and 3.3 km/s. This work provides an example of successful exploitation of optical and physical diagnostic tools to produce an overall measurement with increased fidelity [12]. In a related study Guildenbecher et al. added stereo Digital Image Correlation to make 3D measurements of the initial strain present in a detonator casing [56].

E. Previous relevant experiments

Prior to the current work, a study by the author compared preliminary quantitative measurements made using a plenoptic camera to those made using Digital In-line Holography (DIH) [13]. DIH is a single camera laser-based technique for the 3D measurement of a particle field. In the previous work, two particle tracking experiments with varied parameter spaces were studied, tracking of pellets from a shotgun and tracking of secondary droplets from the impact of a water drop on a thin film of water. This provided preliminary confirmation of the applicability of plenoptic imaging to tracking of large particles and exposed the need for the development of the volumetric calibration and reconstruction algorithms as well as the uncertainty characterization executed in the current work. The previous studies are described briefly here, more detail can be found in [13].

i. Shotgun

Similarly to the DIH configuration in [57], a shotgun (12 gauge, number 9 shot) was placed approximately 15 ft from the field of view of the plenoptic camera, which was equipped with a 105 mm Nikon macrolens. A breakscreen was used to trigger the camera as the shotgun pellets passed through the screen. The pulsed diode and diffuser provided backlight illumination of the pellets, and two images were recorded for each particle field with an interframe time of 5 μs. Figure 13 shows a plenoptic image pair refocused to two different depths. In these images, the pellets propagate from right to left. Figure 14 shows a similar DIH image pair. Visual comparison of these figures provides a qualitative assessment of the two imaging methods.

The vertical bands in the DIH images are a result of shockwaves visible due to the use of collimated laser light for illumination of the measurement volume. This noise source is not observed in the plenoptic results because they were recorded using diffuse light. This noise reduction highlights a significant benefit of plenoptic imaging resulting from flexibility in illumination. Another significant difference that can be seen in these figures, is the variation in the field of view visualized using each method. The field of view used in DIH is limited by the size of the collimation lens, an instrument which is difficult and costly to obtain at diameters greater than approximately 50 mm. In contrast, the field of view of the plenoptic camera can be readily changed by adjusting the focus of the main objective, which in this experiment allowed a larger field of view as indicated by comparison of the scale legend on each figure. This increased field of view of course, also reduces the minimum spatial resolution of the plenoptic system. This is a significant reduction given that a plenoptic camera already trades spatial resolution for angular resolution in the insertion of the microlens array.

In this early attempt at quantitative measurements using refocused plenoptic images, the need for a volumetric calibration was also identified. In the processing of this experimental data, the determination of physical locations of objects was executed by converting from image space to object space using thin lens optics relationships. Though this provides a qualitatively useful depiction of locations, phenomena such as lens distortion present in real lens systems and unavoidable experimental misalignment, created quantitatively significant errors. This motivated the volumetric calibration method development described in Chapter III.

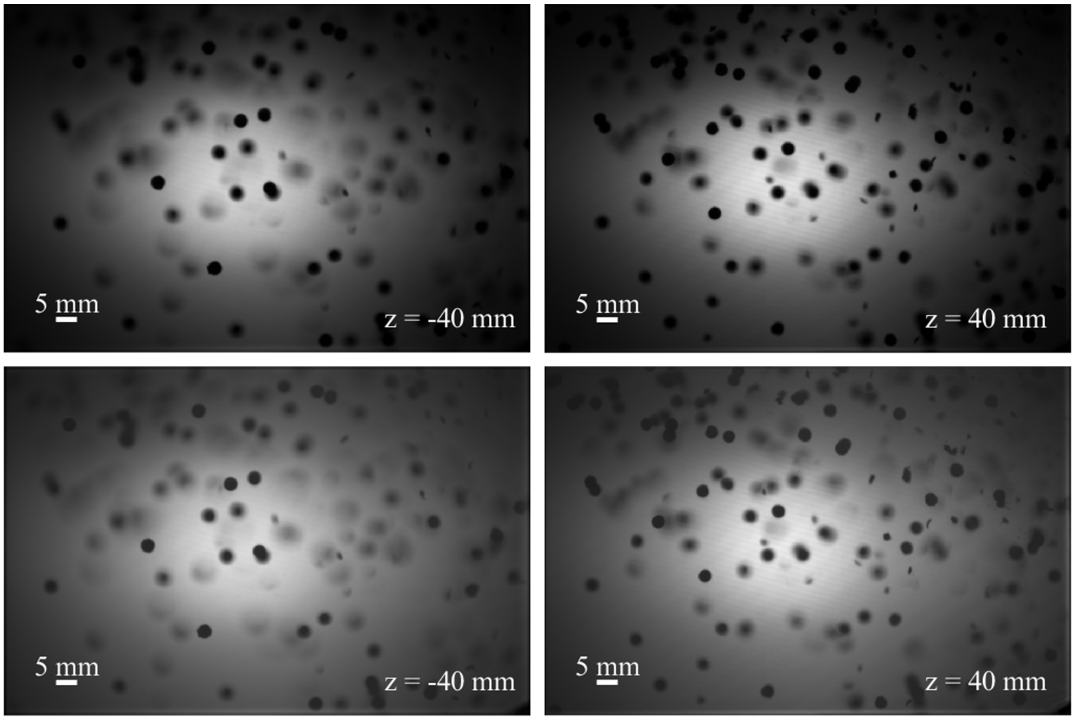

Figure 13. Refocused plenoptic images of pellets from a shotgun, frame 1 refocused near the front of the volume (top left), frame 1 refocused near the back of the volume (top right), frame 2 refocused near the front of the volume (bottom left), frame 2 refocused near the back of the volume (bottom right).

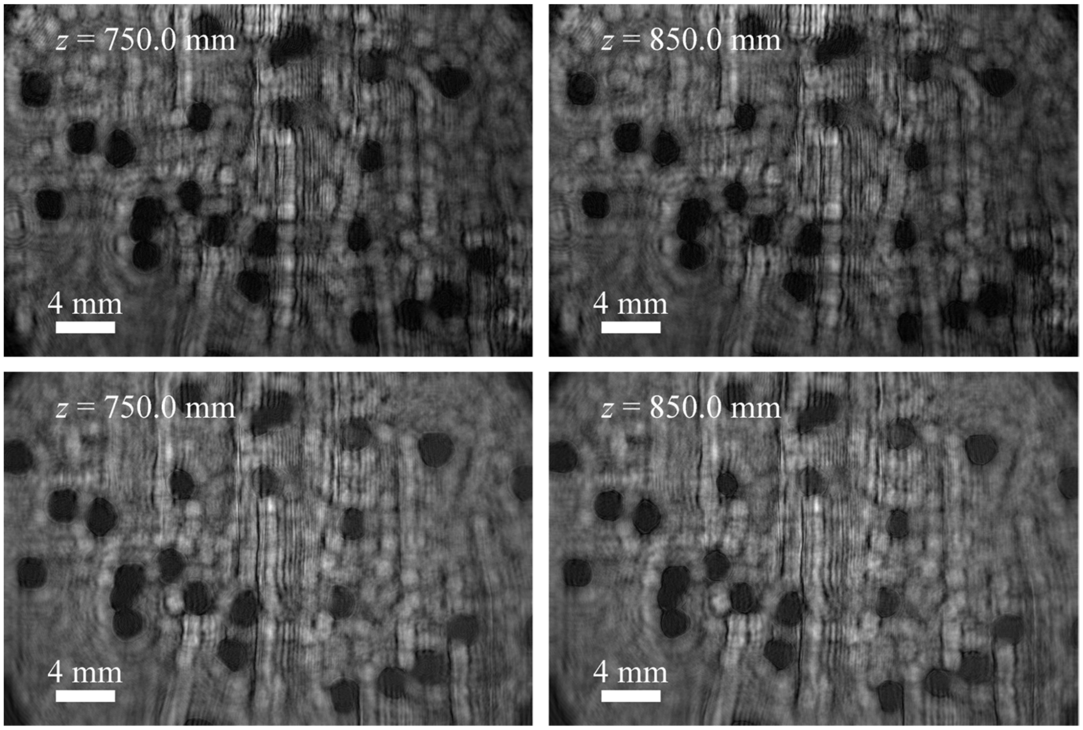

Figure 14. Refocused DIH images of pellets from a shotgun, frame 1 refocused near the front of the volume (top left), frame 1 refocused near the back of the volume (top right), frame 2 refocused near the front of the volume (bottom left), frame 2 refocused near the back of the volume (bottom right).

ii. Drop impact

As was done in Guildenbecher et al. [58], a syringe pump filled with deionized water produced droplets that left a syringe tip at approximately zero velocity and were accelerated by gravity to impact a thin film of deionized water contained in a rubber o-ring affixed to a smooth acrylic surface. The thickness of the film was equal to the height of the o-ring (2.35 mm), and the relatively large diameter of the o-ring (50.8 mm) prevented interaction of the breakup process with the edges. Initial attempts to reconstruct the 3D particle field were complicated by bright spots caused by light refraction through the transparent drops. This was eliminated by coloring the water with black food dye, resulting in nearly opaque droplets.

An example of three refocused planes and a resulting measured vector field from this experiment is shown in Figure 15, demonstrating general agreement with the expected morphology of this type of secondary droplet field. From the front and top views of the same drop impact shown, the expected radial symmetry of the secondary droplet motion in all directions is evident, though several erroneous vectors can also be identified. In this previous work, statistical assessments of expected drop size and velocity were made that showed agreement with comparable DIH results, however it also identified the need for an experiment that would allow a more direct uncertainty characterization of both current and future plenoptic particle measurement capabilities, motivating the experiments and analysis described in Chapter IV. Additionally, the data set examined in this experiment contained thousands of images; the required processing time and computational resources needed to complete this analysis was large, and eventually motivated the development of the depth from perspective algorithm developed in Chapter V.

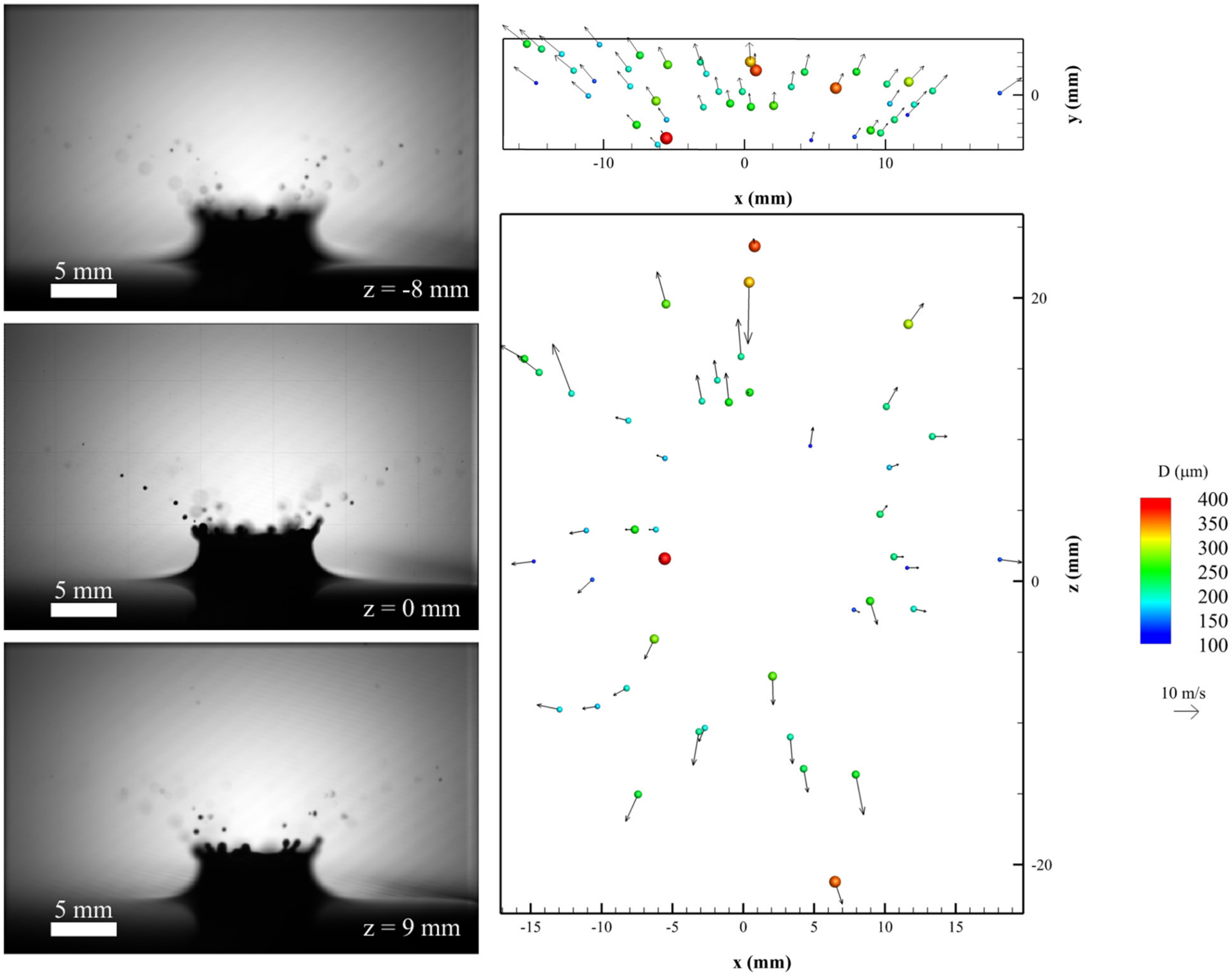

Figure 15. Drop impact image refocused to 3 different depths (left) and measured 3D droplet sizes and velocities (right).

F. Summary

Prior to the current work, light field imaging has been used extensively to create 3D representations from an instantaneously captured 2D image by the creation of refocused and perspective shifted representations of the raw plenoptic data. The adaptation of these tools to the measurement of 3D particle locations is closely related to the extensive existing work in particle tracking as particle locations determined from plenoptic images can be used as an input to particle tracking schemes similarly to the method used in other techniques. The current work is motivated by the results and unanswered questions of previous experiments in plenoptic particle tracking.

III. Volumetric Calibration

The goal of volumetric calibration of a plenoptic camera is to determine an accurate relationship between the best estimate of the true global Cartesian coordinates, defined here in (X,Y,Z), and some measure of location obtained from the plenoptic relations in the previous chapter. When locations are measured from numerically refocused images in object space defined by the thin lens equations, (x,y,z) coordinates are defined. Alternatively, the light field coordinates, (u,v,s,t), may be directly used as the initial location measurement. This chapter reviews previous light field imaging calibration efforts in literature, describes the development and implementation of three volumetric calibration methods, compares the effectiveness of these methods in terms of calibration quality and computational efficiency, and finally provides an example application highlighting the flexibility of the developed calibration.

A. Background

As the popularity of plenoptic cameras has increased, the development of calibration methods specific to light field imaging has become a growing area of research, specifically efforts to increase the accuracy of plenoptic camera based measurement techniques using both focused and unfocused plenoptic cameras [59,60]. These plenoptic calibration efforts stem from earlier work involving the calibration of multiple camera systems [61,62]. In related fields, such as stereo PIV, self-calibration methods have been developed based on volumetric methods that use measurements of the disparity between simultaneous images from multiple cameras to determine the true position of the imaging volume [63,64]. In addition to calibration of the position of different cameras, efforts have been made to correct for magnification changes due to distortion [65]. Brücker et al. have developed a method of volumetric calibration refinement for multi-camera systems based on an iterative cross-correlation of particle images and a tomographic back projection. This refinement was shown to substantially reduce disparities and improve reconstruction quality [66].

Plenoptic imaging may benefit from incorporation of similar concepts, such as correction of lens distortions. Calibration of the lenslet-based single-camera plenoptic system has required further algorithm development, which has motivated a variety of research efforts. Most of this work has been directed toward development of calibration techniques for focused plenoptic cameras due to the commercial availability of the Raytrix focused plenoptic cameras. Specifically, Heinze et al. created a calibration algorithm using a physically based model to correct lens distortions [67], and Zeller et al. used a model-based algorithm to estimate intrinsic and extrinsic camera parameters and calibrate the optical imaging process and the depth map of the plenoptic camera [68]. In further work, this was applied to a visual odometry algorithm, providing improved depth accuracy [69]. Significant developments have also been made in reducing the prior knowledge required to execute the calibration process [70]. Cho et al. made adaptations to the Lytro light field camera calibration system by implementing a learning based scheme for interpolation from the raw hexagonal microlens grid to a rectilinear light field grid. This method showed improved reconstructions as a result of the new interpolation scheme [71].

B. Calibration methods

The current work examines plenoptic camera calibration techniques that are based on the measured locations of a known dot grid imaged at a variety of depths for application to the unfocused arrangement. These concepts are similar to those used in the calibration of tomographic systems that relate the coordinate system of each camera to a global coordinate system [7]. These methods provide flexibility in experimental implementation, as detailed knowledge of specific lens parameters is not required since the calibration is based entirely on information gathered from the calibration target.

In this section, three calibration methods are presented, which differ in this choice of initial location measurement. Results show clear differences in ease of implementation and measurement uncertainty. The first calibration method discussed is based on the assumption that the main lens can be modeled as a thin lens and requires only an estimate of magnification. The other two calibration methods developed in this work are based on the measured locations of a planar grid of dots imaged at a variety of depths and their known (X,Y,Z) coordinates. A polynomial fit relates these two volumetric grids. This differs from previous plenoptic camera calibration efforts, which seek intrinsic and extrinsic camera parameters for single step correction [18]. A particular advantage of the proposed polynomial methods is their tendency to produce robust measurements within the calibrated volume. The main difference in the two fit-based methods is in the coordinate spaces being mapped. The first method, Volumetric Dewarping, determines initial measured locations in 3D object space estimated by the thin lens equation, (x,y,z). In contrast, Direct Light Field Calibration eliminates some processing needed to determine (x,y,z) and directly relates global Cartesian coordinates to plenoptic coordinates, (u,v,s,t). The use of the latter method is motivated by its applicability to multiple camera systems to allow for the concurrent calibration of two or more plenoptic cameras. Motivation is also provided by the need to correct for inaccuracies caused by lens distortion in a single camera system in a flexible manner that can be tailored to an individual experimental configuration.

i. *Simple thin lens based calibration*

Prior to this work, a majority of 3D plenoptic measurements have been based on the assumption that the main lens can be approximated as a thin lens with focal length, f. Magnification at the nominal focal plane is then defined as $M = -l_i/l_o$. By similar triangles, this is equivalent to $M = -h_i/h_o$ or the ratio of image height to object height. These heights are used in practice as they can be easily estimated from the raw image. The thin lens equation can also be used to determine the image space location of an object at any other distance from the lens. In this case, the object and image distances in the thin lens equation are replaced by the virtual object and image distances, l'_o and l'_i, respectively. By convention, object distance from the lens is defined relative to the nominal focal plane by the parameter z where positive distances are farther from the camera. By combining these relations with the thin lens equations, it can be shown that,

$$(x,y,z) = \left(\frac{(s-u)\alpha + u}{\alpha(1-M)-1}, \frac{(t-v)\alpha + v}{\alpha(1-M)-1}, f\left[\frac{1}{M} + \frac{1}{\alpha(1-M)-1} \right] \right), \tag{5}$$

where α is formally defined as $\alpha = l'_i/l_i$,. Note that when $\alpha = 1$, Equation (5) reduces to a scaling of the location on the image sensor, (s,t), by the nominal magnification. For other values of α, these equations scale the in-plane location based on the effective magnification at the corresponding depth. A detailed derivation of this relationship can be found in Appendix A: Thin lens plenoptic coordinate conversion. The advantage of this method is simplicity and convenience as the only physical measurement required is an estimate of the magnification at the focal plane, which, in some experimental configurations, is the only practical measurement.

ii. *Volumetric dewarping*

In the development of a volumetric calibration using a plenoptic camera, there is an option to use either refocused or perspective view images as the basis for measuring calibration points. In the first implementation, referred to here as Volumetric Dewarping (VDW), refocused images were chosen due to the obvious way depth is captured and because existing algorithms can be used to determine depth from these images. This method of calibration involves the creation of a 3D volume made up of a series of refocused images, termed a focal stack, based on the expected light-ray locations using thin lens geometric assumptions as described in the previous subsection. This volume is then dewarped in post-processing. The first step in this process is the formation of a focal stack from the raw images captured of a calibration target dot card at each depth. Next, (x,y,z) locations of the dots in each focal stack are measured. This is automated using a modified version of the processing algorithm defined in Guildenbecher et al. [72], which is a hybrid particle detection method combining minimum intensity and maximum edge sharpness methods. Next, the true global Cartesian locations of the dots, (X,Y,Z) are determined from the known dot card dimensions. A third-order 3D polynomial function is defined to relate measured (x,y,z) to true (X,Y,Z):

$$\begin{aligned}(X,Y,Z) = {} & a_0 + a_1x + a_2y + a_3z + a_4xy + a_5xz + a_6yz + a_7x^2 + a_8y^2 + a_9z^2 + a_{10}x^2y \\ & + a_{11}x^2z + a_{12}xy^2 + a_{13}y^2z + a_{14}xz^2 + a_{15}yz^2 + a_{16}xyz + a_{17}x^3 + a_{18}y^3 + a_{19}z^3\end{aligned}, \tag{6}$$

where $a_{0\text{–}19}$ are the polynomial coefficients found using nonlinear optimization in MATLAB. Finally, this mapping is used to dewarp any focal stack calculated in (x,y,z) coordinates into (X,Y,Z) coordinates again using MATLAB routines. This method provides a logical improvement on the thin lens based method, however, the requirement for the creation of a large focal stack for each image makes it computationally expensive. This motivates the development of the Direct Light Field Calibration method discussed next.

iii. Direct light field calibration

The third technique is a more direct method of calibrating the recorded light field. Instead of dewarping the volume as a postprocessing step, the calibration data is used in the generation of the reconstructed volume. In essence, the goal of this calibration technique is to determine a mapping from any point in (*X*,*Y*,*Z*) space to a light field coordinate *L*(*u*,*v*,*s*,*t*). This mapping is shown schematically in Figure 16, where light rays are shown relating known calibration points in (*X*,*Y*,*Z*) space to locations on the aperture and microlens planes. The colored light rays indicate rays traveling through different points on the aperture from the four known calibration points.

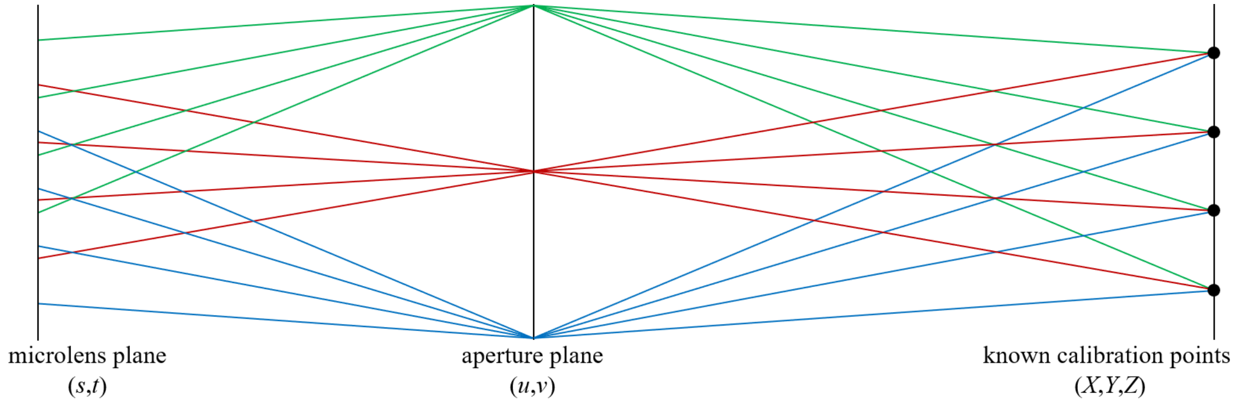

Figure 16. Schematic depiction of the mapping between object space coordinates and image sensor coordinates using the two plane parameterization.

These aperture locations can be easily isolated by rendering perspective views with fixed (*u*,*v*) coordinates. Finally, the corresponding (*s*,*t*) coordinates can be determined by locating the calibration point in each perspective image. The mapping constructed through the calibration procedure must provide the same projection as the original refocusing equation, Equation (3), and since the calibration points are defined in (*X*,*Y*,*Z*) space, the new mapping will skip the translation to image space and project directly from object space to the microlens plane. Therefore, the mapping function $\mathcal{P}$ is defined as a function mapping a point in object space projected to a point on the microlens plane, i.e.,

$$(s,t) = \mathcal{P}(X,Y,Z,u,v)\,. \tag{7}$$

The identification of points in object space and determination of the corresponding locations on the microlens array is the basis of this algorithm. To determine the location of the projection, the incoming light field must be isolated at an assumed aperture location, which can be executed by exploitation of the capability of the plenoptic camera to generate unique perspective views at different (u,v) positions. These images can then be used to determine the location of the projection at the microlens plane. For each dot card location, or Z position, a range of perspective images is generated. Then for each of these images the locations of every dot, in (s,t) space, is determined and recorded. Once all the dot locations are determined for each perspective view at every depth location, a matrix A is generated using the object locations and the angles of the projection (X,Y,Z,u,v). The corresponding projection locations are placed into two vectors **s** and **t**. Then the coefficients are determined in a least-squares sense by solving the system of equations $\mathbf{a_s} = \mathbf{A}/\mathbf{s}$ and $\mathbf{a_t} = \mathbf{A}/\mathbf{t}$. When generating the reconstructed volume using the light field calibration data Equation (3) is rewritten as,

$$E(s',t') = \iint L\big(u,v,\mathcal{P}_s(X,Y,Z,u,v),\mathcal{P}_t(X,Y,Z,u,v)\big)A(u,v)\,du\,dv\,, \tag{8}$$

thus replacing the linear projection operations with a best-fit polynomial. Conceptually this can be compared to treating each perspective view as a separate camera, except that all of the calibrations are consolidated into a single polynomial. The user selects (u,v) locations, and the projection operator relates (X,Y,Z) to (s,t). The replacement of the original linear projection operations removes the assumption of a thin lens and a camera perfectly aligned with the volume of interest. Additionally, rather than explicitly attempting to correct for microlens aberrations, this implementation assumes ideal (u,v) coordinates based directly on pixel coordinates measured relative to the microlens centers and wraps the combined effects of main lens and microlens aberrations into a single correction. Again, a third-order mapping function is chosen:

$$\begin{aligned}\mathcal{P}(X,Y,Z,u,v) = a_0 &+ a_1X + a_2Y + a_3Z + a_4u + a_5v + a_6X^2 + a_7XY + a_8XZ + a_9Xu + a_{10}Xv \\ &+ a_{11}Y^2 + a_{12}YZ + a_{13}Yu + a_{14}Yv + a_{15}Z^2 + a_{16}Zu + a_{17}Zv + a_{18}u^2 + a_{19}uv + a_{20}v^2 \\ &+ a_{21}X^3 + a_{22}X^2Y + a_{23}X^2Z + a_{24}X^2u + a_{25}X^2v + a_{26}XY^2 + a_{27}XYZ \\ &+ a_{28}XYu + a_{29}XYv + a_{30}XZ^2 + a_{31}XZu + a_{32}XZv + a_{33}Xu^2 + a_{34}Xuv + a_{35}Xv^2 \\ &+ a_{36}Y^3 + a_{37}Y^2Z + a_{38}YZ^2 + a_{39}YZu + a_{40}YZv + a_{41}Y^2u + a_{42}Yu^2 + a_{43}Yuv \\ &+ a_{44}Y^2v + a_{45}Yv^2 + a_{46}Z^3 + a_{47}Z^2u + a_{48}Zu^2 + a_{49}Zuv + a_{50}Z^2v + a_{51}Zv^2 \\ &+ a_{52}u^3 + a_{53}u^2v + a_{54}uv^2 + a_{55}v^3\end{aligned} \quad ,(9)$$

where 56 coefficients are required. A detailed guide explaining the procedure for the experimental collection of calibration data, determination of calibration mapping functions, and application of calibration to experimental data using DLFC is given in Appendix B: DLFC guide.

C. Experimental verification

An experimental comparison of the calibration methods was made by imaging a calibration target with a square grid of dots 1.25 mm in diameter and with a spacing of 5 mm. This target was placed at a variety of angles and a variety of depths from the camera as shown in Figure 17, and the volume was reconstructed using each calibration method. This specific configuration was selected for applicability to a multiple plenoptic camera experiment in which each camera would view a volume at an angle and a common coordinate system would be selected to combine the information from all cameras. Sets of images were captured with the camera placed at angles of θ = 0, 10, 20, 30, and 40 degrees from perpendicular to the dot card plane. Angles were determined based on the placement of the camera along the axes shown horizontally and vertically in the figure, which are estimated to be accurate within ±0.5 mm based on the precision of the linear traverse. Propagation of uncertainty is used to estimate the angular accuracy to be approximately ±0.01 degree. At each position, the camera was nominally focused on the center of the dot card at its origin location. Then the dot card was traversed along the direction indicated in Figure 17, and images were captured at 1 mm increments along this axis at locations ±25 mm from the origin location. The traverse direction is defined as the *z* direction and is oriented such that positive values are farther from the camera than the origin location, and negative values are closer to the camera than the origin location. The translation stage utilized was a Newport UTS50CC High-Performance Precision Translation Stage that had a total travel distance of 50 mm and a specified absolute accuracy of ±4.5 μm.

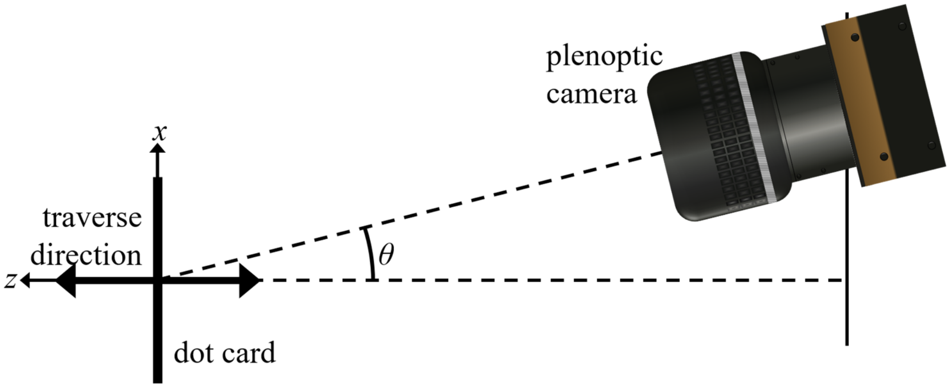

Figure 17. Experimental configuration depicting camera placement relative to the dot card and traverse.

The dot cards located at $z = -25, -20, -15, -10, -5, 0, 5, 10, 15, 20$, and 25 mm were used as a training set to calculate the mapping functions for both the VDW and DLFC methods. To quantify the results, the mapping function was used to calculate corrected volumes from dot card images not used to create the mapping function. Calibrated volumes were created for dot card images located at $z = -23, -13, -3, 3, 13$, and 23 mm at each of the 5 dot card angles resulting in 30 calibrated volumes for each calibration method.

To provide a quantitative analysis of the calibration accuracy, sharpness was used to measure the locations of the dots in the resulting calibrated volumes under the assumption that the dots have the sharpest edges at the in-focus plane. As a reference of scale, the average error in the depth direction using the thin lens calibration at an angle of 0 degree was 0.51 mm with some error magnitudes of up to 6.7 mm. The in-plane volume size was approximately 52 by 78 mm with a volume depth of 50 mm. Generally, depth error increased with distance from the focal plane. It should be noted that the following discussion places an emphasis on error in the depth direction as it is expected to be the most significant due to the limited range of collection angles from which plenoptic images are captured. This range is limited by the size of the main lens aperture. Additionally, values for the thin lens calibration are considered only for the 0 degree case, as this method is not intended to correct for rotation of the dot card.

Examination of these errors was executed by determining the average and standard deviation of error in each direction as a function of the depth of the dot card. Figure 18 displays the average errors for each method used as a measure of accuracy, all normalized by the size of a microlens in object space. In the analysis of this data set, the results from each angle were examined separately, and similar trends were noted in each. The depth error resulting from the thin lens calibration based on manually estimated magnification is larger than the error resulting from the volumetric calibration methods and follows a general direct relationship with depth; however, this trend is not precisely centered at the focal plane. This trend may be a result of a curvature of field aberration not accounted for in the simple thin lens based calibration, or it may be a systematic error because of the rough estimation of magnification and the nominal focal plane location. The accuracy measurements for simple calibration span a range of 5.06 mm as compared to ranges of only 0.70 mm and 0.66 mm for VDW and DLFC, respectively. Additionally, the overall averages for the simple calibration, VDW, and DLFC are 0.51 mm, 0.29 mm, and 0.21 mm, respectively (equivalently 3.2, 1.8, and 1.3, respectively, when normalized by the size of the microlenses). This suggests that similar accuracy is achieved using either VDW or DLFC.

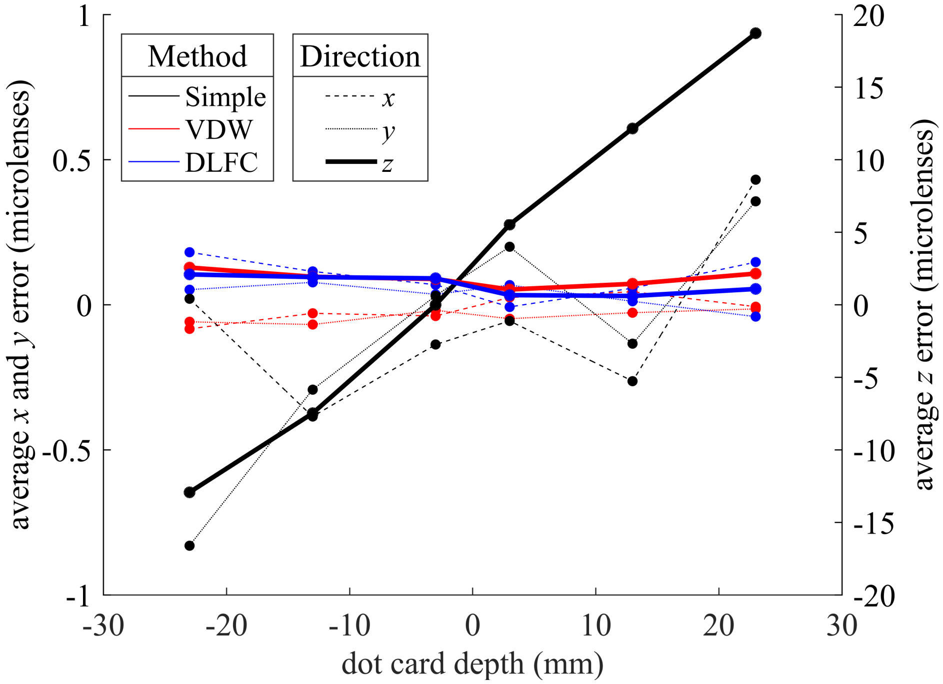

Figure 18. Average depth error for each method and direction as a function of dot card depth.

Figure 19 displays the standard deviations of error for each method for all configurations used as a measure of precision. Results demonstrate significant improvement in precision using either volumetric calibration method when compared to the simple thin lens results. In the simple calibration case, the precision measurement was as large as 1.34 mm, while the largest values for VDW and DLFC were 0.80 mm and 0.76 mm, respectively. The average precision of depth error for the simple calibration, VDW, and DLFC are 0.83 mm, 0.53 mm, and 0.52 mm, respectively (equivalently 5.2, 3.3, and 3.3, respectively, when normalized by the size of the microlenses). This suggests that precision is similar using either volumetric method.

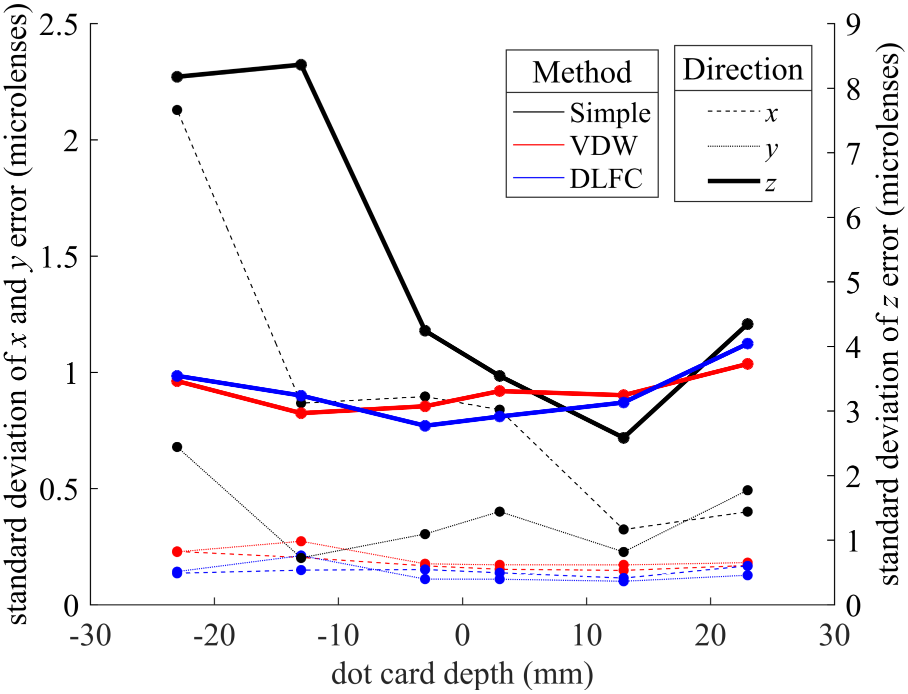

Figure 19. Standard deviation of depth error for each method and direction as a function of dot card depth.

In an effort to further examine the possible effect of an inaccurate estimation of magnification in implementing the simple thin lens calibration, this method was executed using a variety of magnifications within a small range of the initial estimate. Based on examination of average error for each of these magnifications, it was determined that the ideal magnification to minimize depth error for this data set was 0.45 (the original estimate was 0.48), which resulted in average errors as displayed in Figure 20. This demonstrates that some depth accuracy improvement can be gained by optimizing the selected magnification; however, this requires examination of dot cards at a variety of depths in addition to the magnification estimation. The in-plane errors were actually increased in some cases, though not as dramatically as the depth error was changed. Additionally, the error measured using this ideal magnification remains larger than that achieved using VDW or DLFC, indicating that the higher-order terms included in these polynomial-fit based methods play an important role in accuracy improvement.

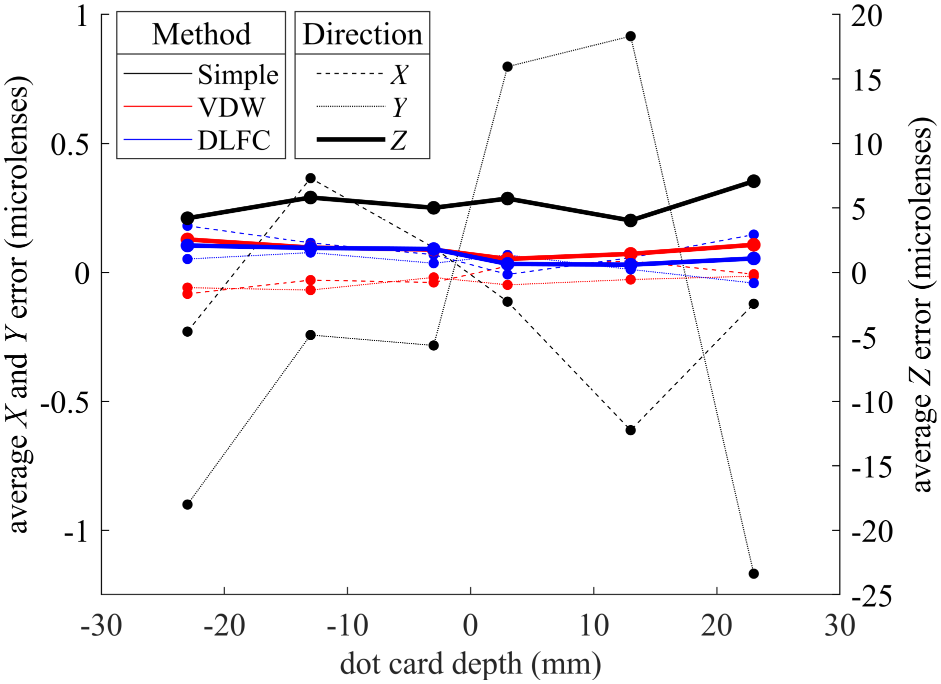

Figure 20. Average depth error for each method as a function of dot card depth. An optimized value of magnification was used in implementation of the simple thin lens based calibration. The data for the polynomial based fit methods is the same as in Figure 18.

In the examination of this data it is also relevant to consider the effect of varying dot card angle, which effectively results in a translated coordinate system. In the unrotated case, the *Z* axis physically lies along the optical axis of the camera. As the angle is increased, these two axes become more separated, and the direction of the optical axis is actually represented partially by the *X* and *Z* axes. Therefore, due to the known reduction in accuracy along the optical axis, it is expected that as the rotation angle is increased the accuracy in the *Z* direction would improve as accuracy in the *X* direction worsens. This trend, although slight, is displayed in Figure 21, where the average error in each direction for VDW and DLFC is shown as a function of angle.

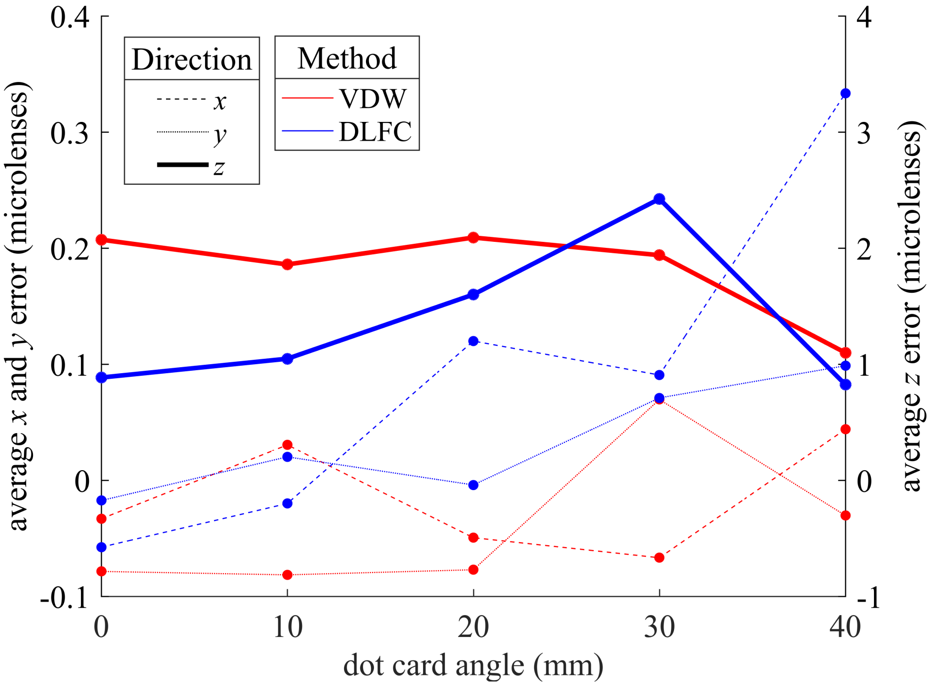

Figure 21. Average depth error for each method and direction as a function of dot card angle.

D. Computational requirements

Considering the similarities in the measurement error using either volumetric method, the computational requirements of each become a significant factor in the comparison. The computational requirements of implementing either method in comparison to the previous simple calibration should also be noted. The measurements presented here represent an initial MATLAB implementation, which has not been optimized to minimize computational time. For this reason, we choose not to compare our processing performance with alternative techniques (e.g., [67]).

The first step in data processing is the creation of the mapping function, a step not required in the simple calibration method. The main difference between the two volumetric methods in this step is in the requirement in VDW to create a focal stack of each dot card image and extract dot locations from these focal stacks before determining the mapping function. In this experiment, this process took approximately 6 hours parallelized in MATLAB on a 12-core desktop computer.

Then, the user must spend about 10 min selecting the correct center dots from each focal stack. In comparison, DLFC determines the dot card locations from perspective shifted images, which can be calculated significantly faster than refocused images. In this case, the creation of the perspective shifted images and determination of the mapping function takes about 20 minutes total, again including about 10 minutes of center dot selection by the user. It should be noted that these differences in computational time do not represent an overall comparison of the two methods, as the process of creating the mapping function must only be done once for a given data set. Comparison of the computational requirements necessary for creating data focal stacks is more critical in determining the overall computational time, particularly in the processing of large data sets. DLFC also requires less computational time in this portion of the processing; however, by a narrower margin. In comparison to creation of a focal stack using the simple calibration method, creation of a focal stack followed by application of the VDW takes approximately 114% as long, while creation of a corrected focal stack using the DLFC mapping takes approximately 109% as long. In the focal stacks used in this experiment, this equates to a difference of about 2 minutes per image between VDW and DLFC. Though this difference is smaller individually, it is the more significant indication of the total processing time required and indicates the improved computational efficiency of the DLFC method over VDW.

E. Example application: calibration of a spherical surface

The experiment described in the previous section is based on a configuration in which imaging of a planar region is desired; however, this type of calibration can be applied to other configurations including imaging of a curved surface. This further increases the flexibility of plenoptic imaging to include applications such as the analysis of curved regions within an engine or measurement of properties along a curved airfoil. As an example of this capability, a simple experiment was conducted in which a globe was imaged and DLFC was applied to map the curved surface of the globe to a single image plane. This experiment was arranged similarly to the dot card experiment as shown in Figure 22.

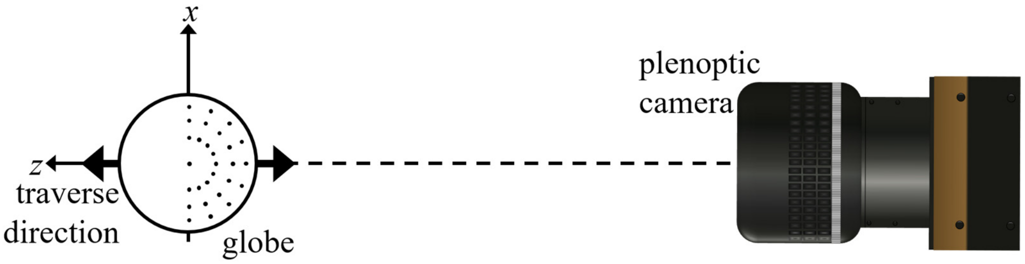

Figure 22. Spherical calibration experimental configuration.

Dots were drawn on the intersections of the latitude and longitude lines in increments of 10 degrees and 15 degrees, respectively, and the globe was imaged at a variety of depths to create a set of calibration points. Calibration was executed by simply replacing the Cartesian coordinates (X,Y,Z) with (latitude, longitude, 0) since we were interested in the reconstruction of a single spherical plane at the surface of the globe. The results of this calibration are demonstrated in Figure 23, which shows refocused images using the simple thin lens based calibration and a spherical implementation of DLFC based on dots at the latitude and longitude grid intersections. Comparison of the two images clearly demonstrates the viability of calibration based on nonplanar surfaces. In addition, this result rather clearly demonstrates the ability of the proposed techniques to remove what is effectively a severe image distortion.

Several points should be made in further examination of the spherical calibration result. First, this experiment was intended as a demonstration of flexibility only, and a perfect grid was not expected. Since the dots were drawn by hand, they are not guaranteed to be aligned in a perfect rectilinear pattern or to be exactly circular. Additionally, the printed latitude and longitude lines appeared to have significant alignment inaccuracies, specifically at the seam on the equator, again contributing to an imperfect grid. Despite these issues, this figure confirms that our implementation of volumetric calibration using a plenoptic camera can be used to create an image of a nonplanar surface from a single raw plenoptic image. In particular, comparison of the edge regions of these two images shows that regions that are significantly blurred in the planar calibration are brought into focus in the spherical calibration, and additional details, specifically text, can be discerned after application of this calibration.

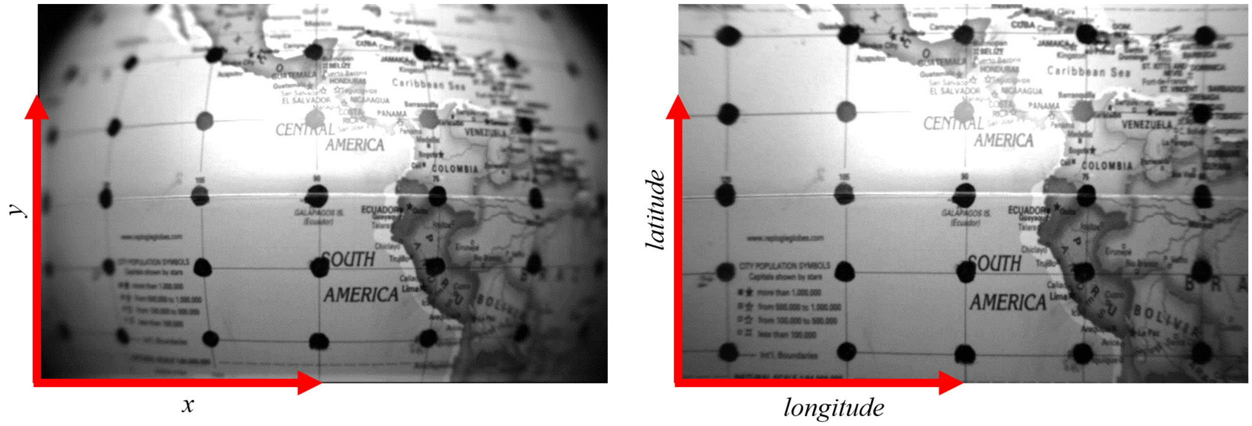

Figure 23. Spherical dewarping of a globe demonstrating an image with standard planar calibration (left) and spherical calibration (right).

F. Summary

Three methods of volumetric calibration have been implemented and examined for accuracy and precision as well as computational efficiency. The thin lens based method resulted in significant errors as compared to the two methods based on a 3D polynomial mapping function created using information gathered from a known set of dot card images. The Volumetric Dewarping method uses a polynomial mapping to correct an un-calibrated volume while the Direct Light Field Calibration method uses a polynomial mapping to create a calibrated volume directly from raw plenoptic data. An experiment was designed to test the reconstruction accuracy achievable using these two methods in which images of a dot card were captured at a variety of angles and the calibration algorithms were used to create corrected volumes in which the camera viewing angle was apparently perpendicular to the dot card. The results of this experimental comparison demonstrate a similar increase in reconstruction accuracy using either method. In the calibrated volumes created using each method the depth location of individual dots was measured on average to within 0.5 mm of their actual known location, representing a 1% error in the depth direction based on the reconstructed volume size. The errors in the x and y directions are approximately an order of magnitude smaller. In comparison, the errors in the thin lens calibrated volumes in this experiment averaged 1.67 mm in the depth direction, with some errors as large as 8 mm. Though the improvement in depth accuracy achieved by application of these calibration methods is significant, further improvement may be possible through further work examining the selection of the mapping functions order and organization.

IV. Depth from focus

The initial algorithm developed in this work for the determination of object depth utilizes the refocusing capability of the plenoptic camera due the straightforward volumetric representation created by a series of refocused images, termed a focal stack. Additionally, refocusing allows the use of established processing methods for particle measurement as plenoptic focal stacks can be processed in a manner similar to Digital In-line Holography (DIH) processing methods.

A. Algorithm development

The determination of depth from focus processing scheme begins with the creation of a focal stack from the raw plenoptic image. In the implementation discussed here, Volumetric Dewarping was applied to each focal stack as described in Chapter III Section B Subsection ii. After dewarping, the 3D location of each particle was measured from the focal stack using a modified version of the DIH processing algorithm defined in Guildenbecher et al. [72], which is a hybrid particle detection method combining minimum intensity and maximum edge sharpness methods. In the minimum intensity method, it is assumed that the intensity of the particle is lowest at the in-focus depth, while the maximum edge sharpness method assumes that the sharpness of the particle edge, measured using the Tenengrad operator, is highest at the in-focus depth. In that previous study, it was determined that using a minimum intensity map to locate particles produces accurate shape and in-plane location information while using a measure of maximum edge sharpness is more useful in determining the depth location.

These methods were combined by first calculating a minimum intensity map of the volume and applying a variety of thresholds to this map. To provide flexibility and allow processing of images with inconsistent illumination across the entire field of view, an additional processing step was included in which the images were divided into smaller regions and an optimum intensity threshold was selected for each region. Using these varied thresholds, a group of possible particles was detected. Next, the sharpness for each edge was calculated by averaging the Tenengrad values for the pixels on each edge, and the edge with the maximum sharpness was selected as the in-focus edge. The depth of the particle was then determined from the average depth location of the selected edge [72]. Once located in 3D space, individual diameters were measured from the refocused image of each particle. Finally, particle velocities were determined based on a nearest neighbor matching between the 3D particle fields.

B. Theoretical limitations

Measurement accuracy is hypothesized to be strongly correlated with the spatial resolution and depth of field of the plenoptic camera. Due to the use of the microlens array and the unique post-processing methods, the definition of these metrics is slightly more complex compared to traditional photography.

Figure 24 illustrates a simple plenoptic camera in which five pixels lie behind each microlens. The color bands in the top schematic illustrate the angular regions captured by each individual pixel. As detailed in [14], a numerically refocused image is calculated by integrating all of the light which originates from the plane of interest into spatial regions discretized by the microlenses. For example, refocusing to the nominal focal plane of the main lens aperture sums the intensity of each of the illustrated pixels to determine the refocused intensity at the center of the image. The theoretical depth of field of such a numerically refocused image at the nominal focal plane is derived by Deem et al. [73] as,

$$\Delta z = \frac{f(M-1)^2}{M(M-1) - f_\mu N / f(N-2)} - \frac{f(M-1)^2}{M(M-1) + f_\mu / f}, \tag{10}$$

where f is the focal length of the main lens, M is the nominal magnification, f_μ is the focal length of the microlenses, and N is the number of image sensor pixels behind each microlens in one dimension (calculated as the microlens pitch, p_μ, divided by the pixel pitch, p_p). In this work, particle depths are determined from the sharpness of numerically refocused images. Therefore, it is hypothesized that Equation (10) will bound the measured particle depth precision, and this quantity is referred to as the theoretical depth resolution, Δz.

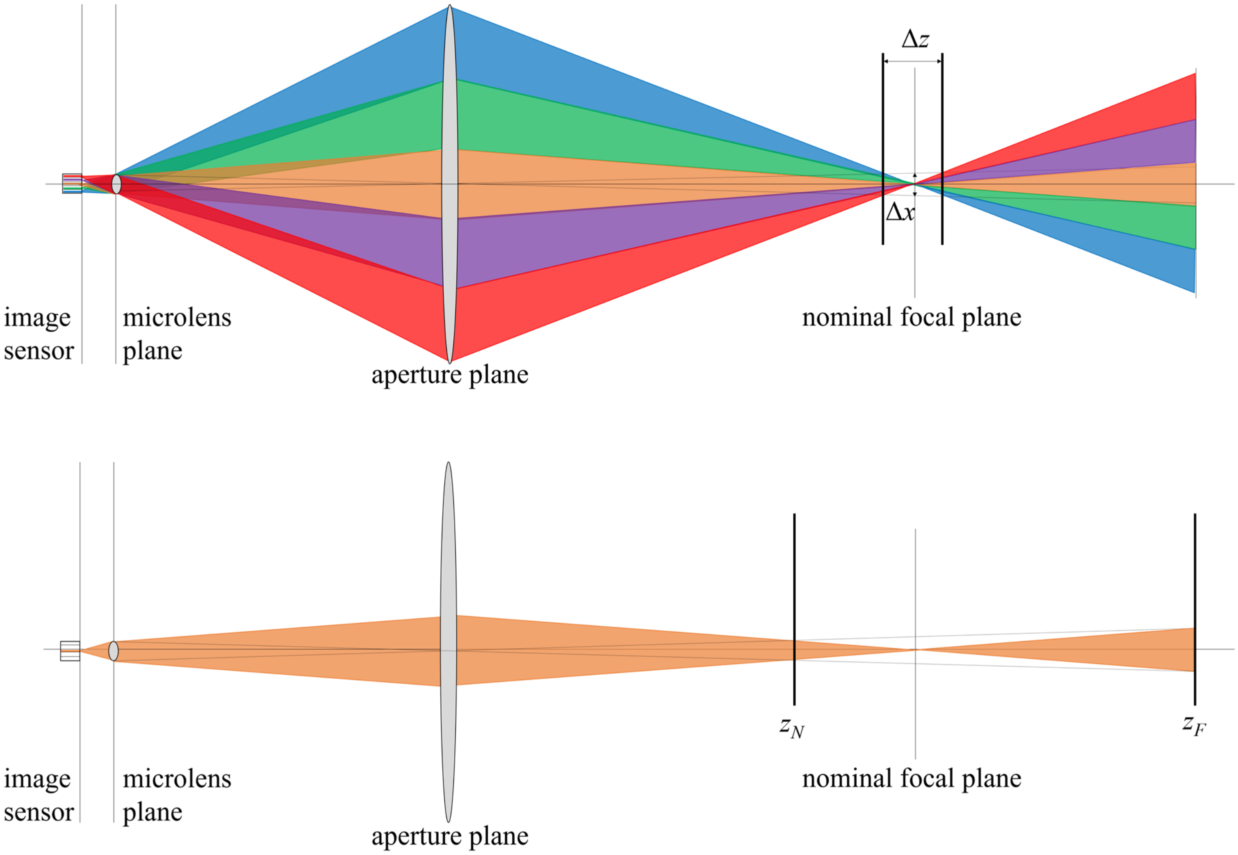

Figure 24. Illustration of the theoretical depth resolution, Δz, (top) and the total depth range (bottom). A numerically refocused image (top) is determined by integrating the intensity of all light rays which pass through the main lens aperture and has a relatively narrow depth of field. In contrast, the narrow aperture of a single pixel (bottom) determines the effective depth range over which numerically refocused images remain sharp.

In-plane resolution of plenoptic imaging is also examined by Deem et al. [73] using ray-tracing of the light incident on a microlens. Since all light rays incident on a particular microlens reach the same image sensor pixels, any light rays emanating from the corresponding object space location have indistinguishable spatial locations in that dimension [73]. The size of this object space location is determined by the nominal magnification of the system and the microlens pitch,

$$\Delta x = p_{\mu} / -M \, . \tag{11}$$

In this work, in-plane particle positions are measured from the refocused images with Equation (11) defining the theoretical bounds of precision.

Finally, it is important to quantify the range of z depths over which measurements are expected to remain accurate. A numerically refocused image can only be rendered as sharp as the sub-images from which it is determined [14]. These sub-images are discretized by the individual pixels, and, as illustrated in the bottom row of Figure 24, the small effective aperture results in a relatively large effective depth of field. This is calculated by first determining the diameter of the N times smaller aperture, $D = p_p \cdot l_i / f_\mu$, where l_i is the image distance of the main lens. Given additionally that the size of the circle of confusion is equivalent to the in-plane resolution calculated in Equation (11), the depth of field of the sub-images can be determined from a standard depth of field equation as,

$$DOF = \left[\frac{D l_o}{D - \Delta x} - l_o \right] - \left[\frac{D l_o}{D + \Delta x} - l_o \right], \tag{12}$$

where l_o is the object distance of the main lens. From this equation we can also define the near and far limits of the depth of field, z_N and z_F respectively as,

$$z_N = \left[\frac{D l_o}{D + \Delta x} - l_o \right] \text{ and } z_F = \left[\frac{D l_o}{D - \Delta x} - l_o \right]. \tag{13}$$

When numerically refocused images are calculated, any particle contained within $z_N \leq z \leq z_F$ is expected to come into sharp focus at its corresponding optical depth. Therefore, Equation (13) defines the theoretical range of optical depths over which particle measurements should remain accurate. The current work focuses on macroscopic applications of plenoptic imaging in which the microlenses and pixels are larger than the relevant diffraction limited spot size. This is contrasted with microscopic applications, such as those discussed by Truscott et al. [26], Levoy [74], and Pepe et al. [75] where spatial resolution and depth of field may be better predicted by diffraction limited models. While the methods provided here may guide future investigations of the uncertainty of diffraction limited applications, the detailed quantitative results are likely to differ. It is hypothesized that the precision of individual particle measurements in the out-of-plane, z direction and the in-plane, x and y directions will correlate with Equations (10) and (11), respectively. In addition, the total depth range over which measurements will remain accurate is bounded by Equation (13).

C. Experimental configuration

In previous work focused on experimental uncertainty quantification of related measurement techniques, well-defined 3D calibration fields have been created using neutrally buoyant particles immersed in liquids [76] or objects fixed on glass slides [77]. While similar techniques could be employed here, the refraction of light through material interfaces combined with the unique manner in which plenoptic cameras utilize angular information, would result in image aberrations that must be corrected. To avoid this, the current work focuses on a particle field in which all recorded light rays pass through a common index of refraction medium, namely air. This is achieved using the experimental configuration photographed in Figure 25.

A rigid particle field is simulated by the heads of straight pins (roughly 2.4 mm diameter) inserted at random orientations into a rigid foam ball (approximately 115 mm diameter). To reduce reflections and increase the ease with which the pin heads can be segmented from the background, the shafts of the straight pins are painted white. Finally, the scene is illuminated by three continuous green LEDs with diffusers placed to reduce shadows created by the pins.

Precisely known displacements along the optical depth direction, z, were created by affixing the particle field to an automatic translation stage as shown in Figure 25. The stage had a total travel distance of 50 mm with an absolute accuracy of ±4.5 µm. The plenoptic camera was positioned such that the optical axis was parallel to the translation axis.

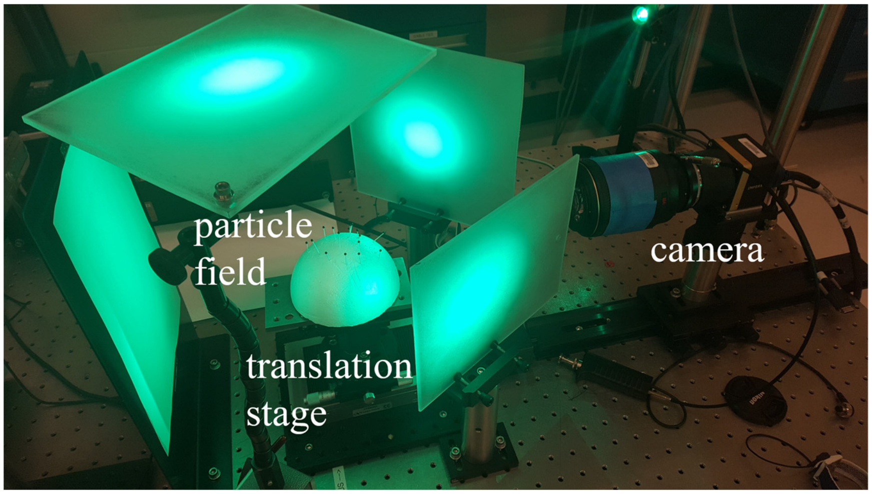

Figure 25. Photo showing the static particle apparatus and plenoptic cameras experimental configuration.

To explore the scaling of measurement accuracy with Equations (10) - (13), data was collected at four different magnifications of 0.25, 0.35, 0.5, and 0.75 achieved by adjusting the focus of the main lens and the separation distance between the camera and the particle field. Table 1 summarizes the experimental configurations along with the theoretical depth of field, depth resolution, and in-plane resolution.

For some conditions in Table 1, the predicted DOF, over which measurements are expected to retain their accuracy, exceeds the 50 mm travel distance of the translation stage. To extend the experimental range, data was collected with the camera at three different distances from the particle field as shown in Figure 26. In the middle configuration, the particle field was centered at the nominal focal plane, in the near configuration it was centered 50 mm closer to the camera, and in the far configuration it was centered 50 mm farther from the camera. This resulted in a total of 12 configurations of magnification and depth.

Table 1. Experimental configurations and theoretical measurement performance.

M	l_o (mm)	DOF (mm), Equation (12)	Δz (mm), Equation (10)	Δx (µm), Equation (11)
0.25	525	140.4	10.7	308
0.35	405	70.9	5.4	220
0.5	315	34.6	2.6	154
0.75	245	15.3	1.2	103

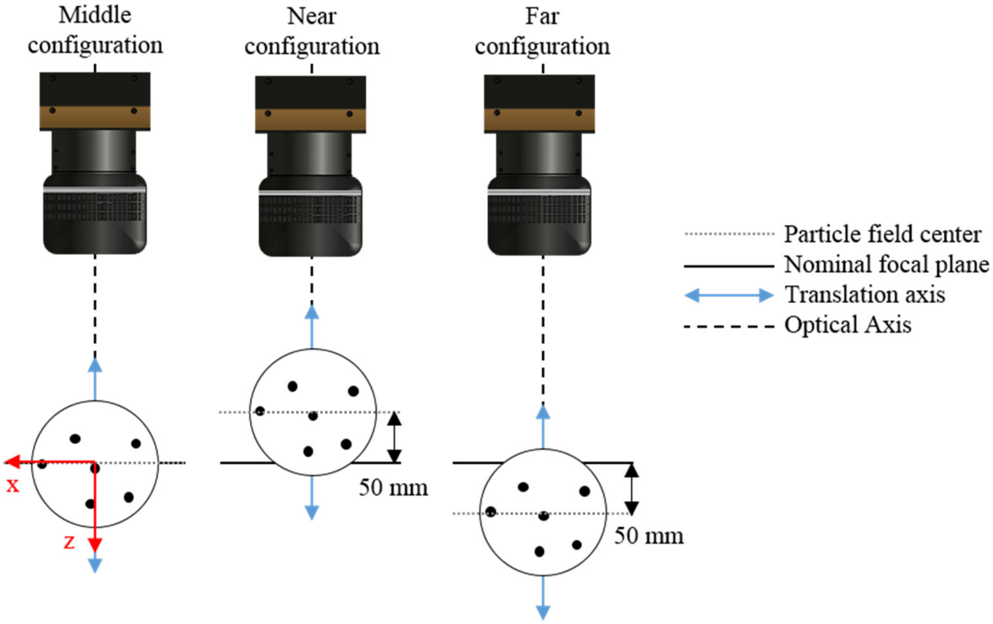

Figure 26. Experimental configuration depicting the three measurement distances used to extend the translation range.

In an experiment, the particle field was translated over the full range of the translation stage with images captured every 1 mm. Following this, the pins were randomly repositioned to ensure independent data sets, and the experiment was repeated 50 times. This process was performed for every magnification and every depth offset, resulting in over 30000 raw images. Additionally, in each configuration, a set of dot card images was collected so that volumetric calibration could be applied.

D. Uncertainty characterization

The following results and analysis are based on error in the displacements measured from the computational manipulation of the plenoptic images. To provide context for these results, example images from two of the configurations are included here. Figure 27 displays three different focal planes from an image with a magnification of 0.5. Figure 28 displays the same three planes, relative to the focal plane, from an image with a magnification of 0.25. As a reminder, each of these sets of three images is created from a single instantaneous raw image; therefore, the apparent translation through space is a computational effect, not physical movement of the experimental apparatus.

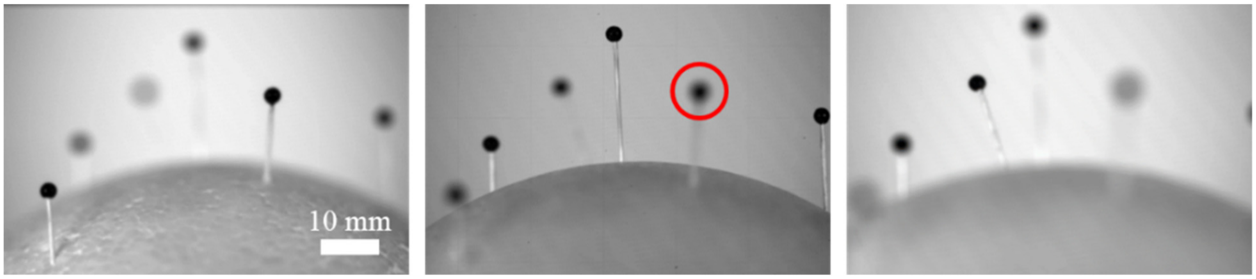

Figure 27. Example refocused images from the middle depth configuration with a nominal magnification of 0.5. Relative to the nominal focal plane, these images are focused at -25 mm (left), 0 mm (middle), and 25 mm (right). The circled particle is used as an example of the error calculation method.

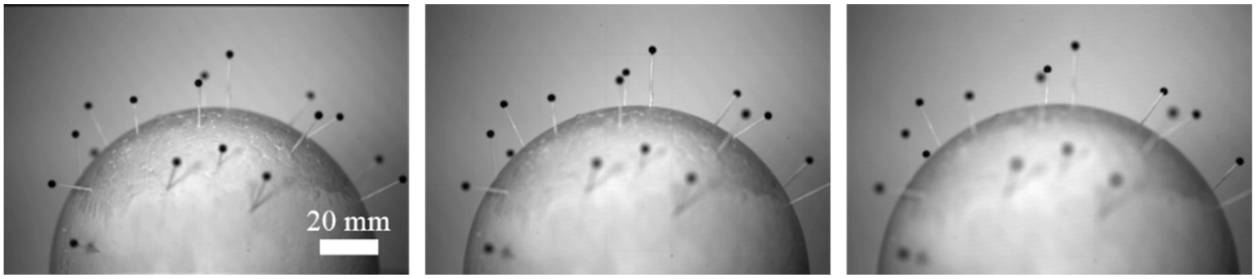

Figure 28. Example refocused images from the middle depth configuration with a nominal magnification of 0.25. Relative to the nominal focal plane, these images are focused at -25 mm (left), 0 mm (middle), and 25 mm (right).

Visual examination of these images shows that the three-dimensionality of the scene is clearly captured by this diagnostic as indicated by various particles appearing in-focus at different optical depths. Additionally, comparison of the two figures demonstrates the scope of this experiment as the field of view is significantly larger when magnification is decreased.

From these focal stacks, particle locations were measured as shown in Figure 29, which displays the center image at $z = 0$ mm from Figure 28. This is overlaid with bright squares showing the in-focus image of each particle at the determined depths. It should be noted that the blurred image of each particle appears in different in-plane positions in the $z = 0$ mm image due to the change in effective magnification as a function of depth. Particle diameter is indicated by color.

Figure 30 displays an isometric and in-plane view of the particle locations and measured displacements extracted from two images of the data set shown in Figure 28. The known displacement between the two images was 20 mm. Measured displacement is indicated by vector length and color. From visual examination of these two views, some variation in the measured z displacement is evident as expected. It should also be noted that the measured particle diameters, shown by the grey scale, fall within a relatively narrow range of 2.35-2.5 mm. This range is reasonable based on the average diameter of 2.4 mm with a standard deviation of 0.06 mm determined using calipers.

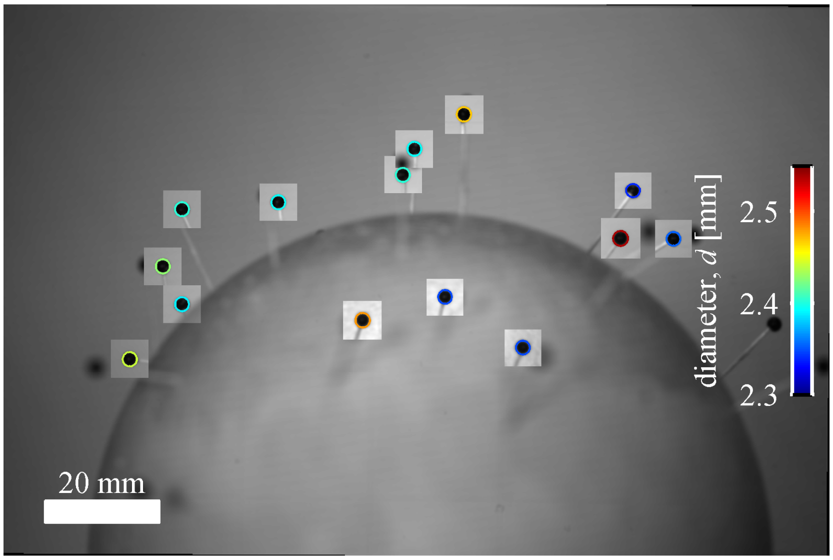

Figure 29. Example of measured particle locations, diameter indicated by color.

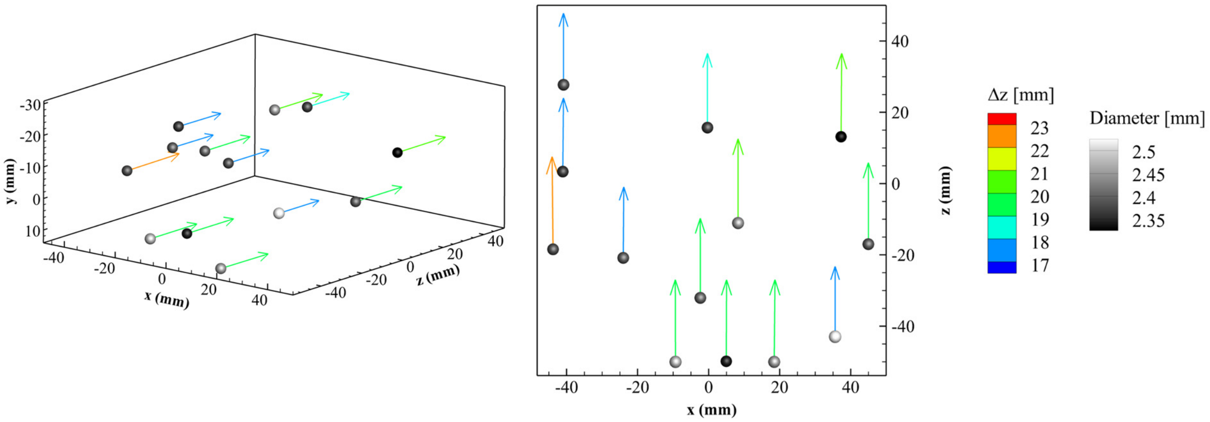

Figure 30. Isometric (left) and planar (right) views of measured particle and displacements from the middle configuration with a magnification of 0.25.

The experimental error in particle depth measurements is determined in relation to the specified positions of the translation stage. Because the location of the nominal focal plane with respect to the $z = 0$ traverse position is not known with sufficient accuracy, this offset is determined with a data fitting procedure. Figure 31 demonstrates the analysis for the particle circled in the middle image in Figure 27. First, the z position of this particle is measured in each of the 51 images and a preliminary linear fit between these measurements and the corresponding traverse locations is determined. Next, a preliminary depth error is determined as the distance of each measurement from the linear fit. Any measurements producing a depth error of more than 5 mm are defined as outliers and removed to avoid their effect on the fit intercept. (Of all measurements, only approximately 0.03% are defined as outliers.) An updated linear fit is determined from the remaining measurements and the slope of this fit is forced to one. Measurement error is thus defined as the difference between measured particle positions and the linear fit at each traverse position shown in Figure 31. Outliers are included in this final calculation.

Figure 32 provides an example of the range of depth error measurements determined in this experiment. This histogram shows the individual depth error measurements from the middle depth configuration where the magnification is 0.5. In the following analysis, a distinction is made between measures of accuracy and precision. Accuracy is quantified by the mean of the depth error just defined, while precision is quantified by the standard deviation, σ, in measured depth error. Histogram plots for all other configurations are similar and not displayed here for brevity.

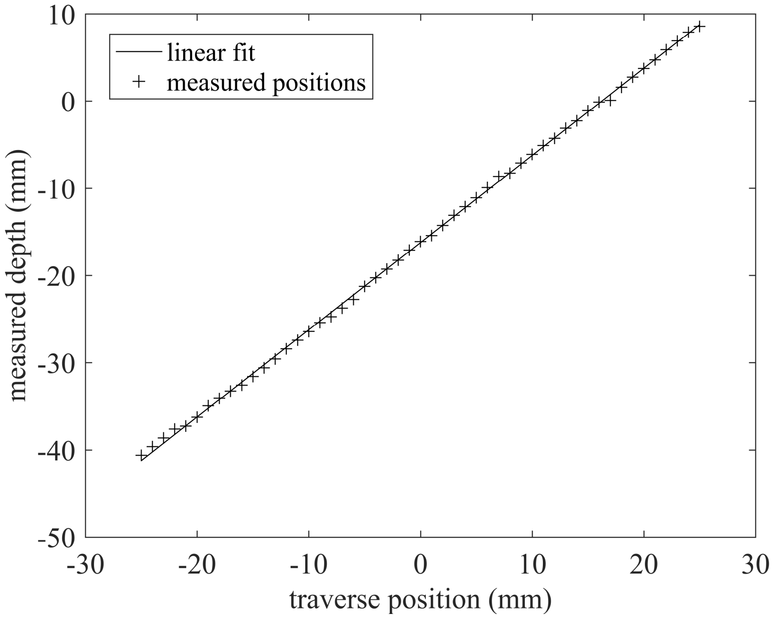

Figure 31. Depth error determination for the middle depth configuration with a magnification of 0.5.

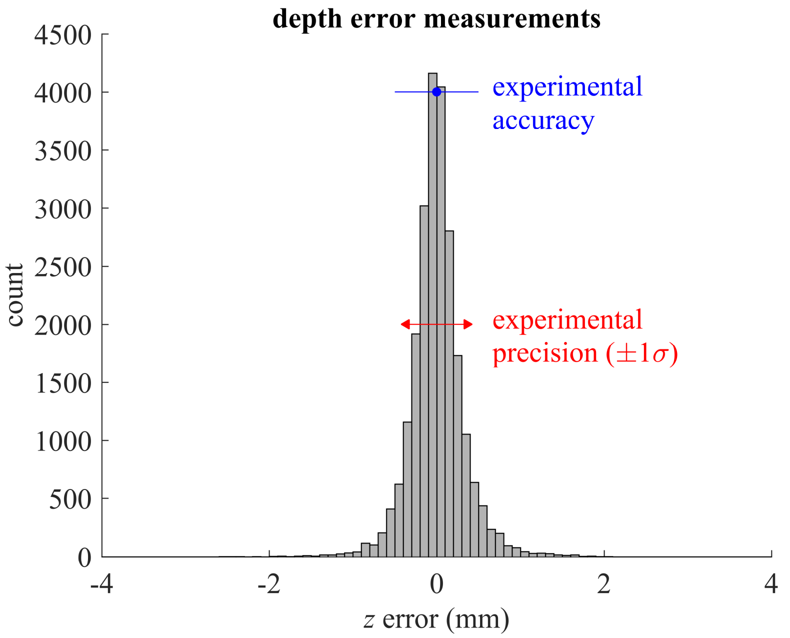

Figure 32. Histogram of depth error measurements for the middle depth configuration with a magnification of 0.5.

i. Confirmation of theoretical depth resolution

All conditions were analyzed as discussed above. Measured depth precision is summarized in Table 2. Here, the standard deviation of the measured error, σ, is taken from all measurements which fall within the calibrated regions. Where necessary, data from the near, middle, and far configurations are combined to quantify the overall measurement precision for each magnification. Comparison of the overall measured precision in the two right-most columns in Table 2 with the theoretical Δz in the left column indicates that the theory roughly corresponds to ±4σ. This is likely the first experimental confirmation that measured particle depth precision using a single plenoptic camera is bound by Equation (10). Therefore, when designing new plenoptic measurements, Equation (10) can provide a reasonable pre-test estimate of measurement precision.

In addition, the results in Table 2 also indicate that the uncertainty predicted by Equation (10) may be overly conservative for many applications. Assuming normally distributed errors, the ±4σ range predicted by Equation (10) corresponds to a 99.994% confidence bound. If, for example, one is instead interested in predicting the 95% confidence bound (~ ±2σ), Equation (10) should be multiplied by 0.5. Other confidence bounds can be similarly determined.

Table 2. Comparison of theoretical and measured depth precision.

	theory	measured precision	
M	Δz (mm), Equation (10)	±1σ (mm)	±4σ (mm)
0.25	10.7	2.68	10.7
0.35	5.4	1.16	4.6
0.5	2.6	0.88	3.5
0.75	1.2	0.58	2.3

Digital in-line holography (DIH) is a related single camera, 3D particle diagnostic [9]. Similar to the current results, the theoretical prediction of DIH uncertainty based on the depth of field of a refocused particle image tends to significantly exceed measurements of uncertainty when quantified by the standard deviation of errors [72]. In DIH it is also well known that the exact scaling between theory and experiment is a function of the image processing routines [76]. Although 3D particle measurements using plenoptic cameras has yet to be explored to the extent of DIH, it seems likely that the details of the data processing methodologies would affect the scaling between the measured uncertainty and the theory observed here.

ii. Effect of particle position

The previous section demonstrates that the overall depth uncertainty scales with Equation (10). It is also interesting to investigate the local uncertainty as a function of z depth, particularly as it relates to measurements both within and outside of $z_N \leq z \leq z_F$. That is the goal of this subsection. Figure 33 (left) displays the average depth displacement error as a function of z location for each tested configuration. This plot includes only data within the depth included in the volumetric calibration, which is within 25 mm of the center of each configuration. The data displayed here was calculated by discretizing the volume in the z direction and averaging the depth errors for displacements within each of these discretized regions. 99% confidence bounds are shown by the vertical bars and the relatively small confidence intervals indicate the statistical significance of this large data set. Examination of the errors in Figure 33 do not show a significant trend in accuracy as a function of particle depth suggesting that volumetric calibration has reduced the depth error bias seen in previous work [23].

A normalization of this data is displayed in Figure 33 (right) where average depth error is normalized by the pitch of a microlens in object space, Δx, and z location is normalized by z_N for

$z < 0$ and z_F for $z > 0$. From this figure it is evident that errors generally lie within a range of $1.5\cdot\Delta x$, similar to previous work [78]. Furthermore, it is interesting to note that relatively good accuracy is obtained outside of $z_N \leq z \leq z_F$. This can likely be attributed to the use of Volumetric Dewarping of the measurement domain, such that accurate results can be obtained outside of $z_N \leq z \leq z_F$ even though the ability to create tightly focused images is degraded.

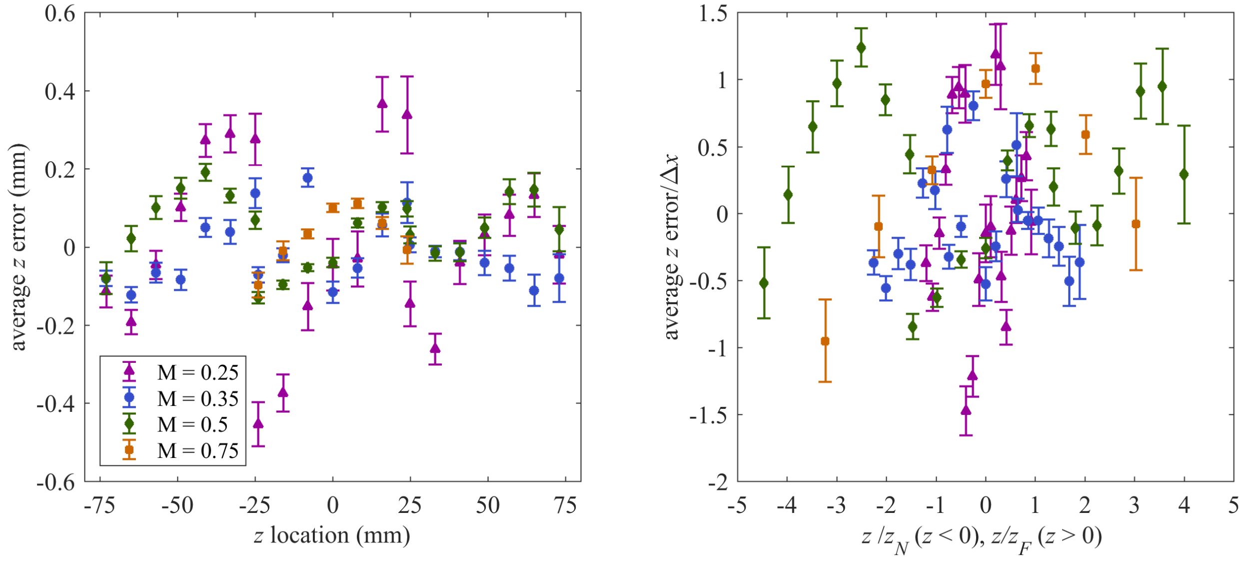

Figure 33. Average depth error for each magnification as a function of particle depth, *z*, in physical coordinates (left) and normalized (right).

Likewise, Figure 34 (left) displays the standard deviation of depth displacement error as a function of z location for each configuration. Error bars again show 99% confidence bounds. Results show a clear trend of decreasing standard deviation (increased precision) with increasing magnification as is generally expected and predicted by Equation (10). This trend largely collapses in Figure 34 (right) where measured σ is normalized by Δz, again confirming the validity of Equation (10). Within $z_N \leq z \leq z_F$ the averaged measured standard deviation is roughly $0.125\cdot\Delta z$, in agreement with the discussion of Table 2. Also, within this range there is no clear trend as a function of magnification or particle depth.

Outside of $z_N \leq z \leq z_F$ the normalized standard deviation tends to increase, indicating that Equation (13) provides a reasonable estimate of the depth range over which measurements are most precise. In contrast to the average error in Figure 34, Volumetric Dewarping does not remove this effect. This is likely because a dewarping procedure does not generally affect the local sharpness of particle images, which is the main driver of measurement precision. On the other hand, the decreased precision is somewhat gradual outside of $z_N \leq z \leq z_F$. This indicates that measurement uncertainty may be acceptable for some applications over depth ranges larger than those given by Equation (13). Therefore, the quantitative results shown in Figure 34 will provide useful guidance for design of new plenoptic measurements. Finally, it should again be noted that results are also likely to depend on the details of the image processing routines.

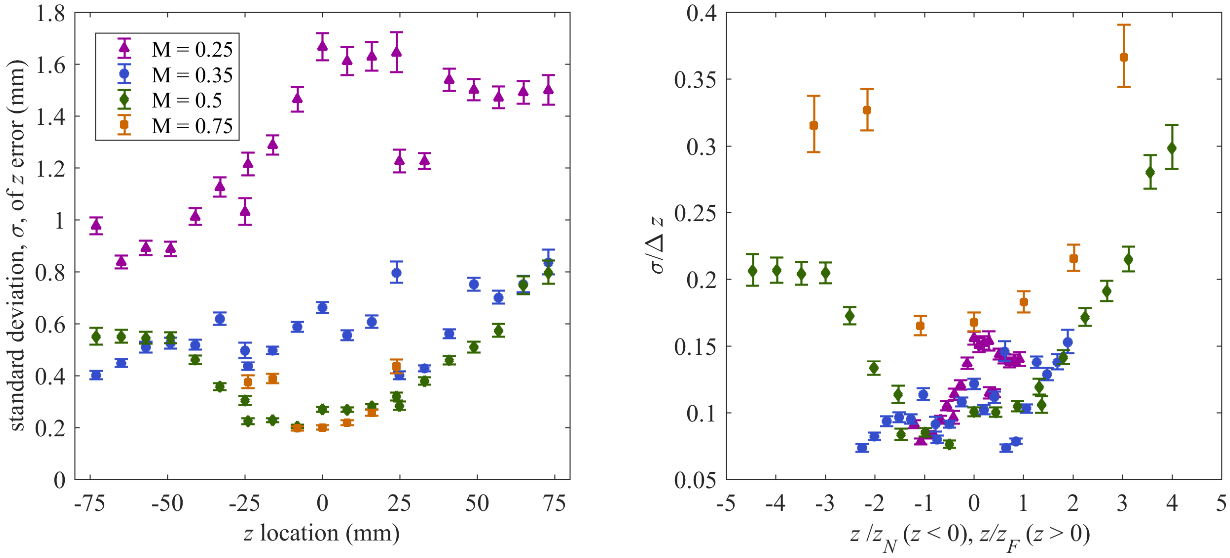

Figure 34. Standard deviation of depth error for each magnification as a function of particle depth, *z*, in physical coordinates (left) and normalized (right).

iii. In-plane error

Though measurement of in-plane error is not the primary goal of this work, a general analysis of in-plane uncertainty can be made based on the fact that physical translation of the particle field was aligned with the depth direction, therefore, error can be defined as any measured movement in the x or y directions. Similar to the analysis of the z error, in-plane error is found by fitting the x and y positions to a constant value with respect to traverse position. Error is thus defined as the measured deviation from this constant.

Error in the x and y directions were analyzed, and as expected results were found to be similar in both directions. For brevity, only the x error is considered here. As is the case for the z error in Figure 33, the average error in the x direction was found to be roughly constant as a function of position and less than $\sim \pm 0.05 \cdot \Delta x$. This is thought to be a reflection of the accuracy of the global dewarping procedures.

Again, the standard deviation in x positional error is considered as a metric of precision. Figure 35 (left) shows the measured results as a function of measured particle depth, z, while Figure 35 (right) shows normalized quantities. Comparison of the magnitude of the results in Figure 35 (left) with the analogous plot of z error in Figure 34 (left) indicates that the standard deviation in the in-plane error is roughly an order of magnitude less than in the z direction. Figure 35 (right) also indicates that the measured standard deviation is a fraction of the size of a single refocused pixel, Δx. This is likely a reflection of the use of sub-pixel region centroid approximation common to image processing routines. Finally, Figure 35 (right) does indicate reduced precision outside of $z_N \leq z \leq z_F$ and some collapse of the data by normalization. Although, it should be reiterated that this study was not focused on the quantification of these in-plane errors, and additional experimentation is warranted to check the consistency of the observed trends. In particular, the relative particle size as a function of magnification and the effect of particle size on the particle location method was not examined.

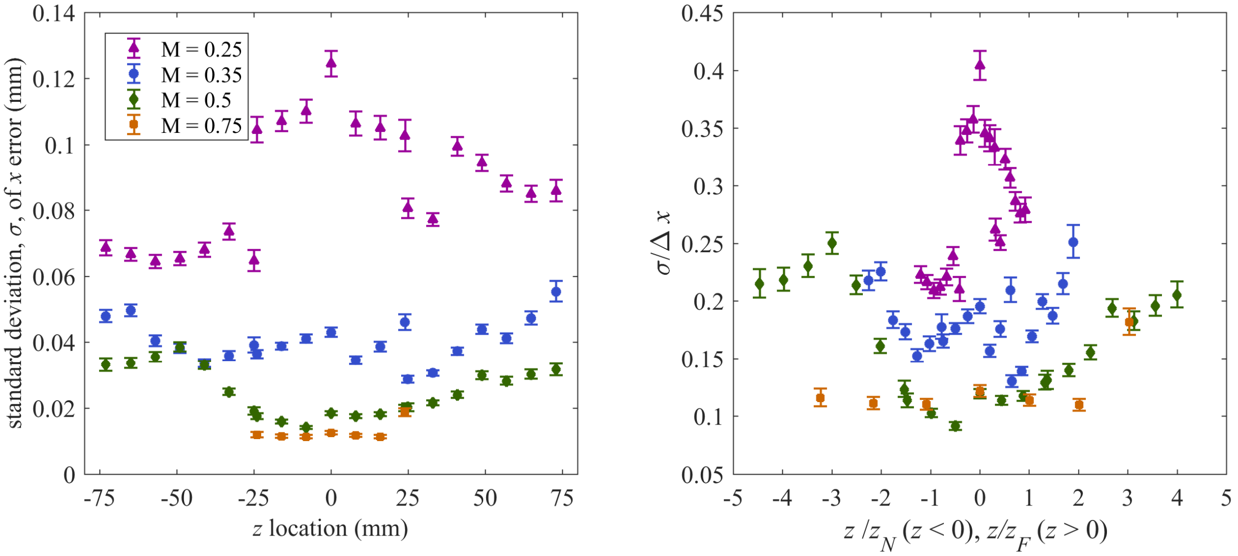

Figure 35. Standard deviation of in-plane error for each magnification as a function of particle depth, *z*, in physical coordinates (left) and normalized (right).

E. Limitations

The large computational requirement of the processing is one of the most significant drawbacks of refocusing based particle location measurements. Due to the large volume of data collected in this study, a computer cluster was used to process the results within a reasonable timeframe. Processing of a single image using one core of this cluster required approximately 5 hours. In a typical run, 256 cores were used simultaneously to enable processing of approximately 1200 images in one day.

An additional limitation of particle measurement from refocused images is encountered in the case of particles that overlap in the in-plane dimensions. An example is shown in Figure 36 where a similar configuration to the one in the previous sections is shown, except that randomly oriented nails are used to provide large aspect ratio particles to simulate explosive fragments. The left column of Figure 36 shows the minimum intensity map and maximum Tenengrad map created from a focal stack. Colored ovals identify two pairs of nails that cannot be separated using the refocusing based method described in this chapter. The right column of Figure 36 shows three perspective views calculated from this same raw image, shifted left (top), center (center) and right (bottom). Examination of the same two pairs of nails shows that in the center perspective, neither pair of nails can be separated; however, in the view shifted to the left the pair circled in red can be separated and in the view shift right the pair circled in green can be separated. This view dependent separation as well as the reduced computational time required for calculation of perspective views and possible uncertainty improvements motivates the development of the perspective shift based algorithm described in Chapter V.

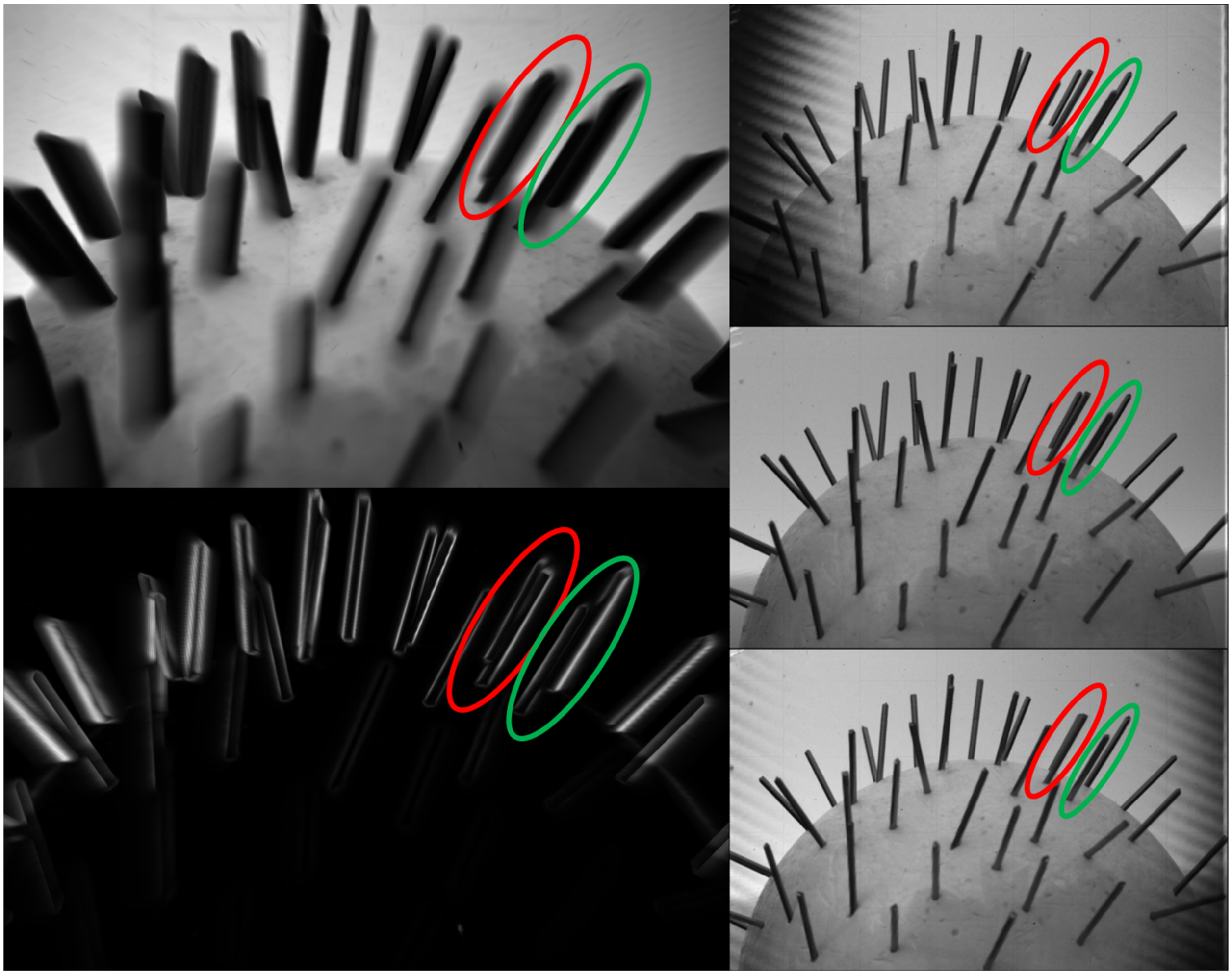

Figure 36. Occlusion measurement limitation example. Focal stack minimum intensity map (top left) and maximum Tenengrad (bottom left) compared to perspective views (right). Ovals indicate corresponding pairs in each image.

F. Summary

These experimental results show overall agreement with the theoretical values of uncertainty in 3D particle localization using a single plenoptic camera. For all optical configurations considered here, the mean displacement error in both the depth, z, and in-plane, x,y, directions is shown to roughly correspond with the size of a refocused pixel over the entire measurement volume considered. Likewise, the predicted precision in the z direction, based on the depth of field of a numerically refocused image, is shown to roughly correspond with ± 4 times the standard deviation of measured depth error, again, confirming theory. Finally, precision is shown to be optimum within the overall predicted DOF of the perspective shifted images with gradual degradation outside of this range.

V. Depth from perspective

Here, a particle localization algorithm is proposed which utilizes the perspective shift capability of the plenoptic camera to overcome the limitations of the previous refocusing based method [79]. In the sections that follow, a description of the development of the perspective shift based algorithm is given encompassing the entire data processing routine from raw image to measurement of 3D particle positions and in-plane size and shape. A discussion of the computational efficiency of the method is also included and compared to the previous refocusing based implementation.

A. Algorithm development

The algorithm developed in this work uses the discrepancy in 2D particle centroids between perspective views to determine 3D particle positions by exploiting the relationship defined by the DLFC volumetric mapping function. The large number of views available in plenoptic imaging provides redundancy and allows erroneous measurements to be identified and removed which reduces uncertainty. A general outline of the method is shown in Figure 37 and is summarized in the following subsections. Throughout this section the processing of an example image from the static particle field data set considered in Chapters IV and VI is presented as a visual tool to provide context for the algorithmic description. A detailed description of the implementation of the method and use of the relevant MATLAB code can be found in Appendix C: Perspective shift algorithm code reference for readers interested in use, modification, or further development of this method.

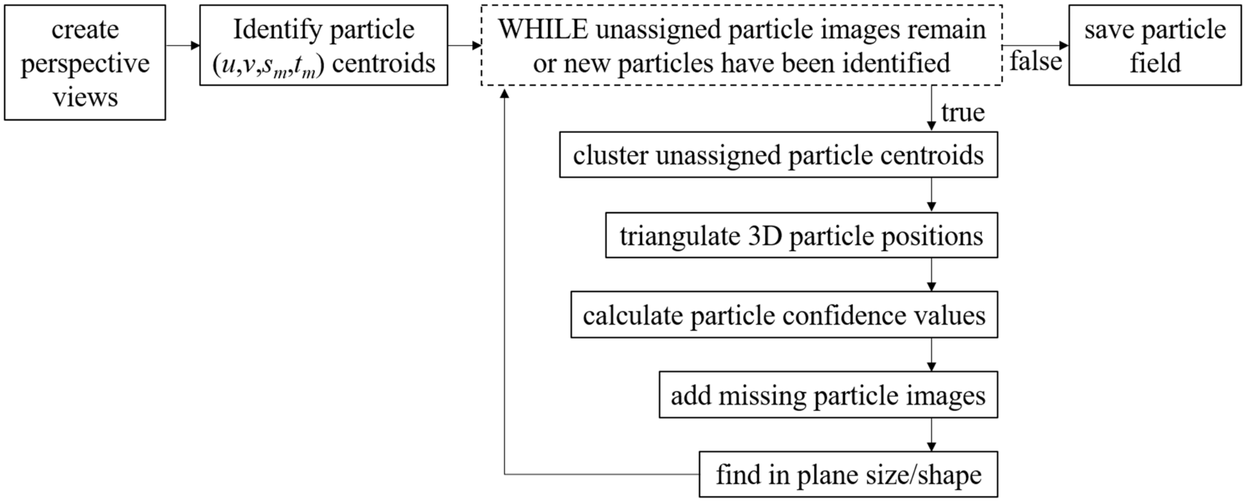

Figure 37. Flow chart outlining the depth from perspective method to determine 3D particle position and in-plane size and shape from a raw plenoptic image.

i. *Identification of particle centroids within each perspective view*

As shown in Figure 38, the first step is the creation of all available perspective views from the single, instantaneous raw plenoptic image. Here, perspective views are generated using the Light Field Imaging Toolkit (LFIT) [34], and each view is assigned a (u,v) position corresponding to angular position within the main lens aperture. Note, in Figure 38, three example perspective images are shown from the 97 total perspective images generated with the current camera and processing algorithm.

Next, in each perspective view, particle locations are determined by segmentation. This work utilizes typical MATLAB region finding tools which define particles (or fragments) as connected regions of pixels with intensities below dynamically determined maximum intensity thresholds. Before segmentation, an averaging filter is applied to each perspective view using a user specified window size. The original perspective view is subtracted from this image to improve the separation between the background and foreground objects in images with non-uniform illumination. Then MATLAB's 'graythresh' is used to determine an appropriate threshold for the image segmentation. This function applies Otsu's method to determine an appropriate threshold by assuming there are two classes of pixels in the image and minimizing the intra-class variation in pixel intensity in the two sets [80]. This threshold is applied to produce a binarized image which is then segmented using MATLAB's 'regionprops' to find regions of connected pixels. User inputs allow selection of acceptable particle size and shape parameters and intensity threshold window size; therefore, results can be improved in applications where some particle size and shape characteristics are known. Note that the literature contains a wide range of alternative image segmentation tools. These could likely provide additional benefits and tuning parameters when required for other applications.

Red circles shown in Figure 38 give examples of the identified particle regions for each perspective view. In this image, pinheads are used to represent particles. Within each perspective view, the centroids of these segmented regions are assigned (s,t) spatial coordinates. This results in a list of measured (u,v,s_m,t_m) light field coordinates depicting all measured particle centroids. In the following subsections 3D particle location is determined using these centroid coordinates. Identified particle regions are used for in-plane size and shape determination and to filter potential shape outliers from centroid clusters. Note, in Figure 38, some particles are not identified in every view due to in-plane proximity with other particles. Still, as shown in the subsequent discussion, the 3D locations of these particles can nevertheless be determined due to the large number of available views.

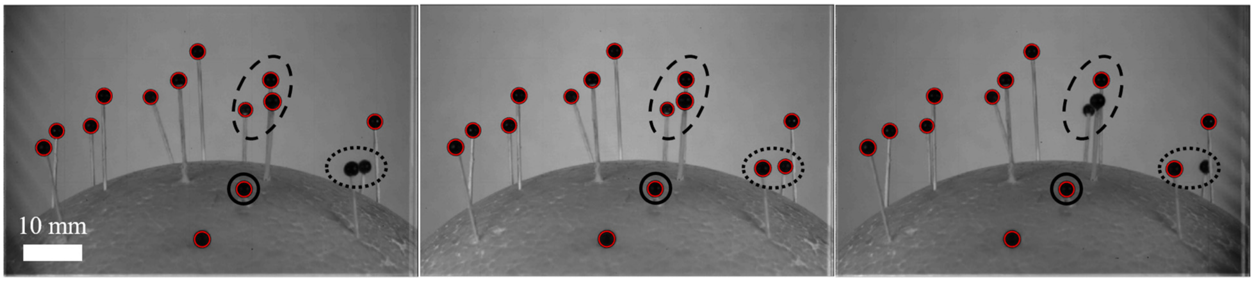

Figure 38. Perspective views of a static particle field demonstrating a horizontal shift in perspective. Red circles indicate identified particles in each view. Black ovals indicate particle of interest.

ii. Clustering of corresponding particle centroids from each view

As seen in Figure 38, an individual particle is assigned different (u,v,s_m,t_m) centroids from each perspective view. Next it is necessary to match each of the corresponding particle centroids which belong to the same physical particle. Conceptually, this is similar to particle tracking, except that the views are spatially not temporally correlated. It is also similar to the correspondence problem in stereo photogrammetry, except that many views are used. This means that all views are equally correspondent to all other views and any sequential method of matching particle centroids between views is susceptible to bias resulting from the order in which views are matched. To avoid this bias, all particle centroids from all views are examined simultaneously using a variation of a k-means clustering technique in combination with depth plane projections. To simplify the discussion, this technique is first shown schematically in Figure 39 where a simulated example using two point particles (color coded blue and orange) is given.

Starting on the right side of Figure 39, an orange particle is located at an optical depth beyond the nominal focal plane. Light rays from this orange particle (shown by solid lines) propagate to the aperture of the main lens where they are focused at a plane in front of the microlens. When these rays reach the microlens plane, they spread back out and are imaged as a cluster of discrete (s_m,t_m) locations as shown by the orange dots in the center image in the bottom row of Figure 39. Similarly, the blue particle, located before the nominal focal plane, is imaged as a cluster of discrete (s_m,t_m) locations as shown by the blue dots in the center image in the bottom row of Figure 39. For scientific applications such as here, grayscale image sensors are typically used to maximize pixel resolution, and the color information shown in Figure 39 cannot be differentiated. Consequently, with no further information these two discretized realizations of out-of-focus particle images are difficult to separate and quantify as two distinct particles.

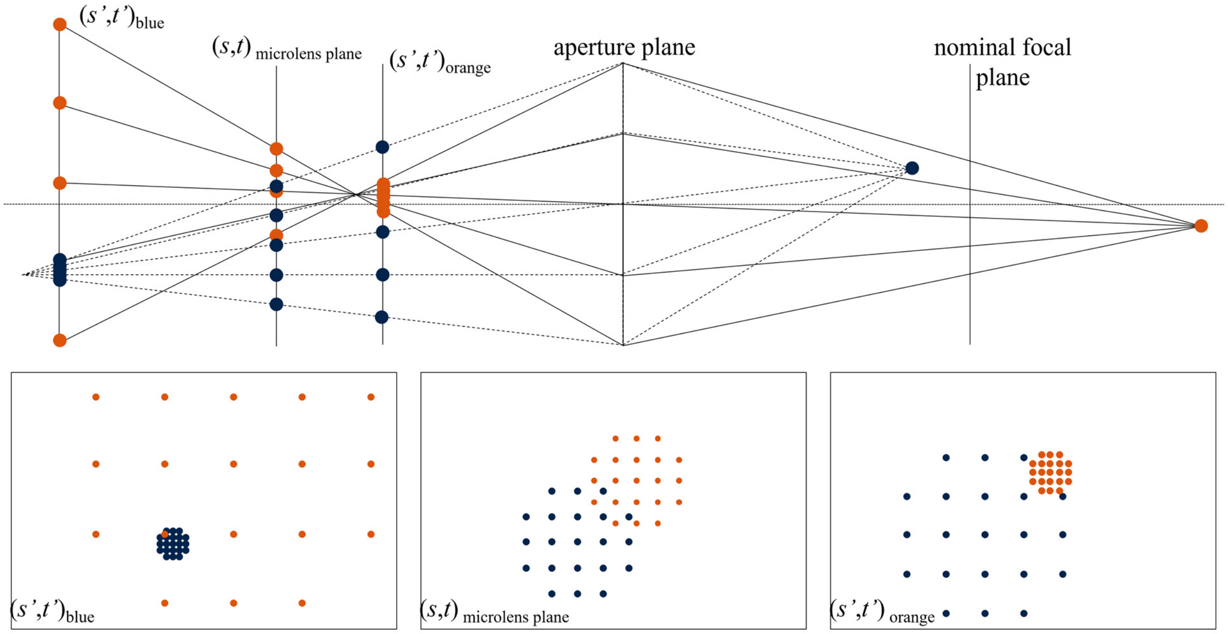

Figure 39. Schematic depiction of necessity and functionality of shifted plane projection clustering.

Fortunately, the plenoptic architecture also quantifies the angular (u,v) coordinates for each of the light rays in Figure 39. As shown in [14], with both the spatial (s_m,t_m) and angular (u,v) information, any ray can be numerically propagated to an alternative image plane at a distance α times the nominal image distance. At that plane, the refocused spatial coordinates (s'_m,t'_m) are

$$s'_m = u + \left(s_m - u\right)\alpha \text{ and } t'_m = v + \left(t_m - v\right)\alpha \, . \tag{14}$$

For example, when the rays in Figure 39 are projected to the $(s',t')_{\text{blue}}$ plane, which is close to the image depth of the blue particle, the rays belonging to that particle form a tight cluster that can be more easily identified. A similar effect occurs at the $(s',t')_{\text{orange}}$ plane for the other particle. Therefore, the method proposed here combines numerical refocusing via Equation (14) with spatial k-means clustering to identify matching particle centroids which form tight clusters at projected image planes near their focus location. As clusters of particle centroids are identified, they are removed from consideration, improving the likelihood of successful clustering of remaining data. (Note, although the α at which a cluster is identified provides an estimate of particle depth, this is not used as a depth measurement due to the sparsity of projection planes and because the necessary volumetric calibration is not applied to calculate the projection.)

At a given image depth (fixed α), the k-means algorithm minimizes the average squared distance between points in the same cluster for a given number of clusters, k [49]. In this application k is the maximum number of particle centroids identified in a single perspective view. This clustering is executed at a range of planes throughout the volume of interest by projecting the particle centroids to different image planes using Equation (14). At each plane, k-means clustering is executed. The size of each cluster is calculated as the maximum distance between the particle (s_m,t_m) positions assigned to that cluster. Any cluster with a size below a predetermined size threshold is accepted as a correct particle cluster and removed from consideration at following planes. The size threshold, T, is the expected maximum size that a correct particle cluster could be if the physical location of the particle is closer in depth to the current plane than any of the other considered planes defined by,

$$T = 1.2\left[\frac{F}{f_n}\frac{\alpha_{1/2}}{\alpha_s - \alpha_{1/2}}\right], \qquad (15)$$

where, F is the focal length of the main lens, f_n is the f-number of the main lens, $\alpha_{1/2}$ is the value of α halfway between the current and neighboring shifted planes, and α_s is the value of α at the current shifted plane. This expected value is multiplied by 1.2 to allow for experimental error.

To reduce the impact of the order in which the depth planes are examined in the clustering procedure, planes are examined from smallest to largest size threshold. At smaller thresholds it is less likely that centroids from an incorrect particle would be included in a cluster. Since centroids are removed from consideration as they are sorted into a tight cluster, this results in a smaller number of particles at the planes with larger size requirements. Note that the difference in required cluster size at each plane is a result of the non-linear scaling between physical coordinates and light field depth planes (α). The planes are evenly spaced in physical space (z) since it is assumed that the particles are randomly distributed throughout the volume. Therefore, this equalizes the largest possible distance of a particle at any location in the volume from a cluster plane.

To assess the effect of the order in which the planes are examined we compared the results of the algorithm using the order described above to the results of the reverse order. The trial used (an image from which is used as the example throughout this section) was selected as it provides an example of overlapping particles and therefore a worst case scenario in terms of clustering success. In this case, 1.6 percent of the measured particles showed some deviation in final measured position as a result of reversing the order in which the planes were examined for clustering. All other particles were measured to be in the same location, indicating that the same centroids were used to calculate the particle position. One reason that this impact is small is the redundancy in available data (due to the large number of views) which allows the removal of any measurements which may be erroneous based on the known configuration of the views. Of those particle measurements that varied, the average difference in depth was 0.024 mm, with in-plane differences approximately an order of magnitude smaller. This suggests that at the particle densities of interest in this application the order of the clustering planes results in a very small difference in the final results, however, it may have a more significant impact at higher particle densities. One important parameter with expected relevance in application to data sets with increased density is the number of cluster planes at which the k-means algorithm is executed. The smaller the number of clustering planes, the larger the size thresholds. This results in more particles per plane and increased probability of cluster overlap even at the optimal plane for a given particle.

An example of this projection and clustering process applied to the experimental image shown in Figure 38 is given in Figure 40. This shows the compilation of measured particle centroid locations from all perspective views projected to two different planes. Of particular interest are the particles in the circled regions. First, consider the projections in the dashed oval. From Figure 38 it is evident that there are three particles in this region. At the projection plane shown on the left of Figure 40, only two clusters are created due to the proximity of the particle centroids, however by projecting these positions to the plane shown on the right, the three particles are separated enough to allow correct clustering. At this plane, the particle images shown in blue form a tight cluster and are identified as a particle; the other two particles are identified at planes not shown here. Other examples of tight clusters created by the projection process are shown in the solid and dotted ovals where the particle centroids form a tight cluster at one plane but not the other. In the case of the solid circle, a single particle is incorrectly identified as two large clusters (neither of which meet the size threshold, T, to be defined as a particle) in the plane shown on the left, but correctly identified in the plane shown on the right.

In some cases of overlapping particles, it is possible that no single view contains all overlapped particles. In this case, it is impossible to identify these overlapping particles because the value of k is smaller than the true number of particles. To rectify this, if the above process is completed and a large number of unassigned particle centroids remain, the possible number of particles input into the k-means algorithm is incrementally increased and the process is repeated with the remaining unassigned particle centroids. This allows the necessary trial and error in the determination of the appropriate value of k to be automated within the algorithm. At the particle densities examined here, this trial and error was required in 15.7% of raw images, though this percentage can vary with the number of required views for a valid particle measurement. The average increase in computational time in cases where the trial and error is required is 0.10 seconds per raw image.

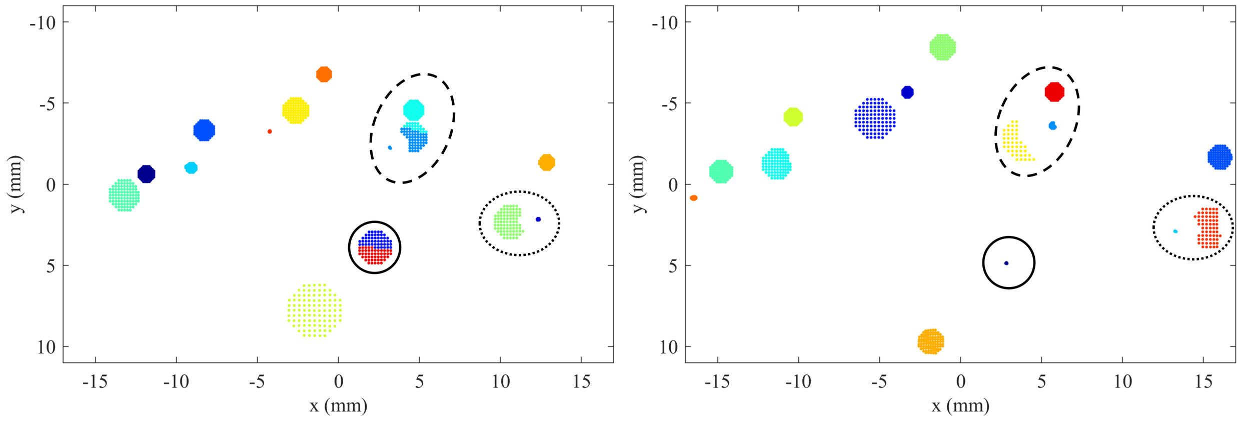

Figure 40. Example of particle centroid clustering executed at two different projection depth planes, color indicates centroids assigned to the same cluster. Ovals indicate particles of interest corresponding to those shown in Figure 38.

For each physical particle in the measurement volume, the end results of this clustering portion of the algorithm is a list of all measured (u,v,s_m,t_m) particle centroids combined from all perspective views. Given the possibility of erroneous cluster assignment, the 3D location procedure allows the rejection of any measurements which may have been inappropriately assigned.

iii. 3D particle location

The calculation of the 3D object space location of a particle is determined using the relationship defined by the Direct Light Field Calibration (DLFC), as described in Chapter III. A schematic depiction of the 3D triangulation process is given in Figure 41. For a given particle, first the (x,y,z) position that minimizes the DLFC polynomial for the (u,v,s_m,t_m) coordinates is determined using a MATLAB nonlinear solver. Next, the DLFC relationship is used directly to define calculated light field coordinates, (u,v,s_c,t_c), which correspond to the (x,y,z) position. The measured and calculated light field coordinates are compared and any measurements that show large discrepancies are rejected as outliers. Then the process is repeated by calculating a new (x,y,z) position using the remaining (u,v,s_m,t_m) until no large discrepancies are found. This allows removal of a (typically small) number of erroneous measurements while still allowing a valid measurement of the particle.

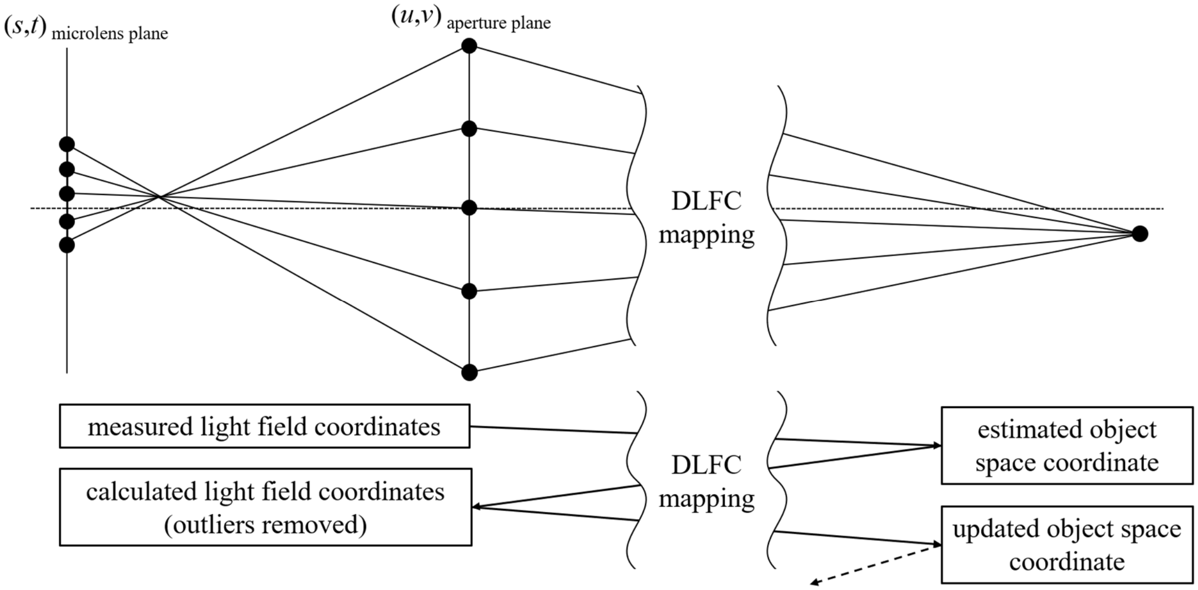

Figure 41. Schematic depiction of 3D particle location process. Translation between light field and object space coordinates is repeated via DLFC until no outliers remain.

iv. Confidence determination and particle centroid addition

At this point, an attempt is made to find particle centroids that may belong to an identified particle but have not been assigned to that particle due to overlap, the influence of other nearby particles, or unsuccessful clustering. First, a confidence value for each identified particle is defined as,

$$C = \frac{n_v / n_p}{d / z_n}, \tag{16}$$

where, n_v is the number of particle centroids identified for the cluster, n_p is the maximum number of possible centroids (defined by the number of available perspective views), d is the average difference in the measured and calculated (s,t) positions for all matching (u,v) for the particle, and z_n is the depth position of the particle relative to the nominal focal plane normalized by the volume depth. The numerator, n_v/n_p, goes to one when a cluster contains particle centroids located from every perspective view. The denominator, d/z_n, is a measure of the in-plane uncertainty of the particle centroids, which is normalized by the optical depth from the nominal focal plane. This normalization accounts for the expected increase in uncertainty away from the nominal focal plane. Therefore, Equation (16) produces high confidence values for particles that are measured in many perspective views and that have small in-plane uncertainty relative to the nominal focal depth.

Next, for every cluster where $n_v < n_p$, starting with the cluster with highest C, the remaining unassigned particle centroids are examined and any centroid which falls within an allowable positional range is added to the cluster. The 3D position is then recalculated using the more complete set of particle centroids. If unassigned centroids still remain, the entire process is repeated starting by clustering only the remaining particle centroids.

v. In-plane size and shape determination

The last step in the algorithm is the determination of the final in-plane size and shape of the particle. This is accomplished by first creating a refocused image centered at the (x,y,z) position where the particle centroid is measured. The combination of information from refocused and perspective shifted images to determine depth has been implemented in literature, notably Tao et al. in an attempt to exploit the strengths and avoid the weaknesses of each [35]. Here, refocusing is used to avoid the more prominent noise resulting from the small effective aperture of a perspective view which significantly affects the consistency of image thresholding. However, this only requires refocusing of a small portion of the light field, thus having a negligible effect on the computational efficiency gain made in the use of perspective views for particle triangulation.

The in-plane size of the refocused image that is constructed is based on the size of the largest bounding box in which the particle was identified in a perspective view and is enlarged by a small factor to ensure the background is present on all sides. To improve the quality of the refocused image, only the views in which the particle was successfully located are used to create the refocused image in an effort to avoid the inclusion of any views with problematic image artifacts (such as vignetting) or in which the particle was occluded. This refocused image is then segmented with built in MATLAB functions which again use Otsu's method [80] as in the identification of particles in perspective views except that no filtering is applied because the refocused image is only a small region, so consistent illumination is assumed.

The procedures described in subsections ii-v above are repeated until either no unassigned particles remain, or no more particles can be successfully identified. Finally, Figure 42 shows the results when the entire process outlined in this section is applied to the example presented in Figure 38 and Figure 40. Again, particles of interest are circled as in Figure 38 and Figure 40. Note that even the partially occluded particles, shown here in maroon and teal, have been successfully located at independent depths.

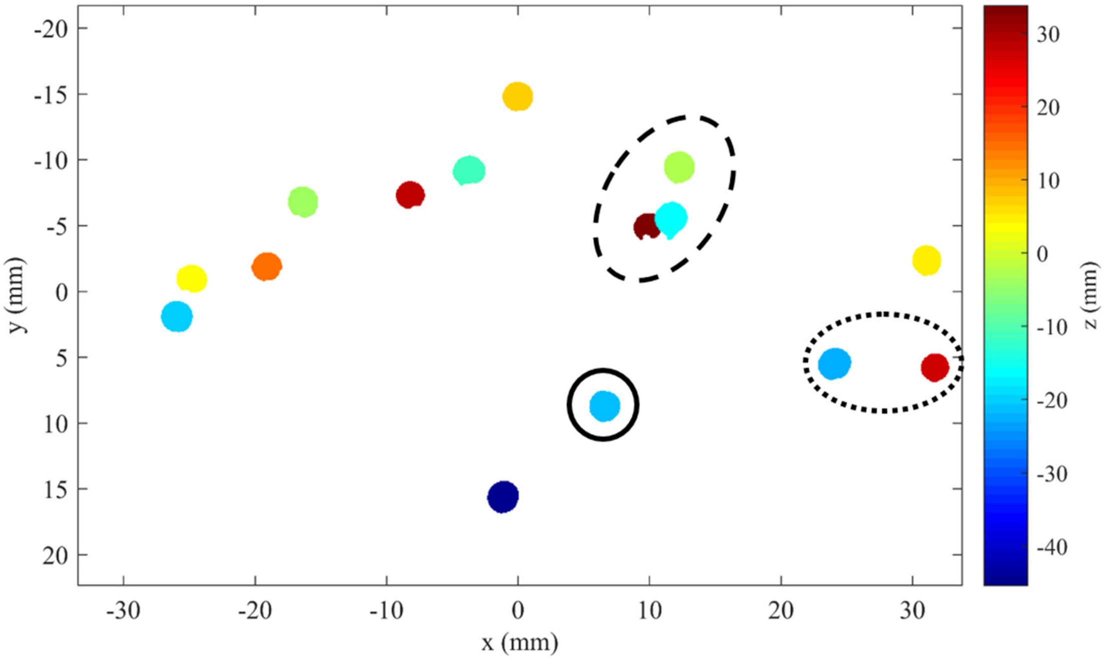

Figure 42. Depth map depicting the final measured positions of the particle shown in Figure 38.

B. Computational efficiency

This section compares the computational resources required by the perspective shift and the previous refocusing based methods. Computational times reported here consider a MATLAB implementation parallelized on a 12-core desktop with dual Intel Xeon E5-2600 v4 processors and 144 GB of RAM to provide a point of comparison for the reader. The large scale processing results reported throughout this dissertation were conducted using a computer cluster at Sandia National Laboratories to allow processing in a reasonable timeframe. Both methods initially require a preprocessing step in which the raw hexagonal microlens grid is interpolated onto a rectilinear grid, which takes about 1 minute. The calculation of a focal stack of the required density and subsequent determination of particle centroid locations using the refocusing method takes about 1 hour for a single image. In comparison, the calculation of perspective views and execution of the particle location algorithm described in this chapter takes approximately 10 seconds – a decrease of about 2 orders of magnitude. For the 30000 image data set from which the example image was taken and which is analyzed in the following chapter, processing using refocusing would take 3.24 years of computational hours, while processing using perspective shift would take only about 24 days of computational hours if processed on the desktop described above. It should be noted that for more complicated or dense particle fields the processing time requirements of each method increases.

The use of perspective views rather than a focal stack also reduces the memory requirements. The refocusing method requires memory storage of a large focal stack (approximately 2 GB of RAM required for each raw image in the current example). In contrast, storage of the perspective views requires only about 0.2 GB. This also significantly affects the computational resources required to reasonably process plenoptic data. Considering the improved uncertainties that can also be obtained using this method, these computational reductions are particularly significant.

C. Summary

Here an algorithm is developed to determine 3D particle position and in-plane particle size and shape from perspective shifted images. This is done by creating a range of perspective views from a raw plenoptic image and determining particle centroids in each of these views. These particle centroids are then projected to a variety of virtual image sensor planes and sorted using a *k*-means clustering routine. Finally, the 3D position of the particle is determined by minimizing the relationship defined by the Direct Light Field Calibration polynomial and the position of all particle centroids from all perspective views. This method allows the removal of individual low-quality measurements from the quantities used to determine final 3D particle positions.

VI. Uncertainty characterization experiments

This chapter is focused on uncertainty characterization of the perspective shift method developed in Chapter V by the analysis of well controlled experiments in a manner analogous to that of the refocusing implementation developed in Chapter IV [79]. Section A of the current chapter discusses the results of applying the perspective shift algorithm to the previously analyzed static particle field data set to assess perspective shifting in comparison to refocusing directly. Additional experimental configurations described in Section B expand the particle type parameters based on the motivating applications of this dissertation. Section C of the current chapter examines the expanded parameter data set. This includes parameters of interest identified as relevant in the initial refocusing based study and focuses on assessment of parameters relevant to the motivating explosion analysis application. Results indicate that measurement error of the perspective shift based method is reduced compared to the previous refocusing based method.

A. Depth from focus vs. depth from perspective

In this section, the refocusing and perspective shift methods are compared side by side through analysis of the same data set to allow direct quantitative comparison of the achievable uncertainty and measurement limitations of each method. Results consider the 12 static particle field experimental configurations described in detail in Chapter IV Section C.

i. Accuracy

Accuracy is considered in Figure 43, which displays the average depth displacement error as a function of z location measured using the perspective shift based method on the left and the results of the previous refocusing based method on the right. Vertical error bars represent 99%

confidence bounds. The perspective shift results show not only error decreased by approximately a factor of 2 but also smaller confidence bounds as compared to the refocusing results, demonstrating measurements that are more consistent. Over a range of 50 mm, depth displacement error is within 0.1 mm, or approximately 0.2% relative error. This can be compared to the refocusing implementation in which errors of approximately 0.4% were measured. As in the refocusing implementation, there is no clear trend in accuracy as a function of depth indicating that the applied DLFC effectively removes depth bias caused by lens distortion and alignment errors.

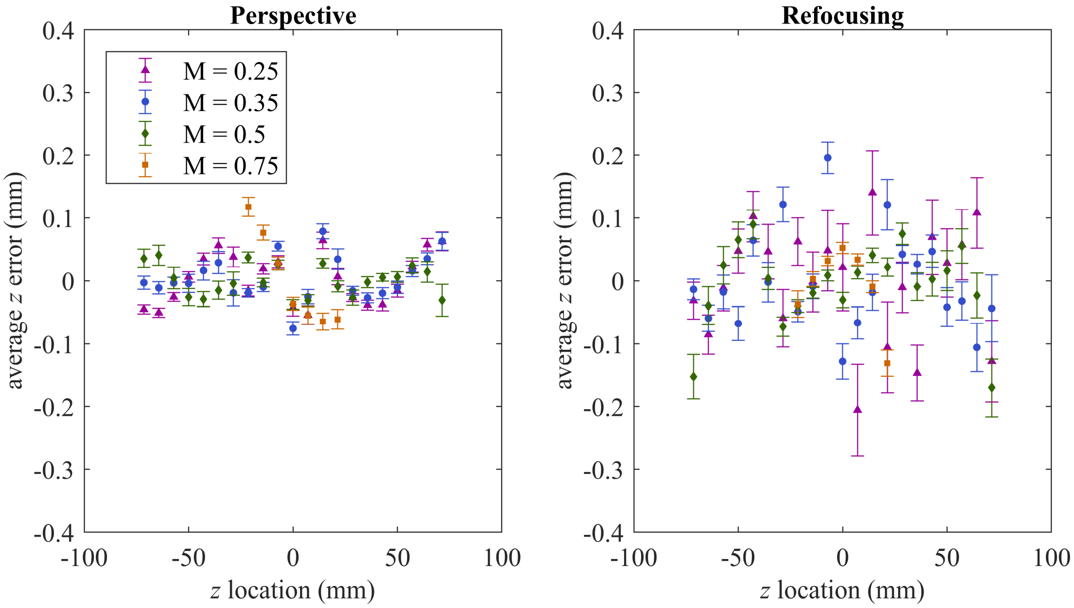

Figure 43. Average depth error as a function of particle depth, *z*, using perspective shift (left) and refocusing (right) based depth measurement.

ii. Precision

Precision is examined in Figure 44 in similar plots with standard deviation of depth error as a function of depth. The perspective shift results show generally improved precision and smaller error bars as compared to the refocusing results. Over a range of 50 mm, the standard deviation of depth displacement error is within 0.4 mm. Again, this is significantly improved compared to the refocusing case where values up to 1.8 mm were measured. In the refocusing based implementation, an improvement in precision was also evident with increasing magnification, a trend not seen in the perspective shift results. This difference is likely a result of differences in the metrics used to determine particle depth. In refocusing, depth is determined using sharpness metrics; therefore, the precision of the measurements is likely related to the number of edge pixels of each particle. Since a fixed particle size is examined in all cases, at larger magnifications each particle has more edge pixels, possibly contributing to the increased precision of these measurements. In the perspective shift based implementation, depth is determined based on the location of the particle centroids, the accuracy of which is not strongly affected by particle size except at extremes. Additionally, the perspective shift method allows removal of low quality portions of measurements by rejection of imprecise particle centroids from individual perspective views. In refocusing, these measurements are integrated into the final position measurement and may negatively affect precision.

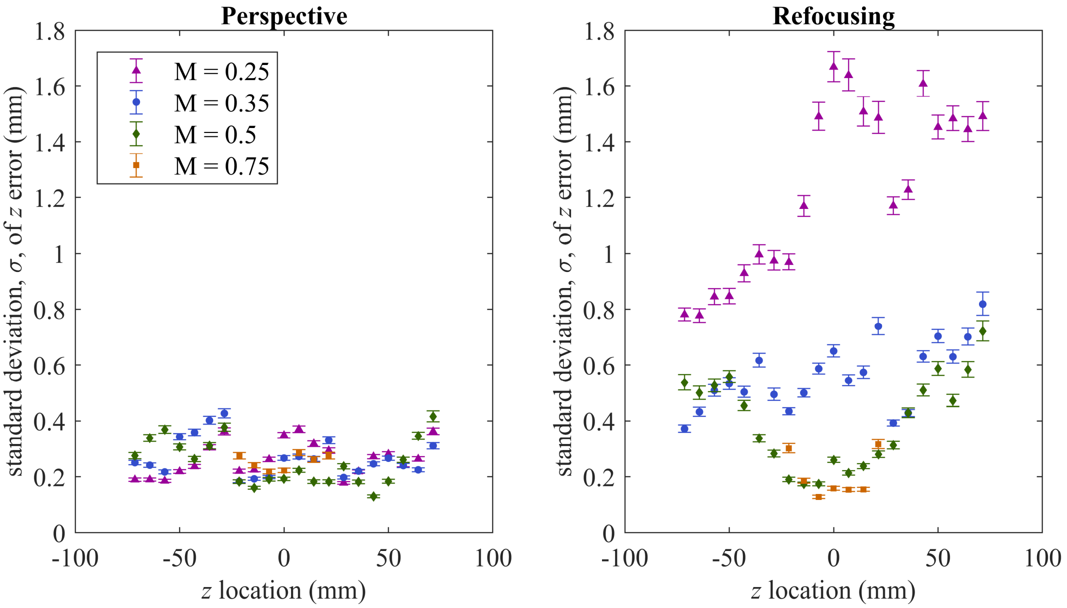

Figure 44. Standard deviation of depth error as a function of particle depth, z, using perspective shift (left) and refocusing (right) based depth measurement.

The natural follow on question remaining in this discussion is the consideration of what the precision limitation is a result of in the perspective shift based measurements and specifically why the resulting precision is similar at all magnifications within the experimental limitations. It is possible that in this experiment the limit is tied to the volumetric calibration procedure. Some parameters relevant to this discussion are given in Table 3.

In this experiment the calibrations for each magnification were conducted with dot cards of varied size so that the diameter of the dots in image space were similar in each to allow consistency in processing. Specifically, the dot diameters were selected to be equivalent to a consistent number of pixels in the resulting processed images and similarly a consistent number of microlenses behind each dot. Each dot diameter was approximately 8 times the microlens pitch in object space as shown in the table. It then follows that the similarity of the precision measurements at all magnifications may be a result of the physical precision of the calibration configuration. Given the high precision of the translation stage used, any significant errors are suspected to be a result of the precision of the printed dot cards and the stability of the dot card mounting system. Though it appears likely that the dot size scaling discussed here is related to the precision limitation, further work including examination of varied dot sizes relative to the microlens size is necessary to draw a definitive conclusion.

Table 3. Volumetric calibration parameters.

Magnification	Microlens pitch in object space (mm)	Calibration dot diameter (mm)	Number of microlenses per dot
0.25	0.308	2.5	8.12
0.35	0.220	1.75	7.95
0.5	0.154	1.25	8.12
0.75	0.103	0.83	8.06

It appears that these effects were not evident in the refocusing based analysis because the errors resulting from the sharpness and intensity based processing method were more significant than the physical calibration errors. These errors related to the image processing method may have been particularly impactful because the refocusing based implementation used Volumetric Dewarping Calibration rather than Direct Light Field Calibration so both the calibration dot measurements and the particle measurements were made using maximum edge sharpness and minimum intensity metrics.

iii. *Depth range*

The improvements provided by the perspective shift algorithm as compared to the refocusing algorithm are further demonstrated by the depth range over which measurements can be obtained. In the previous refocusing based method, much of the data at the largest magnification (0.75) could not be processed. This was attributed to the small depth of field, which did not allow objects to be brought into sufficient focus for valid sharpness measurements. In contrast, the perspective shift method requires only the centroid of a particle to be located. Therefore, data can be processed at depths significantly outside the depth of field.

Figure 45 and Figure 46 provide an example of this difference in processing method. Figure 45 shows sharpness maps from refocused images of dot cards which were located at the nominal focal plane and well outside the depth of field, $z = 0$ mm and $z = 75$ mm, respectively. At the nominal focal plane, the dot edges are clearly identified by sharpness as demonstrated by the narrow region of high magnitude sharpness values. Conversely, far outside the depth of field, much smaller sharpness values, about 3 orders of magnitude smaller, are observed over a large spatial region. This sharpness map does not allow sufficient measurements of dot locations. Figure 46 shows two perspective views demonstrating a vertical shift in perspective of this same dot card located far outside the depth of field. The dots, of course, remain out of focus in these images, however, the in-plane locations can still be determined, as can be seen qualitatively by comparing the positions of the dots relative to the black lines in each image.

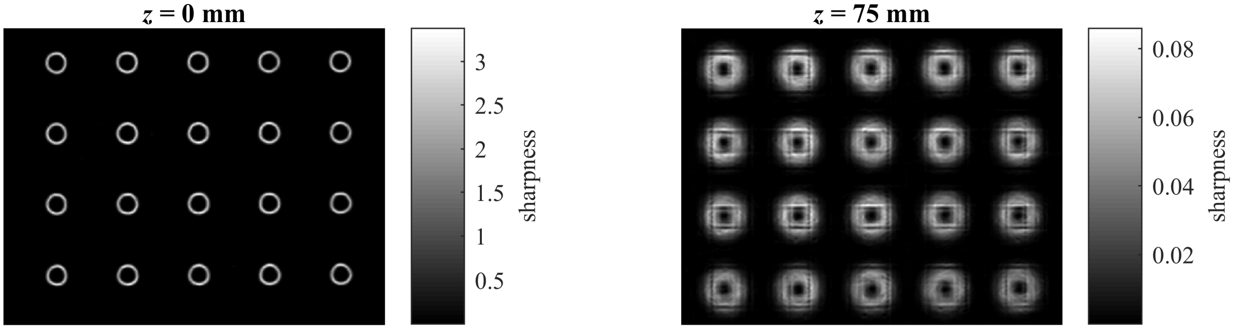

Figure 45. Sharpness maps of refocused dot card images located at 0 mm (left) and 75 mm (right) from the nominal focal plane.

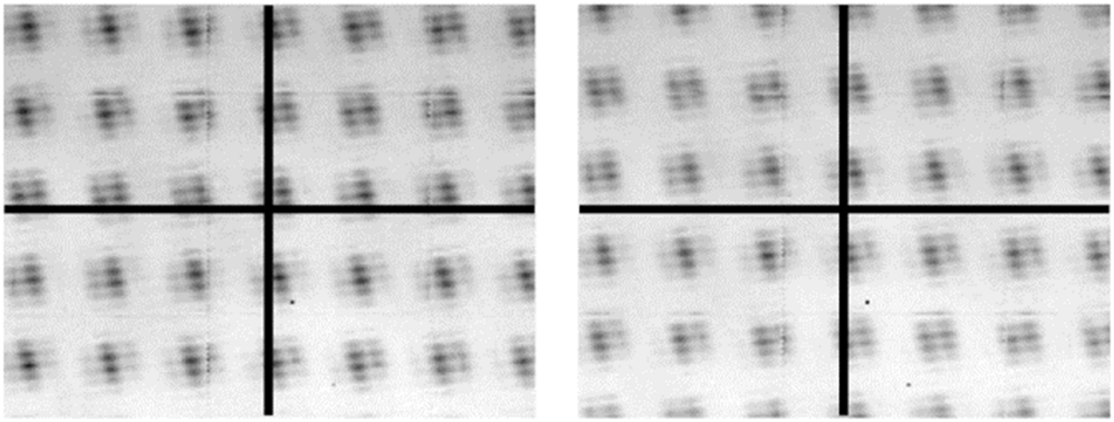

Figure 46. Perspective shifted images of a dot card image located as 75 mm from the nominal focal plane demonstrating a vertical shift in perspective. Black lines overlaid in the same location on each for reference.

The results of this difference are illustrated in Figure 47 where standard deviation of depth error is plotted as a function of depth for the static particle field data set at the largest magnification. Comparison of the results of the two methods in the near focal plane region (|z| near zero) demonstrates similar results. At the extremes, some degradation is evident in the perspective shift results, particularly at the depths farthest from the camera where only a relatively small number of particles could be located. Still, at these depths, the refocusing method failed to measure any particles. Therefore, the improved ability of the perspective method to quantify particles at extreme optical depths is another advantage of the use of perspective shifted images for particle measurements.

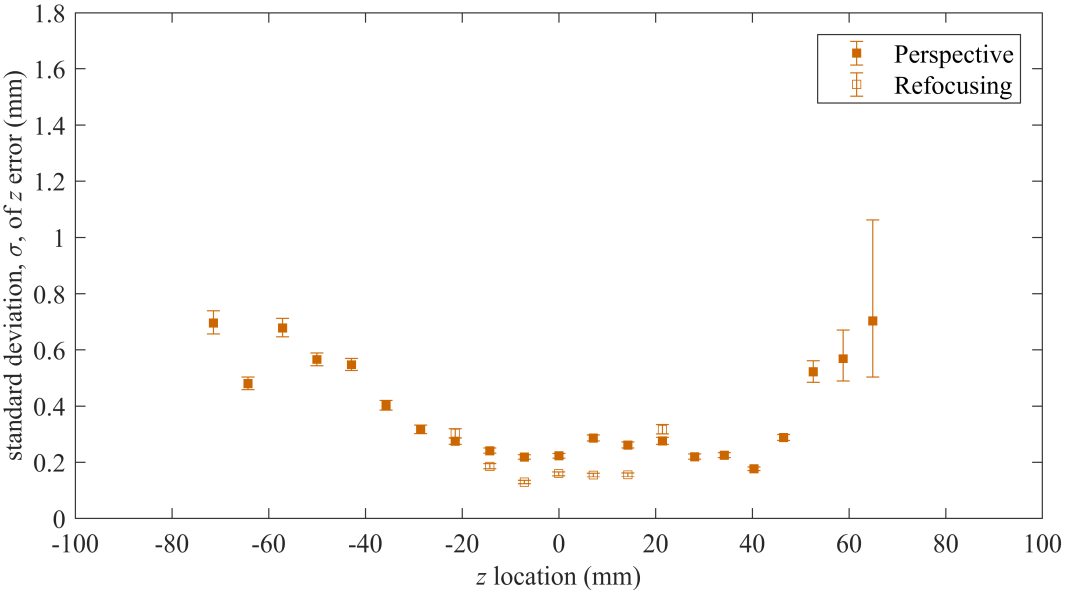

Figure 47. Standard deviation of depth error as a function of particle depth, *z*, for a magnification of 0.75 using both perspective shift and refocusing.

The plot in Figure 47 only includes the precision measurements for the largest magnification case. In the data set examined here this is the only case where the precision degradation is evident in the perspective shift results, as alluded to in previous sections, it is suspected that this is result of the difference in the DOF at each magnification. At all magnifications, data was collected and calibrated over the same depth range of $z = \pm 75$ mm, which corresponds to a significantly different range of DOF in each case.

Table 4 provides the calculated near and far limits of the DOF for each magnification as well as the ratio of the data set edge to the DOF edge. Note that at the smallest magnification of 0.25 nearly the entire range of the data set was within the DOF while at the largest magnification data was collected at distances of approximately 10 times the limit of the DOF. Therefore, it follows that if data were collected at the smaller magnifications at equivalent extreme DOF locations, a similar degradation in precision would be present. In general, it appears that the depth range within which precise depth displacement measurements can be made is extended by the use of perspective shift based measurements as compared to refocusing based measurements, but still eventually limited at some distance relative to DOF. Based on the results from the large magnification case examined here, it appears that this degradation begins at approximately 5 to 6 times the DOF, though further investigation including examination of a continuous data set with a larger range of depths at varied magnification is warranted to verify this trend.

Table 4. Depth of field comparisons.

M	Near DOF (mm), Equation (13)	Far DOF (mm), Equation (13)	Near data set edge (near DOF)	Far data set edge (far DOF)
0.25	-61.0	79.4	1.2	0.9
0.35	-32.4	38.6	2.3	1.9
0.5	-16.4	18.2	4.6	4.1
0.75	-7.4	7.9	10.1	9.5

iv. Spatial dependency

Considering the known lens distortion present in plenoptic data, the dependency of depth error on in-plane distribution is of interest. Figure 48 shows a plot of the in-plane locations of the measured particles from the middle depth static particle field configuration at a nominal magnification of -0.25 color coded by the measured depth error. Note that the arc shaped distribution is a result of the pin head placement in the static particle field experiment. This plot indicates that there is a slight tendency for increased error with increasing radial distance from the center of the image. This suggests that the calibration polynomial may not completely remove the spatial distortion, however, errors of all magnitudes do appear throughout all regions the image.

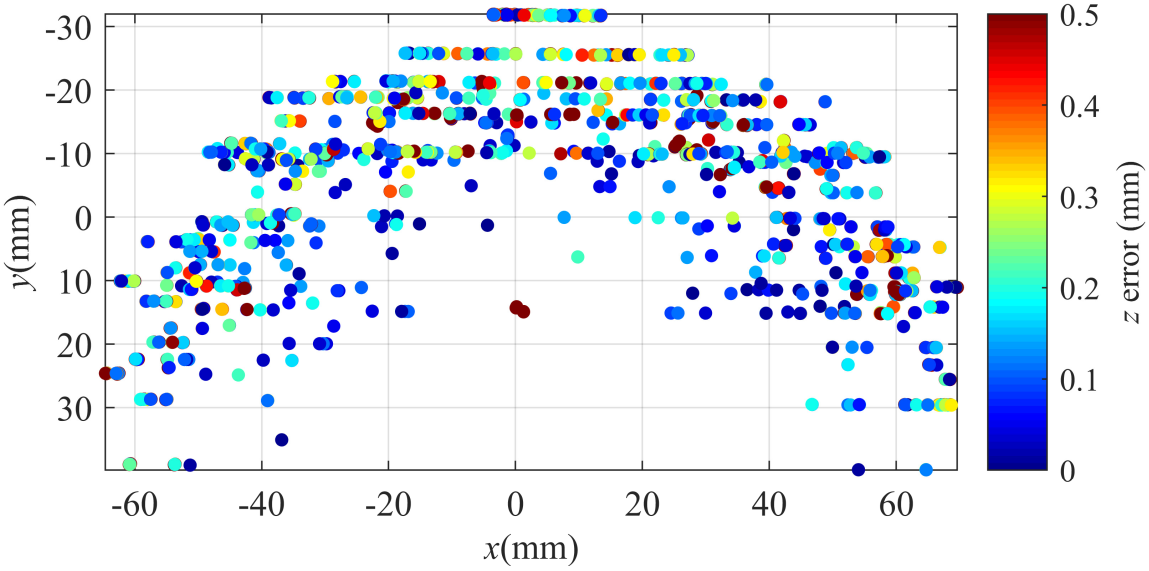

Figure 48. In-plane distribution of depth error where color indicates the magnitude of depth error.

v. Confidence dependency

A final point of interest in analysis of this static particle field data set is consideration of the relationship between the confidence value determined in the perspective shift based algorithm for each particle and the corresponding depth error. This confidence metric is defined by Equation (16). Figure 49 displays depth error as a function of the calculated confidence values. This plot verifies that particles with larger confidence values are measured with improved accuracy. Further, these results demonstrate that the numerical values of the confidence metric are dependent on the magnification as the measurement in the smaller magnification configuration show larger confidence values. This suggests that a normalization based on volume size or resolution could be included to allow consistent confidence values for all configurations. However, it should be noted that the addition of this type of normalization would not have any effect on the use of these confidence values in the current algorithmic implementation as only confidence values within a single image are compared.

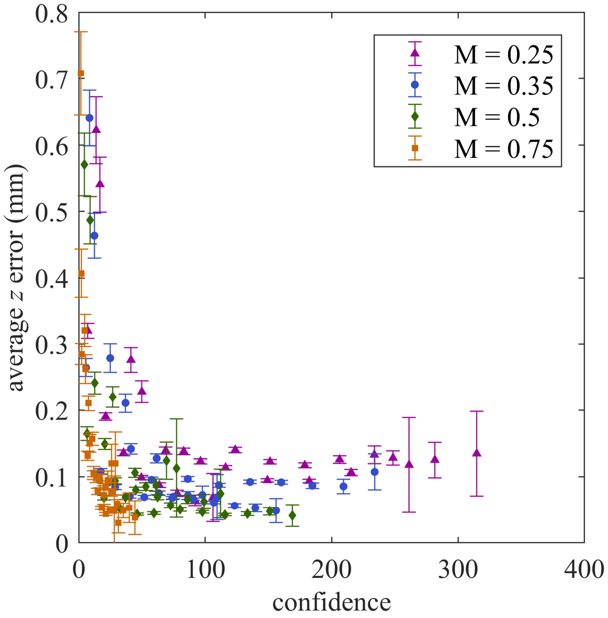

Figure 49. Average depth error as a function of measured confidence value.

B. Expanded parameter experimental configuration

The adaptations made in the new data set are described in this section. Images are collected at depths within 100 mm of the nominal focal plane in 2 mm increments. Given the nominal magnification in this configuration of approximately 0.3, the near and far limits of the DOF are approximately -41 mm and 50 mm, respectively. Therefore, images over this depth range of ±100 mm provide data well outside the DOF of the system in a single continuous experimental configuration. This large depth range was specifically chosen to allow examination of uncertainty outside the depth of field as the previous study and theory suggest degradation at extreme depths. The particle simulants and arrangements examined are described in the following subsections where the resulting measurements are studied.

To examine the depth measurement uncertainty of the perspective shift method for application to large aspect ratio fragments, pin gages of varied known diameter were used as particle simulants. An example perspective view of one of these images is shown in Figure 50. NIST traceable class ZZ pin gages with diameter accuracy of +0.0000", -0.0002" (+0 µm, -5µm) were used, the diameters labeled in the figure have been converted to metric units for consistency. The perspective shift algorithm was used to determine locations of these pin gages in each of the 101 images captured over the 200 mm depth range. To allow direct comparison to the measurement of spherical particles, a similar data set was collected using a row of pin heads of two different types (each with some variation in size) in a similar configuration as shown in Figure 51. The specific diameters of each pin head were measured with calipers with an accuracy of ±5µm and are labeled in the figure.

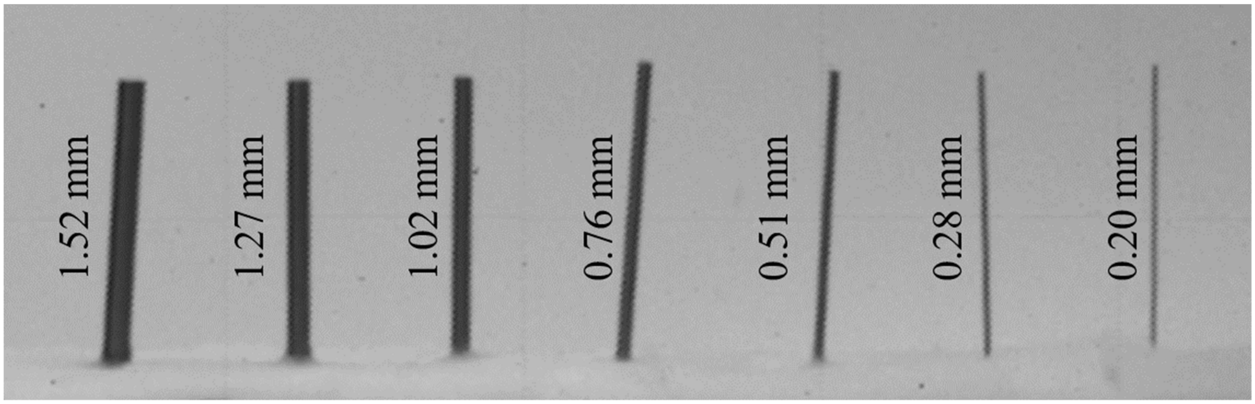

Figure 50. Example perspective view from pin gage data set and corresponding known diameters.

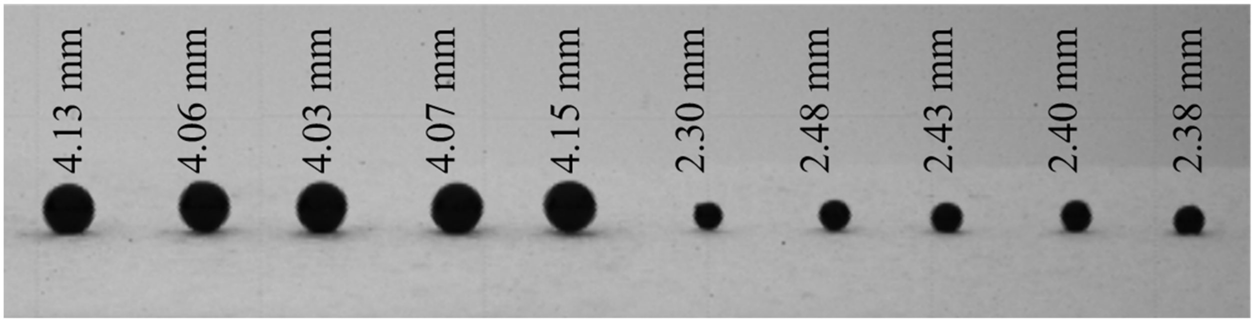

Figure 51. Example perspective view from pin head data set and corresponding known diameters.

C. Expanded parameter analysis

This section examines how the measurement uncertainty of the perspective shift method is affected by variations in the size and shape of the particles or fragments of interest. The uncertainty of the in-plane size measurements of the particles is also assessed including discussion of the effects of image segmentation on these measurements. Particular emphasis is placed on understanding the effects of the image processing selection criteria on these uncertainties.

i. Particle elongation

To assess the effects of particle elongation on accuracy and precision a similar analysis to that in Section A is conducted. This analysis uses measurements of the pin gage data set as large aspect ratio elongated particles, and of the pin head data set as spherical particles, shown in Figure 50 and Figure 51, respectively.

Figure 52 shows the average depth displacement error as a function of depth for both sets of particles as a metric of accuracy, vertical error bars indicate 99% confidence bounds on these measurements. The spherical particles show generally consistent accuracy as a function of depth while the large aspect ratio fragments show a decrease in accuracy at increasing distance from the focal plane ($z = 0$ mm) and larger confidence interval for all depths. A similar trend is observed in Figure 53 where the standard deviation of depth displacement error is shown as a function of depth, examined here as a metric of precision. The spherical particles show consistent precision over the entire 200 mm range examined while the large aspect ratio particles show worse precision at the more extreme depths. The confidence intervals for the large aspect ratio particles are again larger than those for the spherical particles, a trend that increases with depth.

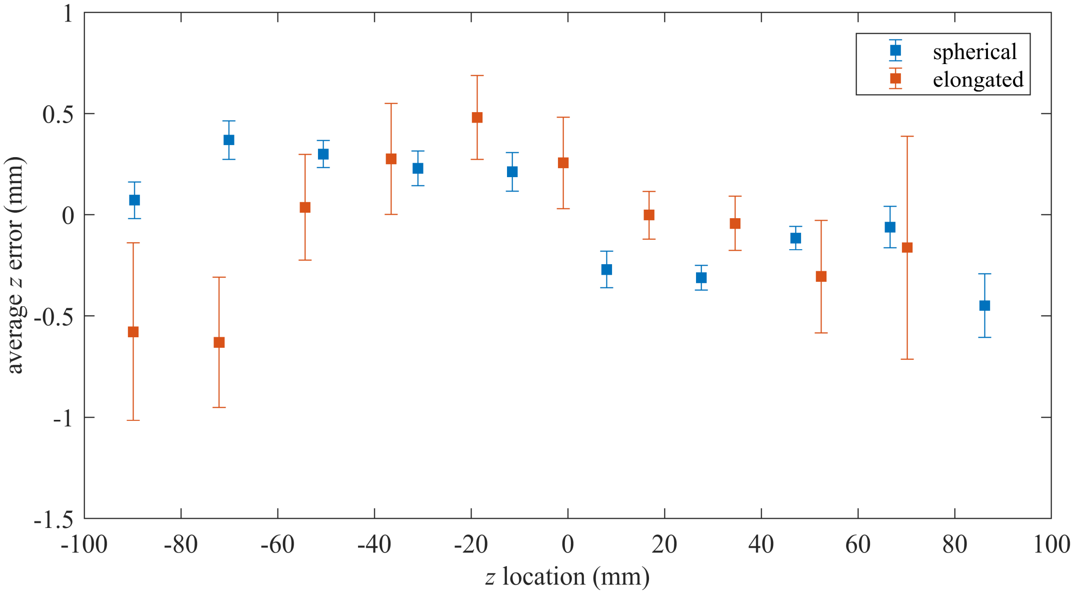

Figure 52. Average depth displacement error as a function of depth as a metric of accuracy.

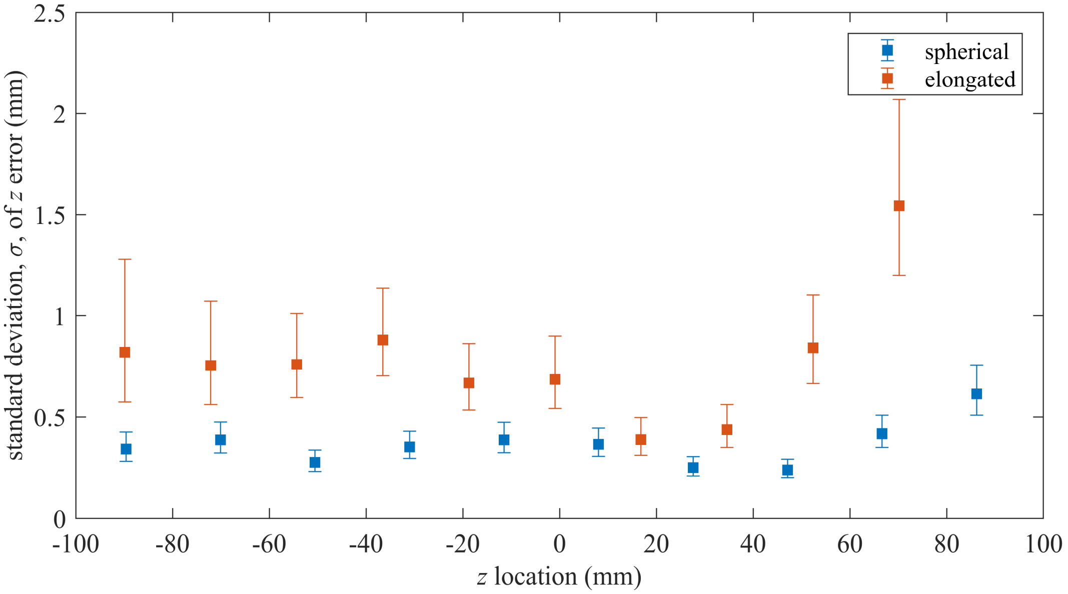

Figure 53. Standard deviation depth displacement error as a function of depth as a metric of precision.

The source of these differences appears to be related to the in the in-plane aspect ratio and size of the two types of particles and how the region identified as the particle is affected by the image segmentation scheme. Specifically, in the case of the smaller pin gages where the diameter only spans a few microlenses (in the smallest case less than one microlens), slight differences in the pixels selected in each perspective view as part of the particle can have a dramatic impact on the measured centroid location of the particle. An example of these differences in centroid measurements is shown in Figure 54 which displays five relatively extreme perspective views from an example image of each type of particle. These images have been segmented based on an intensity thresholding scheme, yellow pixels indicate locations that have been identified as particles and red circles indicate the measured centroid locations of these yellow regions.

Several observations can be made from these examples. First, examination of the particle regions identified for the smaller pin gages shows that in some cases the image segmentation results in a single pin gage being identified as several smaller regions, none of which meet the user defined inputs for a valid particle measurement. This issue is more prevalent at larger distances from the focal plane where image blur is more prominent, resulting in less measurements at these depths and contributing to the increased uncertainty, specifically larger confidence intervals, in these regions. There are also cases where small portions of the end of a pin gage are identified as a separate region, resulting in a small region that does not meet the particle size and shape requirements and a large region that does meet the requirements but has an invalid centroid location because it does not represent the entire particle. A prominent example of this phenomena is present in the centroid location of the smallest pin gage in the $(u,v) = (4,0)$ case, however this occurs to some extent in all the pin gage diameters examined here. These errors are more pronounced in the large aspect ratio fragment measurements than the spherical particle measurements because of the larger size of the length dimension which allows a larger region of variation. The errors in centroid position propagate to the final measured 3D positions of the particles and again contribute to higher uncertainty and affect both the accuracy and precision of the depth measurements. These observations suggest that larger errors would be expected in measurement of the smaller diameters, however, in this small data set it is unclear whether this is the case because all of the measurements for a given diameter are of a single pin gage translated through the volume. A larger data set in which many measurements of each pin gage size are made could allow further investigation of this trend.

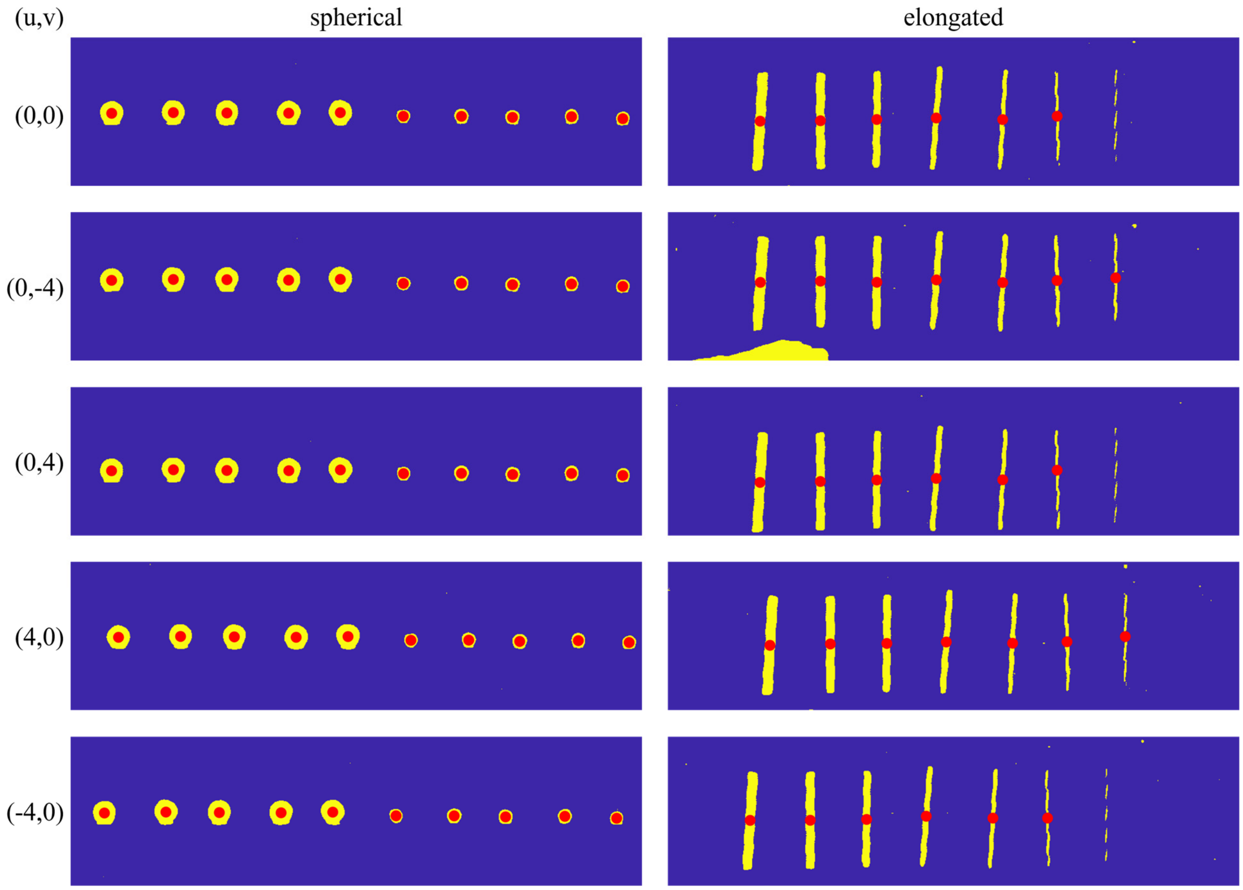

Figure 54. Thresholded perspective views and measured centroids for spherical and elongated (large aspect ratio) particles.

It should also be noted that the uncertainty for the spherical particles in this data set is larger than in the data set examined in Section A. The reason for this is likely linked to two differences in the volumetric calibration of this data set. First, in the current data set, a single calibration was executed over a depth range of 200 mm while in the previous study individual calibrations were executed in 50 mm segments due to experimental limitations of the translation stage. The use of a long continuous calibration may result in a polynomial mapping that cannot entirely encompass the lens distortion errors without further modification. Second, the calibration target used in the current experiment had dot diameters of 6.94 times the diameter of a microlens in object space, smaller than the 8 microlens diameter dots used in the previous study. This may also impact the uncertainty given the possible link between particle size and the uncertainty of centroid measurement. Further study including an in-depth examination of the effects of various calibration variables is warranted to make a definitive statement on the reason for the variation in uncertainty between the two experiments.

ii. Obscured objects

In the measurement of extended objects such as the fragment field analogs discussed here, a significant benefit of the use of perspective views is the ability to make measurements of partially occluded or overlapping objects. In the refocusing implementation discussed in Chapter IV, when an occlusion is encountered, a valid measurement cannot be made of either object because separate edges cannot be defined and the regions of minimum intensity for the objects merge into a single region. An example of this limitation is shown in Figure 36 where a field of nails used as large aspect ratio fragment simulants is imaged. In that figure it is demonstrated that by the use sharpness and minimum intensity metrics, the two image characteristics used to determine particle positions from refocused images, the two pairs of circled fragments cannot be separated. This is mitigated by the use of perspective shift based measurements. Due to the redundancy resulting from the large number of views collected, views in which problematic occlusions occur can be removed and the remaining views can be used to make measurements of both objects. The three perspective views in Figure 36, displayed again in Figure 55 for convenience, provide an example of the separation of occluded fragments. These three views demonstrate a horizontal shift in perspective. The two pairs of nails circled in red and green are of interest, note that the pair in red is separated in the left view (left) but overlapped in both other views and the pair in green is separated in the right view (right) and again overlapped in the other two views.

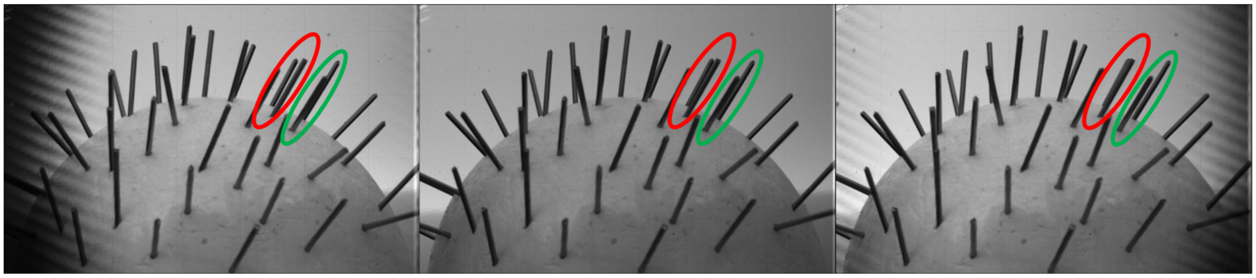

Figure 55. Perspective views providing an example of objects that are occluded in only some views.

For the measurement of each fragment only the views in which that fragment is not occluded are considered, allowing measurement of both fragments in both example pairs. The final measured positions are shown in Figure 56, demonstrating the capability of the algorithm to measure independent depths for both particles in each of these overlapping pairs. The measurement of these occluded particles provides a benefit over the existing refocusing based implementation. It should be noted that this view based separation is limited by the angular range contained within the physical main lens aperture, therefore, objects with a large degree of overlap cannot be successfully separated. This is evident in the example here given that some of the fragments on the left side of the image with a higher degree of overlap are not identified.

This limitation provides motivation for future exploration of alternative image segmentation schemes to allow measurements of more highly occluded particles. These schemes could include the use of image characteristics such as texture, orientation, or boundary lines in place of or in addition to intensity thresholding [81]. Additionally, more integrated use of both the refocusing and perspective shift methods of decoding raw plenoptic data could allow more detailed measurements of occluded particles. For example, consider the case of two large aspect ratio particles located at different depths and crossed at a 90 degree angle such that even a very extreme shift in perspective would not separate the two particles, but, the majority of each particle in visible in all views. In this case, if the sharpness in the region of the crossed particles was examined in a refocused image, the edges of each particle would have different sharpness magnitudes. These sharpness measurements could then be used to define the regions belonging to each particle. The ideal scheme would likely be a flexible algorithm which applied different segmentation methods based on individual particle characteristics to allow optimized use of all available raw data without introduction of prohibitive computational costs.

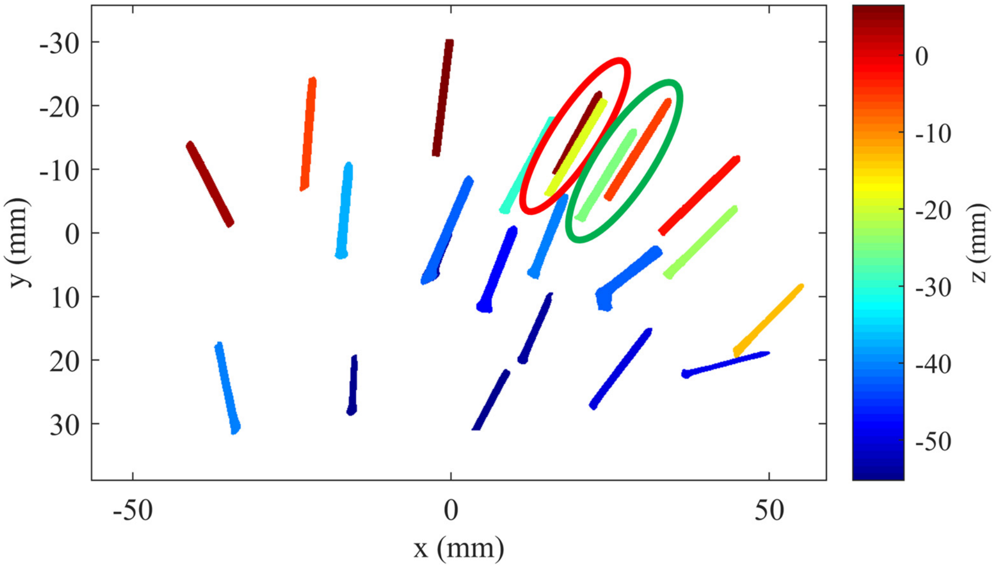

Figure 56. Measured positions of the fragments shown in the perspective views in Figure 55.

iii. *In-plane size*

The pin gage data set, in Figure 50, is examined here to assess the uncertainty of the in-plane size measurements due to the accuracy with which the diameters of the pin gages are known. Figure 57 shows a plot of the measured diameters of these pin gages as a function of the known diameters. A solid line $y = x$ is plotted for improved visualization of the measurement deviation. All the measurements show an overestimation of particle diameter, with the measurements of the smaller diameter pin gages showing larger errors and more variation in error. In examination of the measurements of the two smallest pin gages, the size of a microlens in object space, shown in a dotted line, should be noted. The smallest pin gage has a diameter less than the diameter of a microlens while the next smallest pin gage diameter approaches the size of a microlens. This suggests that the sharp increase in error at these diameters is related to the resolution limits of the experimental system, however, it is promising that the smallest pin gage can still be measured.

Figure 58 presents the diameter errors, defined as (*measured diameter*) – (*known diameter*), for this same data set as a function of measured particle depth. The results are color coded by the known pin gage diameters. Diameter errors are nearly all less than 0.5 mm. As was evident in the previous figure, smaller diameters show larger errors. This trend is true through the entire diameter range examined, but there is a discontinuity in the magnitude of error increase as the pin gage diameter approaches the microlens diameter. Additionally, the errors increase with distance from the focal plane. This trend is more evident at decreasing diameters but does appear even in the largest pin gage diameter to some extent. It is suspected that this trend is a result of the increased blur outside of the DOF because the errors are relatively constant for each pin gage within a region approximately corresponding to the DOF, z = -41 to 50 mm for this experimental configuration.

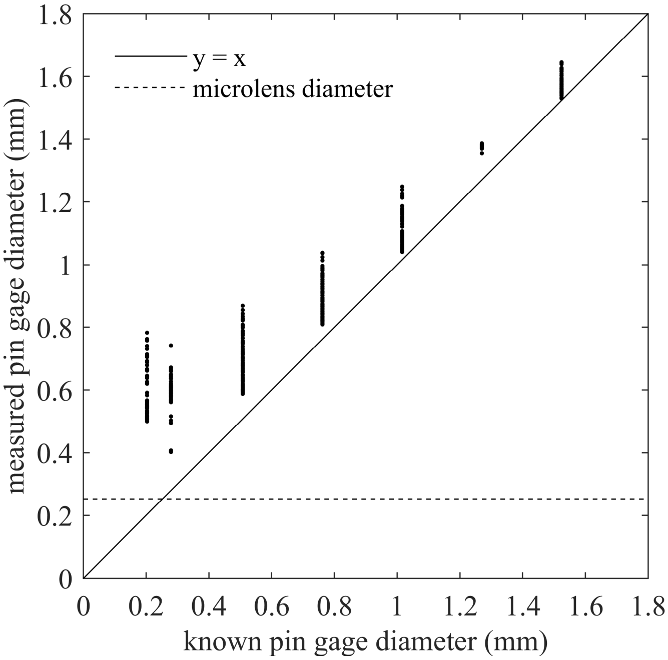

Figure 57. Measured diameter as a function known diameter for pin gage data set.

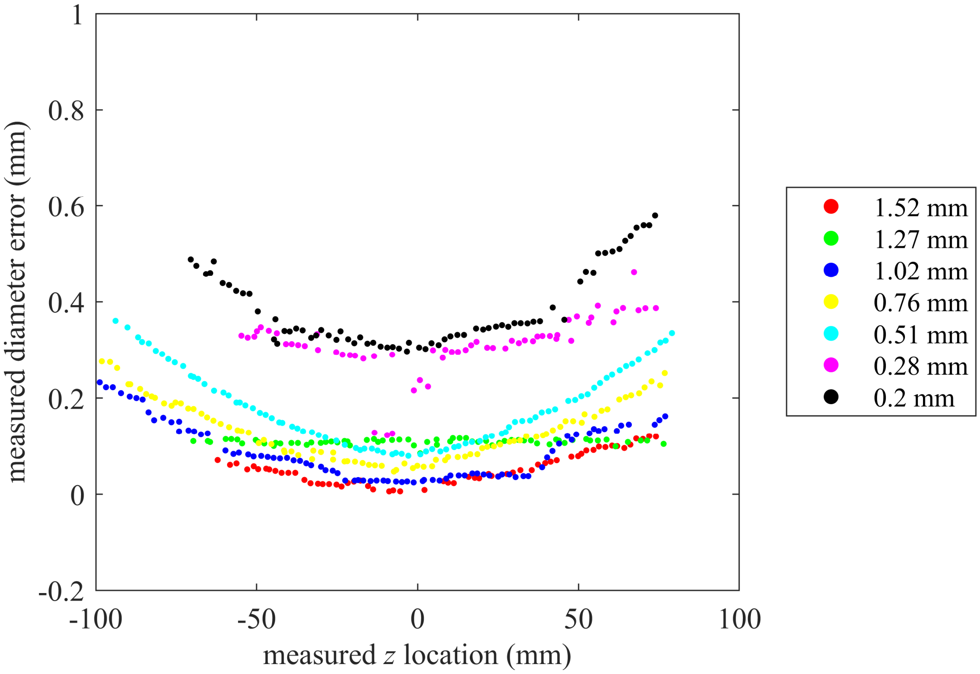

Figure 58. Measured particle diameter as a function of depth for pin gage data set.

As a visual justification of the depth dependent effect of blur, Figure 59 displays renderings of the same pin gage in the images from two different traverse positions. For each position, the center perspective view, refocused view, and resulting thresholded image are depicted. Comparison of the two depths shows significant degradation in the edge sharpness at the more extreme depth and correspondingly a blurrier refocused image. The end effect of this blur is more pixels identified as part of the particle by the thresholding. In examination of this figure, because the size of the in-plane region examined is based on the size of the particle in the perspective views, the region selected at the z = 50 mm depth is larger than at the z = 0 mm depth. This is not expected to affect the uncertainty because larger regions in physical coordinates use a correspondingly larger number of pixels, i.e., the resolution is the same in each. The in-plane size of the fragments does not appear to affect the depth errors for the range of diameters examined here, however, at extreme depths the blur does impact depth uncertainty as discussed previously.

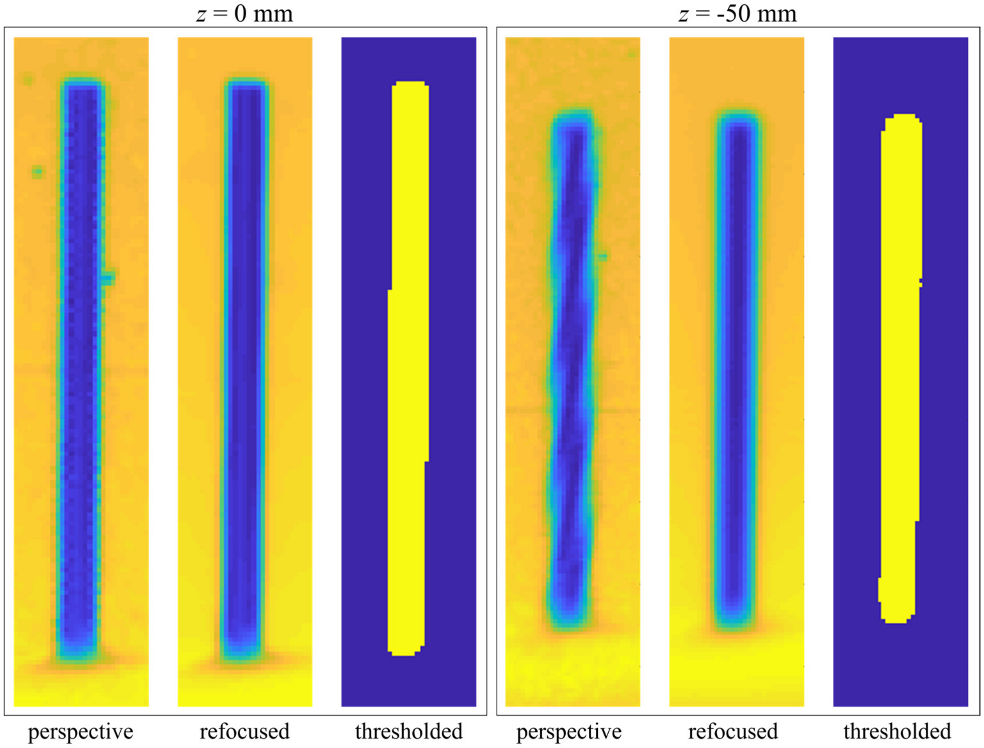

Figure 59. Perspective shifted, refocused, and thresholded images demonstrating the effect of blur on diameter.

iv. Effect of segmentation

As has been alluded to in the previous subsections, the image segmentation scheme can have an impact on the resulting identified particle size and shape. Here, this impact is assessed by examination of the same pin gage data set with the application of artificially modified image segmentation thresholds for determination of the in-plane pin gage diameters. As a reference for the magnitude of these effects, these in-plane errors are on the order of the pitch of a microlens in object space. These modifications were not applied in the initial image segmentation of the individual perspective views and therefore had no effect on the depth measurements, though improvements to the image segmentation at that stage could possibly affect depth uncertainty.

For the first variation, the threshold determined using the built in MATLAB function ‘graythresh’ (described in Chapter V Section A Subsection i) for each refocused particle region was scaled by 110%. These less stringent thresholds resulted in more pixels falling within the range identified as part of the pin gage. Figure 60 displays the measured pin gage diameters as a function of the known pin gage diameters with this modification. As expected, this results in even greater overestimation of diameters. In fact, some of the measurements are so large that they are not included in the plot to allow the same scaling in each of the threshold variation plots. Figure 61 presents the diameter errors as a function of depth for this modified threshold case. Again, erratic results are noted and in general errors are larger than when the calculated threshold is applied. Of particular interest, is the fact that measurements of the smallest pin gage are no longer present. In this case the less stringent threshold had allowed the entire refocused region to be defined as a particle and this region does not meet the restrictions of a valid particle. This threshold variation does not improve the results in this case and is additionally so extreme that unpredictable artifacts occur in some cases, such as the entire refocused region being identified as the particle.

For the second variation, the threshold determined for each refocused particle region was scaled by 90%, resulting in a smaller number of particles being identified as part of the pin gage. Figure 62 again displays the measured pin gage diameters as a function of the known pin gage diameters with lower modified threshold applied. This results in much better agreement with the expected particle sizes, though a slight discrepancy in the slope of the data and the $y = x$ line is present. The smallest diameters remain overestimates (though less so than the with the other thresholds) while the largest diameters are now slightly underestimated. In all cases the variation in measurements among the same size pin gage show far less variation. Of particular interest is consideration of the usefulness of these measurements for discrimination between different sized objects, these results now show no overlap in measured sizes for different particles except between the two smallest diameters. Figure 63 shows the diameter errors for this more stringent threshold case. In addition to the verification of the observations made from Figure 62, this plot also demonstrates that the depth dependency is significantly reduced, for some diameters entirely removed, by application of this lower threshold. This suggests that, for the particular conditions of this data set, this threshold appropriately selects a region closer to the true particle area and that the blur at the more extreme depths is above the adjusted threshold. The remaining presence of a trend relating diameter error and pin gage diameter should be noted, though the error variation over the diameter range encompassed in this data set is smaller in this case than when the original threshold is applied.

Moving to a still more extreme variation, Figure 64 and Figure 65 show the results when the threshold is scaled by 80%. This threshold results in an underestimate of nearly all measurements and for the larger diameter pin gages, reintroduction of a relationship between depth and error. When this 80% scaling is applied, there are no valid measurements of the smallest diameter pin gage as so few pixels remained within the valid range of particle intensity. This inability to measure the small diameter objects is the same final result as was seen in the 110% threshold case and in both cases is a result of such an extreme error in the number of identified particle pixels. Particularly in comparison of the errors shown in Figure 63 and Figure 65, it is expected that the ideal image segmentation scheme would be more advanced than a simple scaling of the identified Otsu threshold as used in the examples in this subsection. In particular, it appears that a scaling threshold that is variable with particle size might be appropriate as different particles show reduced error with different scaling. A more detailed study including a wider range of shapes and sizes would be necessary to implement a robustly appropriate method.

An additional point of interest related to the effects of segmentation is in the measurements of occluded particles, such as the example in Figure 56. The measurement of the in-plane size and shape of occluded particles relies on the fact that a modified version of refocusing is used in which only the views in which the particle is not occluded contribute to the refocused image. Since this refocused image is created in a small region surrounding the particle in some cases the neighboring ‘occluder’ particle also lies within this region. If the particles can still be separated by the thresholding, this poses no problem. However, it is possible that, depending on proximity, that when the thresholding is such that the sizes of particles are overestimated both particles could be identified as a single particle in the in-plane dimensions. This results in particles that are correctly separately identified in 3D space, but that are both defined as consisting of the same shared in-plane size and shape. In the example in Figure 56 this was avoided by an artificial adjustment (threshold*0.95) of the thresholds which allowed correct separation of the particles in the refocused regions.

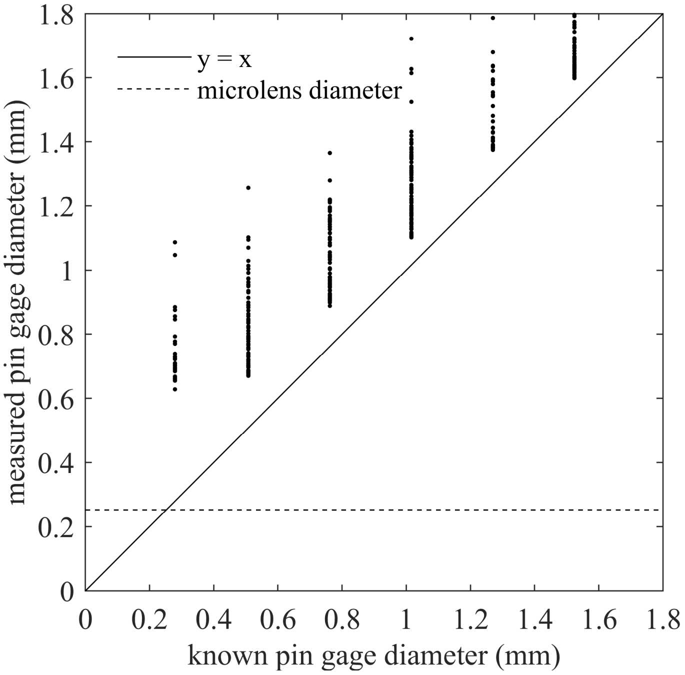

Figure 60. Measured diameter as a function known diameter for pin gage data set with artificially relaxed threshold of 110%.

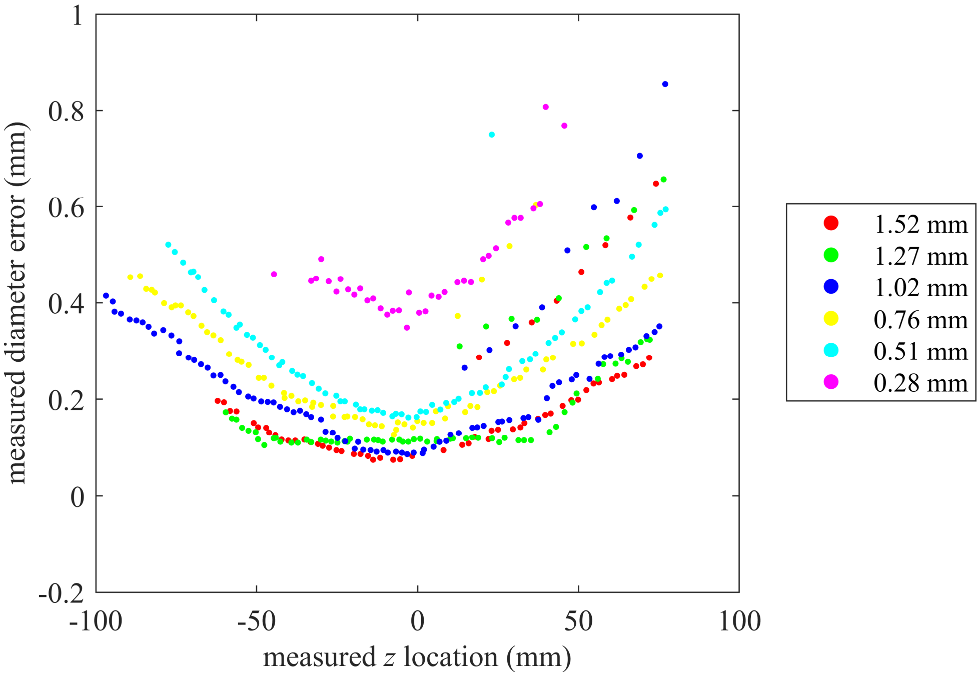

Figure 61. Measured particle diameter as a function of depth for pin gage data set with artificially relaxed threshold of 110%.

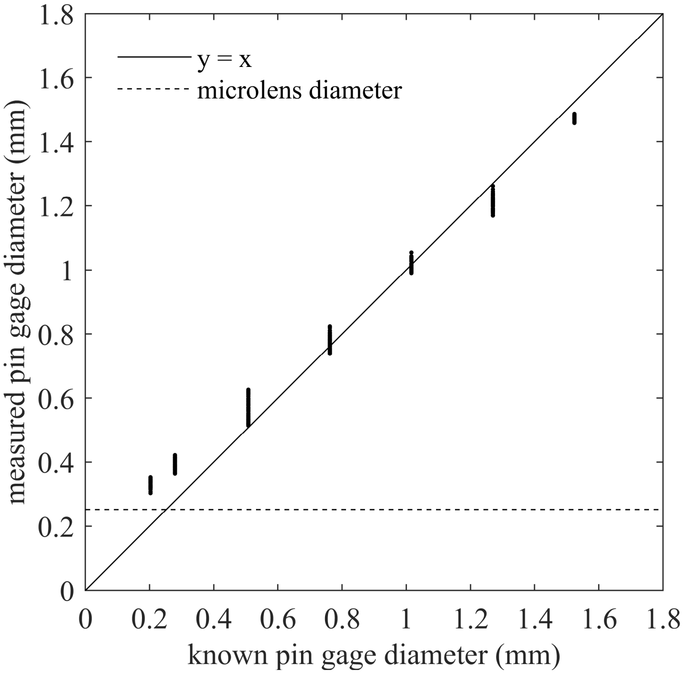

Figure 62. Measured diameter as a function known diameter for pin gage data set with artificially stringent threshold of 90%.

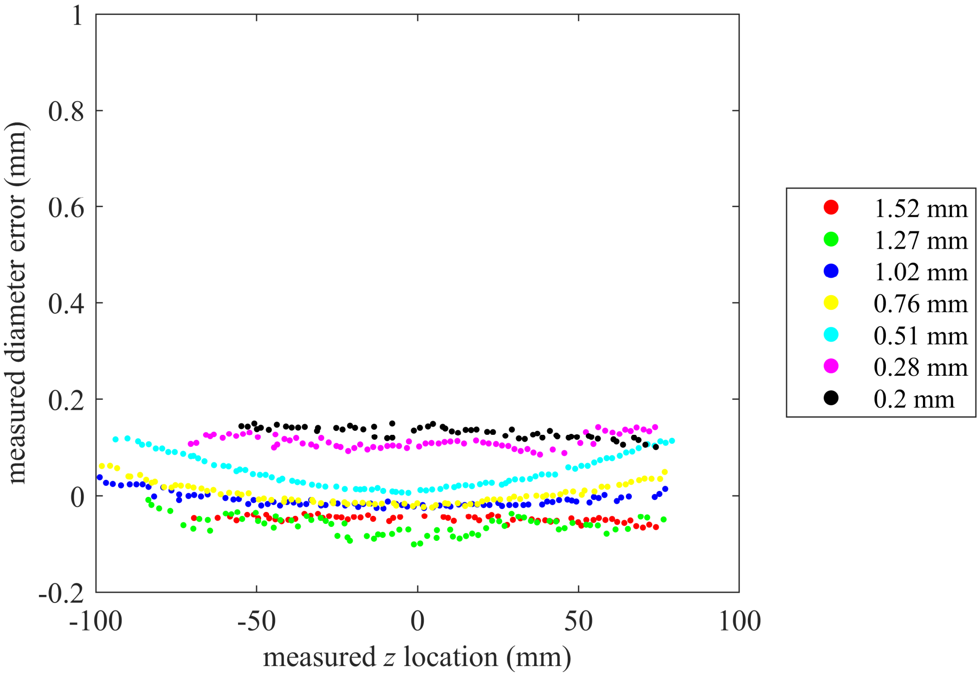

Figure 63. Measured particle diameter as a function of depth for pin gage data set with artificially stringent threshold of 90%.

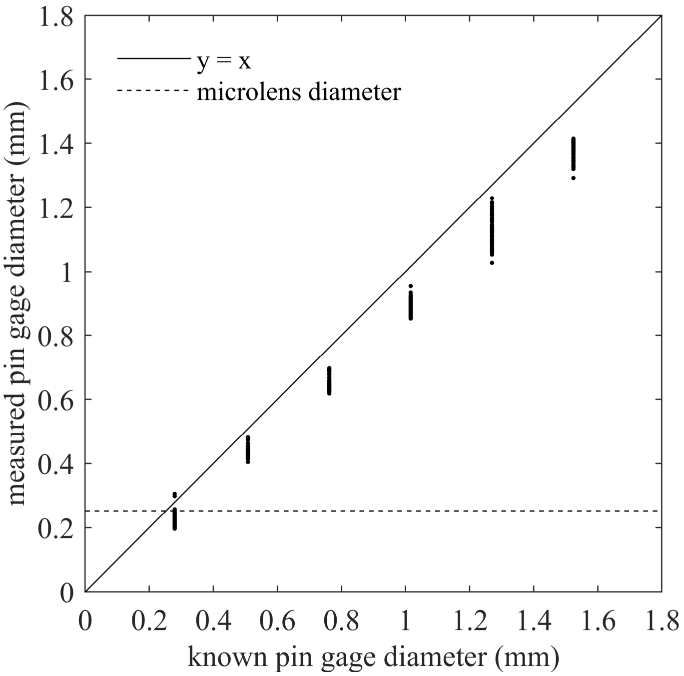

Figure 64. Measured diameter as a function known diameter for pin gage data set with artificially stringent threshold of 80%.

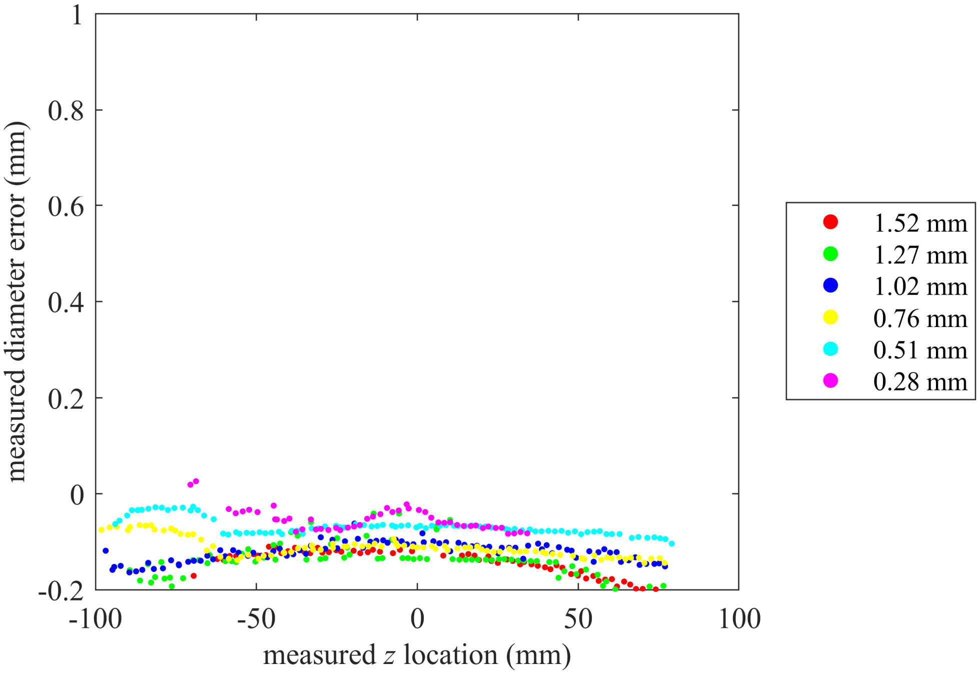

Figure 65. Measured particle diameter as a function of depth for pin gage data set with artificially stringent threshold of 80%.

D. Summary

Application of the refocusing and perspective shift based methods to a static particle field image data set shows improvement in measurement uncertainty and computational efficiency is achieved using the perspective shift based method. Average depth precision within 0.4 mm and accuracy within 0.1 mm is achieved over a range of 50 mm. In addition, the required computational time is reduced by approximately two orders of magnitude. The measurement of large aspect ratio particles indicated increased uncertainty as compared to spherical particles. The perspective shift method was shown to allow measurement of some obscured objects, though this capability is limited by the main lens diameter. The in-plane measurement accuracy was also examined and shown to be highly dependent on the image segmentation scheme implemented.

VII. Measurement uncertainty analysis

The previous chapter has assessed the measurement error and associated uncertainties achieved in measurement of 3D particle location using the perspective shift algorithm. To enable future improvements of these measurements, the current chapter will examine the expected impacts of various error sources. Synthetic and experimental calibrations will be used to assess both the mechanisms throughout the algorithm through which error is introduced and the propagation of error from raw light field measurements to particle locations. The measurement error examined in this dissertation is a result of the compilation of errors introduced by various phenomena.

In the following subsections, synthetic centroid location error is examined through the use of a synthetically generated DLFC polynomial mapping function. The synthetic calibration creation functionality of the Dragon plenoptic software suite was used, further details of the synthetic calibration implementation can be found in Fahringer [82]. Error was introduced into simulated particle measurements in a manner similar to a Monte Carlo simulation. First, a uniform random distribution of (x,y,z) coordinates representing object space particle locations was created within a defined volume of interest. Second, the DLFC was applied to the points for a range of (u,v) coordinates (the same range used throughout this work), resulting in a list of (s,t) coordinates corresponding to each of these randomly distributed (x,y,z) points. Next, error was added to these (s,t) coordinates representing noise or a systematic error in the centroid measurements in each perspective view. These erroneous (s,t) coordinates were then used to determine (x,y,z), again using the DLFC polynomial mapping, and the discrepancy between the original and erroneous (x,y,z) coordinates was assessed as the resulting propagated error.

A. Error contributions

These points of error introduction can be broadly divided into those resulting from the experimental image collection and those resulting from the processing scheme. Here, a variety of possible error sources in each category are listed.

i. Experimental contributions

In conducting the uncertainty characterization experiments examined in this dissertation a great deal of care was taken to remove various sources of experimental error, however, some experimental errors still exist. These errors can be considered a near best case scenario as experimental limitations such as space or time constraints or complexities required in specific applications can increase these errors.

First, consider errors introduced by the experimental volumetric calibration procedure. The translation stage displacement accuracy introduces some error. In this work, automated translation stages with an accuracy of within 4.5 μm were used. The magnitude of this error could vary significantly as a result of a less accurate translation method. For example, in a confined space it might be necessary to use a manual translation stage which could easily reduce the accuracy to within 0.5 mm. In the uncertainty characterization experiments, stage accuracy also impacted particle measurements, effectively doubling the impact of this error source, though the impact of the particular translation stages used in this work are small, as stated above. A related error source is any uncontrolled motion of the calibration target with respect to the motion of the calibration stage due to a lack of rigidity in the calibration target mounting. Similarly, motion of the static particle field relative to the mounting system could result in error. A final source of error related to the volumetric calibration is the accuracy of the calibration target dot spacing.

Other sources of experimental error result from limitations in the camera system. First, the spatial sampling rate is limited by the resolution of the microlens array, therefore, even with the use of a high-resolution camera the spatial discretization of collected light can be limited. Second, lens distortion introduces error in the apparent location of imaged objects. The volumetric calibration is designed to correct these errors, but it is possible that some effects of distortion remain.

ii. Processing contributions

Various sources of error are also introduced in the process of determining particle location from a raw plenoptic image. First, error is introduced by the mathematical method implemented to determine the particle image centroid. Second, the least squares estimation used in determination of the volumetric calibration polynomial introduces error. Third, the aperture size used to determine particle measurements, or the selection of the perspective views that are included in the measurement, introduces error if low quality views are used. Fourth, the method of image segmentation, here a threshold based binarization, results in some error. Fifth, the restrictions implemented in the clustering implementation may result in error. The impact of this error is highly dependent on the specific processing parameters selected as well as detailed differences in the raw data. Finally, the conversion from the hexagonal microlens array to a rectilinear output image introduces interpolation error.

In the following sections, those error sources that have been identified as the most influential are examined in detail. In particular, the relative effects of mechanisms that may be impacted by the image processing routine developed in this dissertation are examined in an effort to guide future investigations in reduction of measurement error as the largest contributors likely allow the best opportunity for improvement. The sources of error considered in detail here are listed in Table 5.

Table 5. Contributions to error.

Error source	Description
Centroiding method	Error resulting from the mathematical method implemented to determine the particle image centroid
Volumetric calibration	Error resulting from the least squares estimation in the calibration polynomial
Aperture size	Error resulting from the selection of perspective views included in the measurement
Sampling rate aliasing	Error resulting from the limitation in spatial sampling rate
Image segmentation	Error resulting from the threshold based image segmentation method implemented

B. Centroiding method

It is expected that the centroiding method implemeneted has some effect on location accuracy. Specifically, from Matsuoka et al. [83], the expected RSME of centroid locations is on the order of 0.05 to 0.1 pixels for the particle diameters of interest and the relevant centroiding method in the current work. It should be noted that the discussion in this subsection is limited to error resulting from the determination of a centroid from a perspective view and does not consider error resulting from the conversion from the raw hexagonally sampled data to the rectilinear grid. That previous work considered a variety of quantization levels in determination of centroids; the unweighted centroid method (or $n = 1$ quantization level) corresponds to the centroid measurement method used in the current work in which the image is binarized. The average and standard deviations of depth error for 0.09 pixels maximum of noise addition are 0.010 mm and 0.013 mm respectively, using a synthetically generated calibration. These values are smaller than the average and standard deviation of depth error measured experimentally and shown in Figure 43 and Figure 44 using the perspective shift algorithm suggesting that error in centroid measurement method independently is not the primary cause of uncertainty. These values do show that, as in the experimental data, the standard deviation of error is larger than the average.

Figure 66 allows a more detailed examination of the error at a noise level of 0.09 pixels in plots of the average error and standard deviation of error as a function of particle depth. These plots show that the in-plane error is independent of depth but, the depth error shows a slight increasing trend in the average and standard deviation of error with distance from the camera. It is suspected that this is a result of the fact that a pixel in a perspective view, the defining plane of the (s,t) coordinates to which noise is added, represents increasingly larger portions of object space at increased distance from the camera. This means that the addition of a given number of pixels of noise to the position of a particle close to the camera is equivalent to a smaller error in physical space than the addition of the same number of pixels of noise to a particle farther from the camera.

A second point of consideration in the uncertainty of centroid measurements is the dependency of uncertainty on particle size. From Matsuoka et al. [83] it is expected that the root mean square error (RMSE) of a centroid measurement decreases with increasing particle diameter. Matusuoka et al. also showed that in the measurement of centroids using a weighted centroid method resulted in overall smaller error, however, this improvement was most significant for smaller diameter particles than examined here [83]. In future work, the use of a weighted centroid method could improve the algorithm.

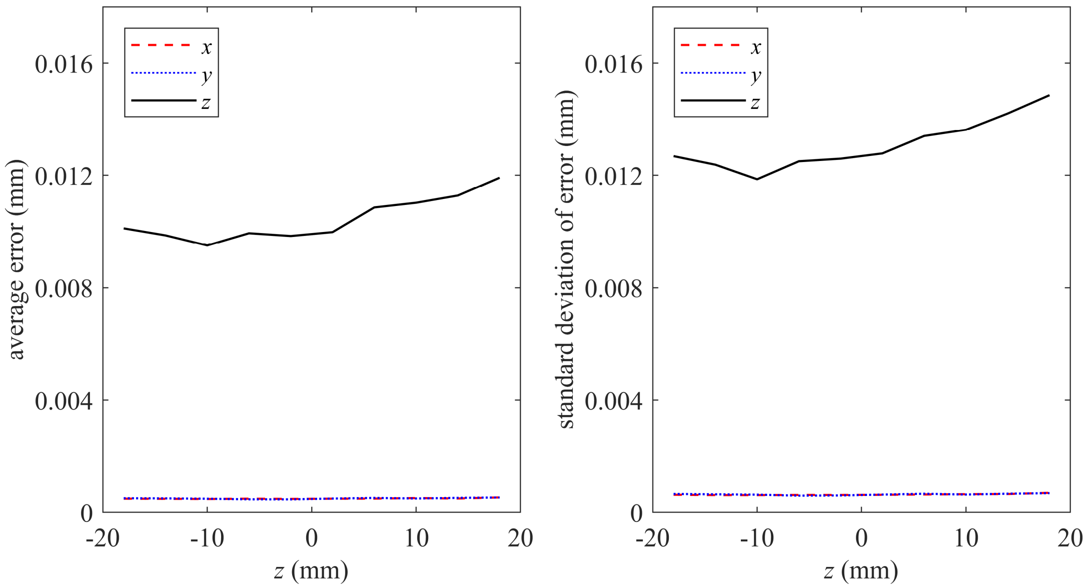

Figure 66. Average and standard deviation of error in (*x*,*y*,*z*) position as a function of particle depth for added noise of 0.09 pixels.

C. Volumetric calibration

Inaccuracies in the volumetric calibration are another contributing factor to error in the measured perspective view centroid positions. To assess the magnitude of these errors the calibration polynomial has been utilized to examine the calibration target dot positions used to create the calibration. This was executed by applying the polynomial mapping to the known (*x*,*y*,*z*,*u*,*v*) positions to calculate the corresponding (*s*,*t*) positions defined by the calibration and comparing these values to the original (*s*,*t*) positions used to create the calibration. Error was then defined as the discrepancy between these two sets of (*s*,*t*) coordinates.

The resulting average and standard deviations of error in (*s*,*t*) as a function of calibration target depth are shown in Figure 67 for two different experimental calibrations. Figure 67 (left) shows the results from one of the dot card calibrations from the original static particle field experiment with a nominal magnification of -0.35 and a depth range of 50 mm, entirely within the DOF at this magnification. These errors show no significant correlation with depth and averages and standard deviations of less than 0.05 pixels. As an example of a calibration executed over a larger relative depth range Figure 67 (right) shows the errors from the expanded parameter static particle field experiment with a nominal magnification of -0.3 and a depth range of 200 mm. As a reminder, the DOF of this configuration is from -41 mm to 50 mm. This calibration not only has slightly larger errors within the DOF, but also shows significant increases in error outside the DOF.

To further assess these trends, Figure 68 shows the calibration errors for the near and far depth calibrations from the same data set shown in Figure 67 (left), expanding the total measured depth to 150 mm. In both the near and far configurations increased error with increased distance from the focal plane is evident, though this trend is more significant in the near configuration (likely a result of the difference in the near and far DOF). Though this same trend is evident in the 200 mm depth calibration, the degradation is smaller in the three separate 50 mm cases. It should be noted that the difference in magnification is also expected to impact these errors, however, if the calibrations were of equal quality it would be logical that the magnification of -0.35 (50 mm depth ranges) configuration would have larger error due to the smaller DOF (this increase is evident in a similar examination of the magnification of -0.5 case, not shown here for brevity). Therefore, it appears that a higher quality calibration is achieved in measurement of a smaller depth range. This suggests that not only does the calibration degrade at extreme depths but also that the increases in error outside the DOF can negatively affect the error in the near focal plane region, supporting the argument made in Chapter VI Section C Subsection i concerning the effects of a large depth calibration.

These errors represent the minimum expected impact of the calibration on centroid measurement error. The magnitudes of these errors, on the order of 0.1 pixels, suggests that calibration error likely has only a small impact on the propagated depth error in general, but it should be emphasized that these magnitudes are the errors resulting from using the calibration to calculate the (*s*,*t*) positions originally used to create the calibration and are therefore the minimum expected error.

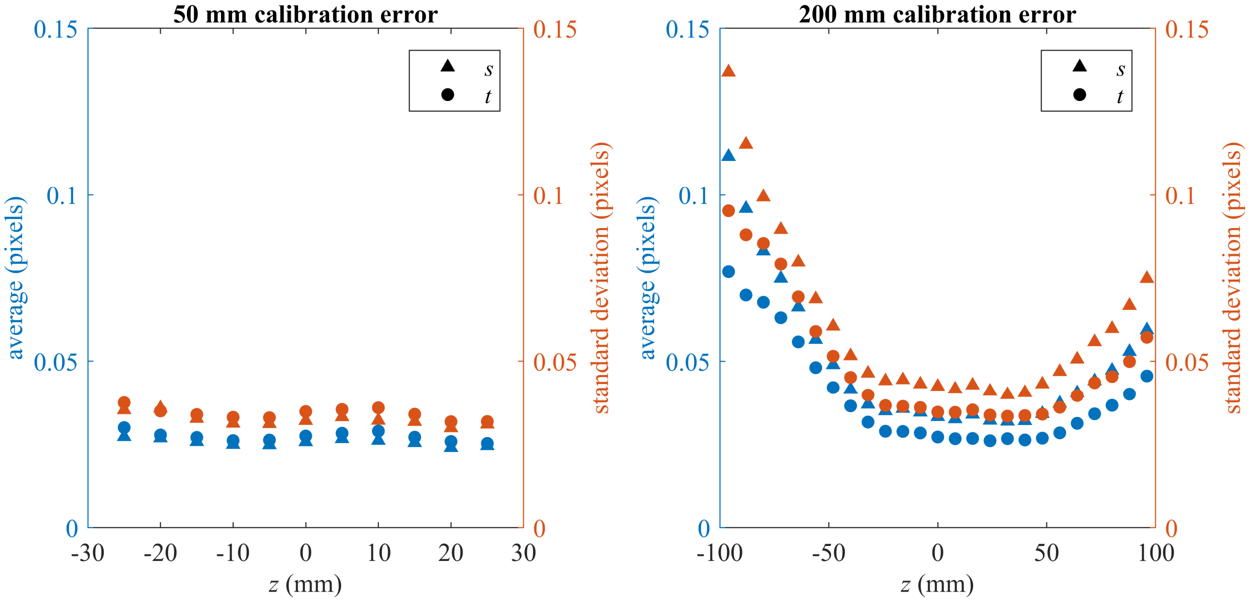

Figure 67. Average and standard deviation of error in (*s*,*t*) position as a function of calibration dot depth for 50 mm (left) and 200 mm (right) depth range calibrations.

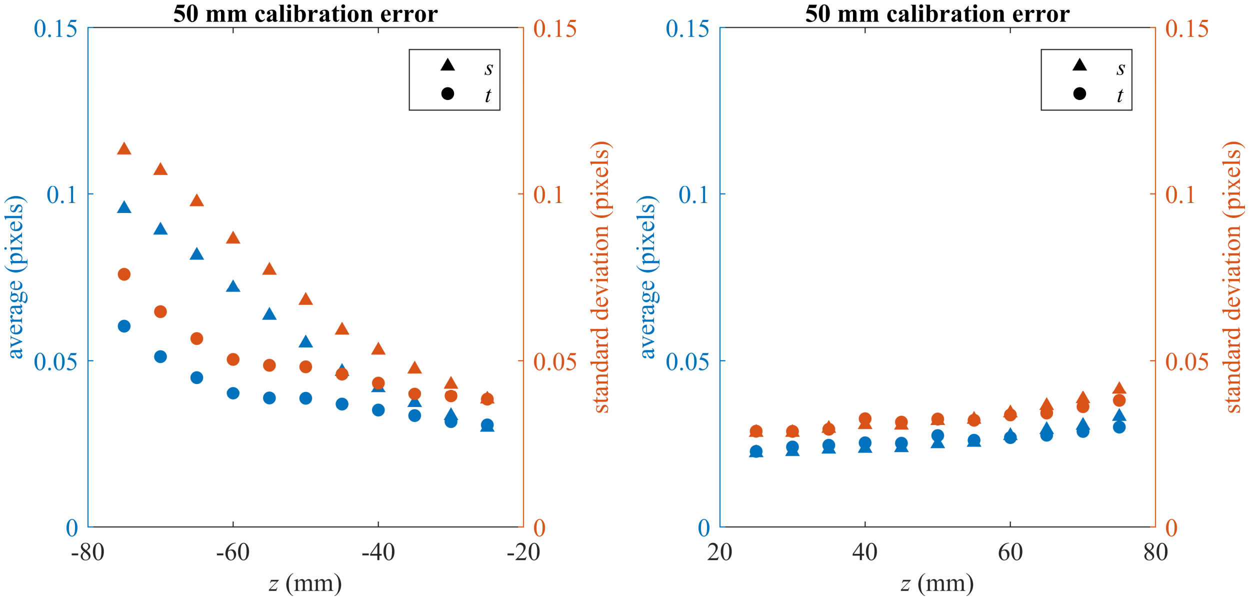

Figure 68. Average and standard deviation of error in (*s*,*t*) position as a function of calibration dot depth for near (left) and far (right) depth configurations.

Additionally, a small number of these measured errors were significantly larger with errors in the depth range of 50 mm case of up to 0.45 and 0.35 pixels in the *s* and *t* directions, respectively, and in the depth range of 200 mm case of up to 0.71 and 0.61 pixels in the *s* and *t* directions, respectively. Therefore, in some measurements the calibration is likely to have a more significant impact. It is possible that this impact could be reduced in implementation of a self-calibration procedure, particularly in configurations where a large measurement depth is required, and significant degradation is expected.

D. Aperture configuration

The effective aperture size used to extract particle measurements using the perspective shift method is variable based on views included in the measurement. In stereo imaging it is known that a larger parallax angle improves measurement quality; additionally, it is expected that the redundancy resulting from a larger number of view improves results to some extent. Here, the errors resulting from variations in the views included in particle measurement are considered.

i. Error scaling

In the plenoptic camera arrangement examined here, the views near the edges of the aperture are expected to be noisier as a result of vignetting and, eventually, the impacts of neighboring subaperture images. Therefore, the improvement resulting from increasing the aperture size must be weighed against the degradation resulting from noisy edge views. Erroneous microlens coordinate positions to examine this phenomenon were created as,

$$s_{error} = s + \left(u/u_{\max}\right) r \,, \tag{17}$$

where *s* is the original horizontal microlens coordinate of the particle in the view of interest, *u* is the horizontal angular coordinate of the particle in the view of interest, u_{max} is the maximum horizontal angular coordinate within the aperture, *r* is a uniform random noise with a maximum of

1 pixel, and s_{error} is the resulting error added horizontal microlens coordinate of the particle in the view of interest.

An important unknown that becomes evident in this discussion is how the noise scales with radial position; here linear and cubic scaling of noise addition are considered. This was executed using the synthetic calibration at three different aperture diameters and the resulting depth errors are given in Table 6.

Table 6. Varied aperture size error dependency.

Noise scaling	Depth error (mm)	7 pixel diameter aperture	11 pixel diameter aperture	15 pixel diameter aperture
linear	mean	0.102	0.062	0.045
	standard deviation	0.128	0.080	0.056
cubic	mean	0.017	0.026	0.036
	standard deviation	0.021	0.032	0.044

This indicates that under the assumption that noise scales linearly with radius, (u/u_{max}), the addition of more views improves the measurements while under the assumption that noise scales cubically with radius, $(u/u_{max})^3$, the addition of more views degrades the measurements. Note that in this table a diameter of 7 pixels corresponds to the use of the center view and all views within a radius of 3 pixels.

To evaluate the noise increase present in experimental data, the calibration errors considered in Section C above are examined as a function of the radial position of each view. Discretization of the error based on the radial position of each view allows analysis of the effect of including edge views that may be compromised due to vignetting or other degrading features. Figure 69 displays the average error in the (s,t) directions as a function of radial aperture position of each view for the 50 mm calibration examined in Figure 67 (left). The errors show a small increase with increasing radius until a radius of approximately 5 pixels is reached after which the error increases sharply. A similar trend is apparent in Figure 70 which displays the standard deviation of error in the (*s*,*t*) directions as a function of aperture radius for the same calibration. In this example the error is larger in the *t* direction, however, this appears to be dependent on the specific calibration examined as in Figure 71 and Figure 72, which show the same plots for the 200 mm calibration, the error is larger in the *s* direction. In both cases the difference in the two in-plane dimensions is small. The plots from the 200 mm calibration show a similar trend with a slight increase over most of the aperture until a sharp increase at a radius of 5 pixels. In both calibrations the sharp increase is at a similar radius indicating that is a true limit based on the microlens and pixel sizes for these similar magnification configurations, not an effect of the calibration. These errors also indicate that although the noise does increase for views at a larger radius, the increase is small for all views within the 11 pixel diameter, therefore it is expected that the use of an 11 pixel diameter produces the best available measurements. In these data sets a larger diameter is not feasible as a valid calibration cannot be executed due to the degradation of the edge views. This suggests that in general, the use of all views that can be successfully calibrated is advisable.

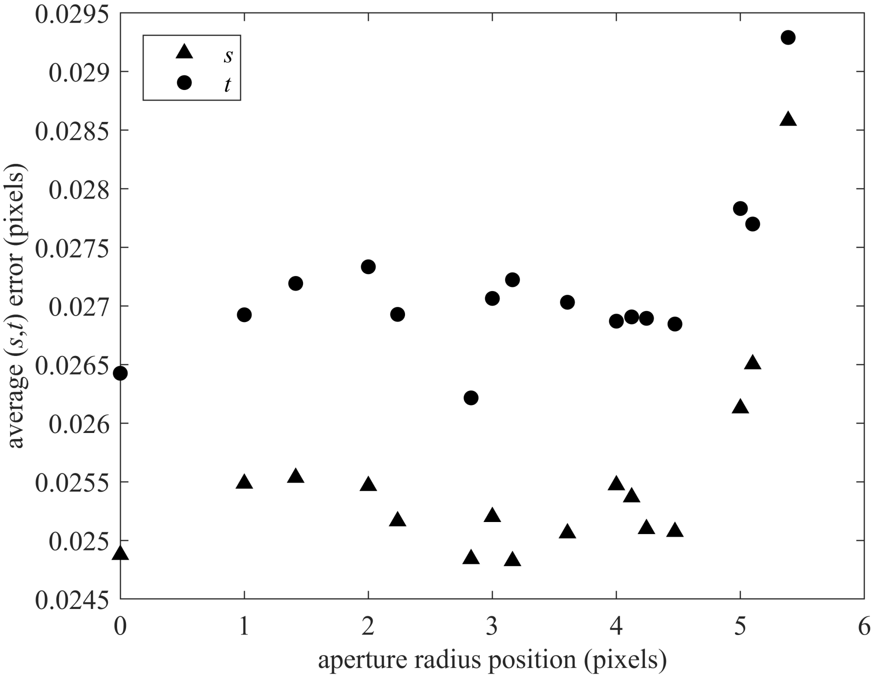

Figure 69. Average error in (*s*,*t*) position as a function of the radial position of a view, 50 mm calibration.

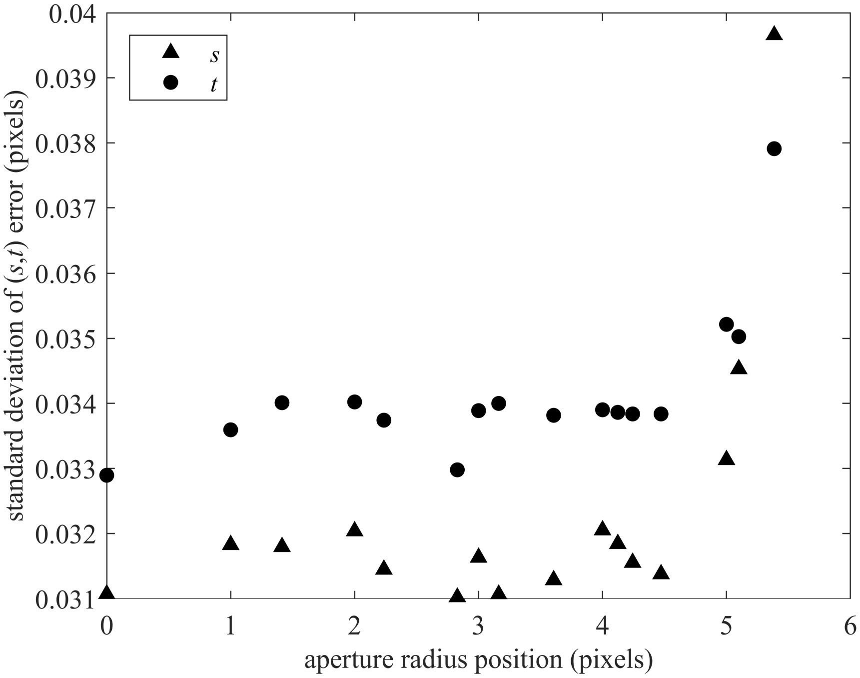

Figure 70. Standard deviation of error in (*s*,*t*) position as a function of the radial position of a view, 50 mm calibration.

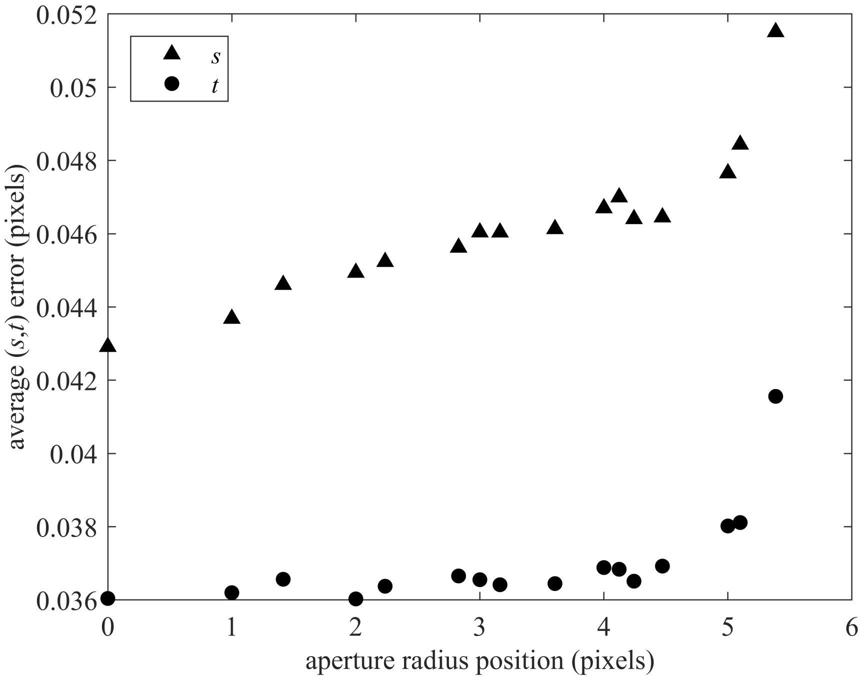

Figure 71. Average error in (*s*,*t*) position as a function of the radial position of a view, 200 mm calibration.

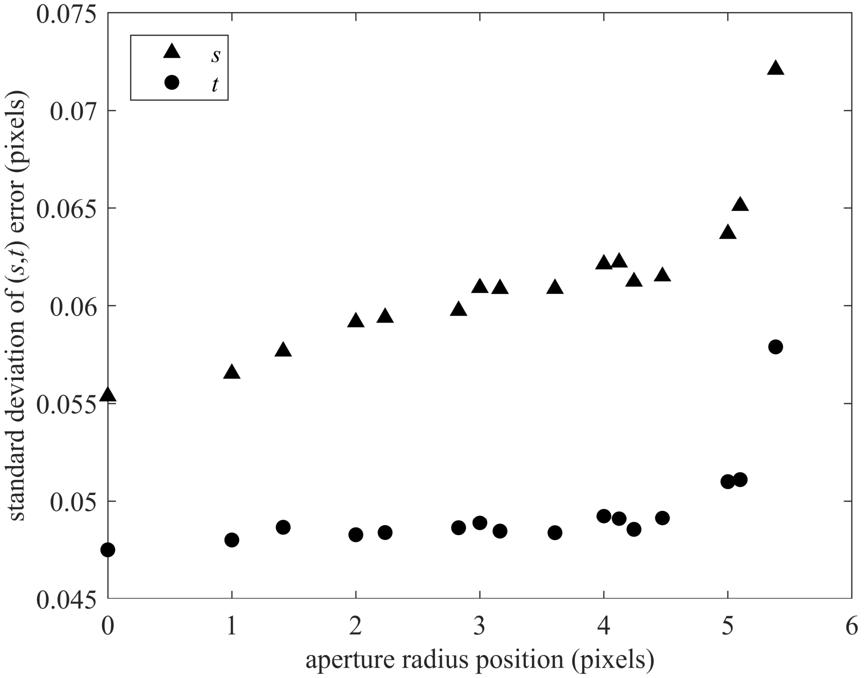

Figure 72. Standard deviation of error in (*s*,*t*) position as a function of the radial position of a view, 200 mm calibration.

ii. Number of views

A related error contribution consideration is simply the number of views in which a particle is identified. This number is variable; as stated previously, this variability is an important benefit of the perspective shift method due to the flexibility it allows. However, the number of views in which a particle is located may also impact uncertainty and is not necessarily tied to the size of the aperture because any combination of views can be used to measure a particle. Figure 73 shows a plot of the average error in each direction as a function of the number of views in which a particle was located, note that the arrangement of the views for each particle was random. These results show that calculation of particle positions from a small number of views has only a minor impact on the resulting errors in the in-plane dimensions but a significant impact in the depth direction and improved results are achieved from more views.

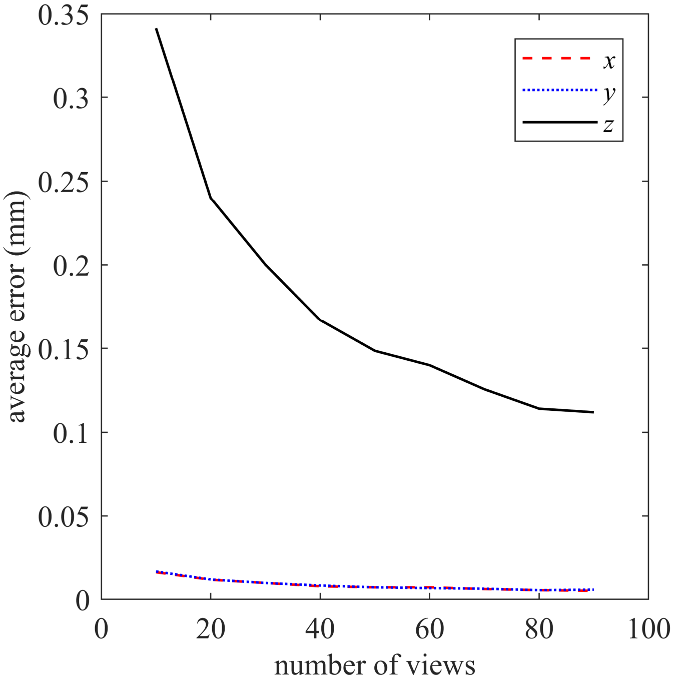

Figure 73. Error as a function of number of views in which a particle is measured using a synthetic calibration.

In experimental data this improvement may be more dramatic as a result of unpredictable experimental factors. For example, if a particle can only be located in a few views, it suggests that some image artifact (such as overlap or vignetting) has affected the other views to the extent that reliable measurements were not available. It then remains likely that the remaining views were impacted to some extent by the artifact and may still be degraded. The effect of these errors probably varies significantly depending on the specific parameters defining a valid measurement.

iii. Aperture size

To assess the effect of the aperture size on the error of triangulated particle position, views within a specified aperture diameter of the calibration target dot grid images were selected. Then each of these subsets of views were used to calculate 3D dot positions. Error was defined as the discrepancy between these calculated positions and those defined by the calibration. This calculation was repeated for a variety of aperture diameters using the 200 mm calibration data set discussed in previous sections. Figure 74 shows the resulting errors at each aperture radius in the *x*, *y*, and *z* directions. In all directions, error decreases with increasing aperture size, with a steeper decrease at smaller radii. At radii larger that approximately 4 pixels (or the inclusion of the center view and 4 views in each direction) the error appears nearly constant.

Figure 75 further investigates this trend and displays the errors in the depth direction only as a function of both aperture radius and depth position. Note that in Figure 75 depths with extremely large errors (beyond ±82 mm) have been excluded because inclusion of those depths does not allow visualization of the trends discussed above. From this plot it is evident that there is a strong relationship between error and depth for small apertures. For small radii apertures, depth error significantly increases with increasing distance from the focal plane. At larger apertures, again with radii of larger that approximately 4 pixels, there is no apparent dependence on depth.

This suggests that for measurements over a large depth range the use of the larger aperture examined here is necessary, but that if a smaller measurement volume is required the microlens radius could be reduced significantly. This is in agreement with previous work, in particular Fahringer [82], which determined that the ideal microlens diameter is such that the ratio of volume depth to DOF of a perspective view is 1.1. Therefore, for measurement of a smaller volume depth, fewer pixels are required behind each microlens. It should be additionally noted that changing the size of a microlens also affects the effective f-number of the aperture and in turn the DOF, thus, the scaling of all these parameters must be considered in determination of the appropriate microlens diameter.

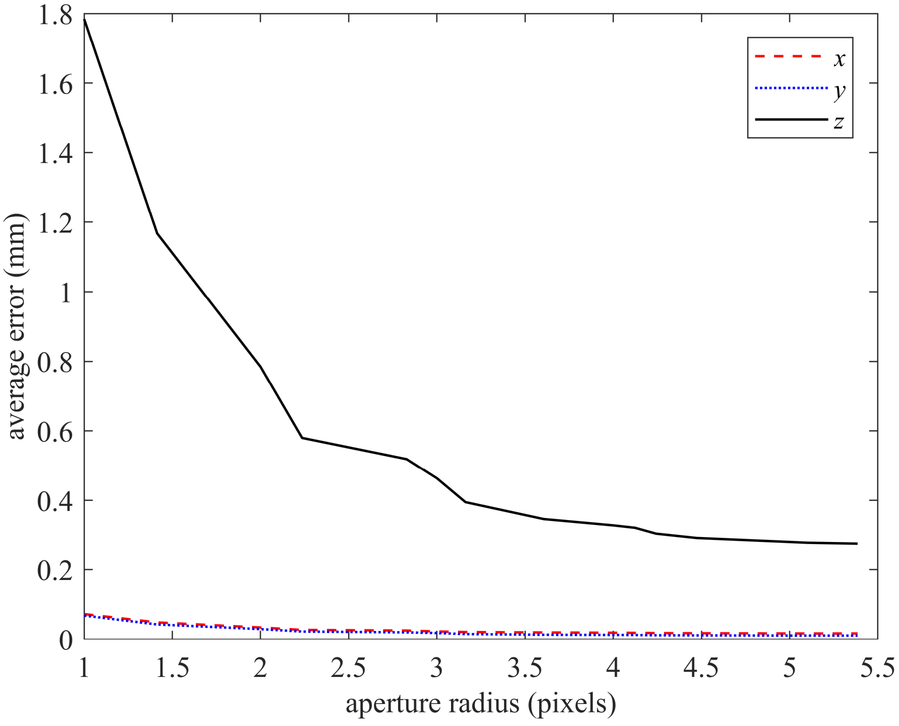

Figure 74. Error as a function of the extent of radial positions included in measurement.

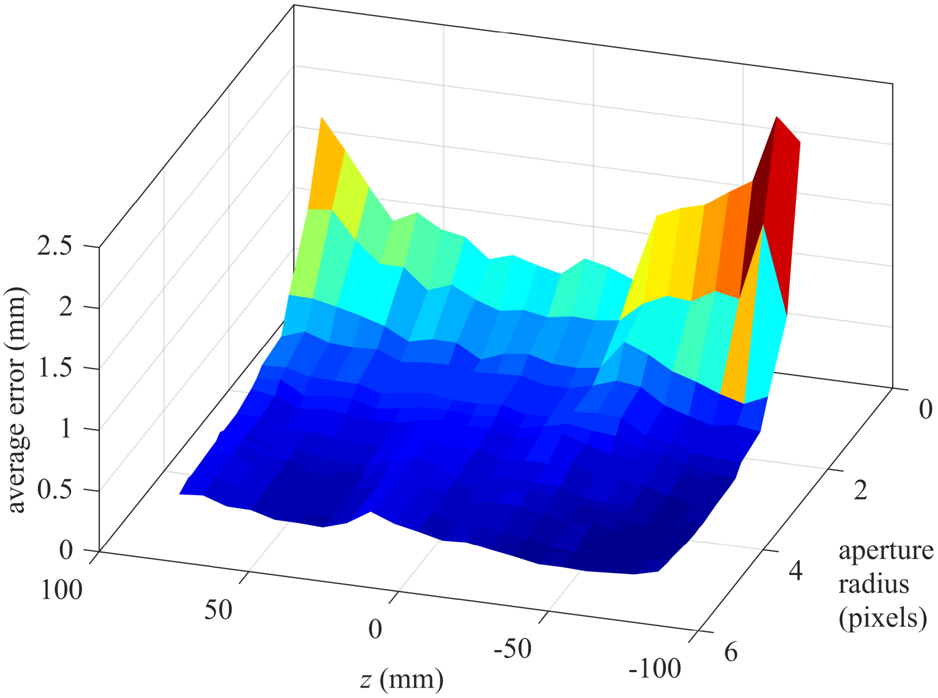

Figure 75. Depth error as a function of the extent of radial positions included in measurement.

E. Sampling rate aliasing

A significant source of image degradation that is easily qualitatively identifiable at extreme distances from the camera is aliasing resulting from the decreased spatial sampling rate in these regions. Here, calibration target dot grid images from an experimental configuration with a nominal magnification of -0.75, where the DOF is approximately z = -7.4 to 7.9 mm, are used to examine these effects as they provide a visually comparable metric. Figure 76 displays the center perspective view of a dot card located at the nominal focal plane. Since the dot card is within the DOF the dots are well focused and no degradation is evident. The red box indicates the location of the enlarged region shown in the bottom of the figure. This cropped region of the raw image from which the perspective view was created is overlaid with the microlens centroids or the locations from which the intensities used to create the perspective view are extracted. The cropped region encompasses the top right edge of a dot and examination of the intensities at the marked microlens centroids shows the expected monotonic gradient with increasing distance from the center of the dot. In this example the dot was large relative to the size of a microlens, therefore the spatial sampling rate was sufficient to result in a continuous and distinct dot in the perspective view.

Figure 77 similarly displays the center perspective view and enlarged region of the raw image of the dot card located at z = 25 mm. This is well outside the DOF, evident from the significant blurring in the perspective view, but not far enough that aliasing artifacts are apparent. Examination of the raw image segment shows that the entire dot is imaged in each microlens, spanning only a few pixels (about 3-4 pixels by visual inspection). Comparison of the intensities at each microlens center still shows a monotonic gradient with increasing distance from the center of the dot (located at the lower left corner of the raw image segment).

Moving even farther outside the DOF, Figure 78 shows the center perspective view and enlarged region of the raw image of the dot card located at z = 50 mm. At this depth, visual inspection of the perspective view shows degradation in the form of vertical and horizontal stripes in the blurred images of the dots. Examination of the raw image segment here shows that each dot appears on an even smaller number of pixels in each microlens (only 1-2 pixels by visual inspection). Comparison of the intensities at each microlens center in the raw image segment now shows that because the dot is sampled on such a small number of pixels in each microlens, the intensity gradient radiating from the center of the microlens is no longer monotonic. This is particularly evident in the vertical direction due to the closer spacing between microlens centers and corresponds to the stronger horizontal stripes in the resulting image artifacts. Therefore, these artifacts appear to be the result of spatial undersampling.

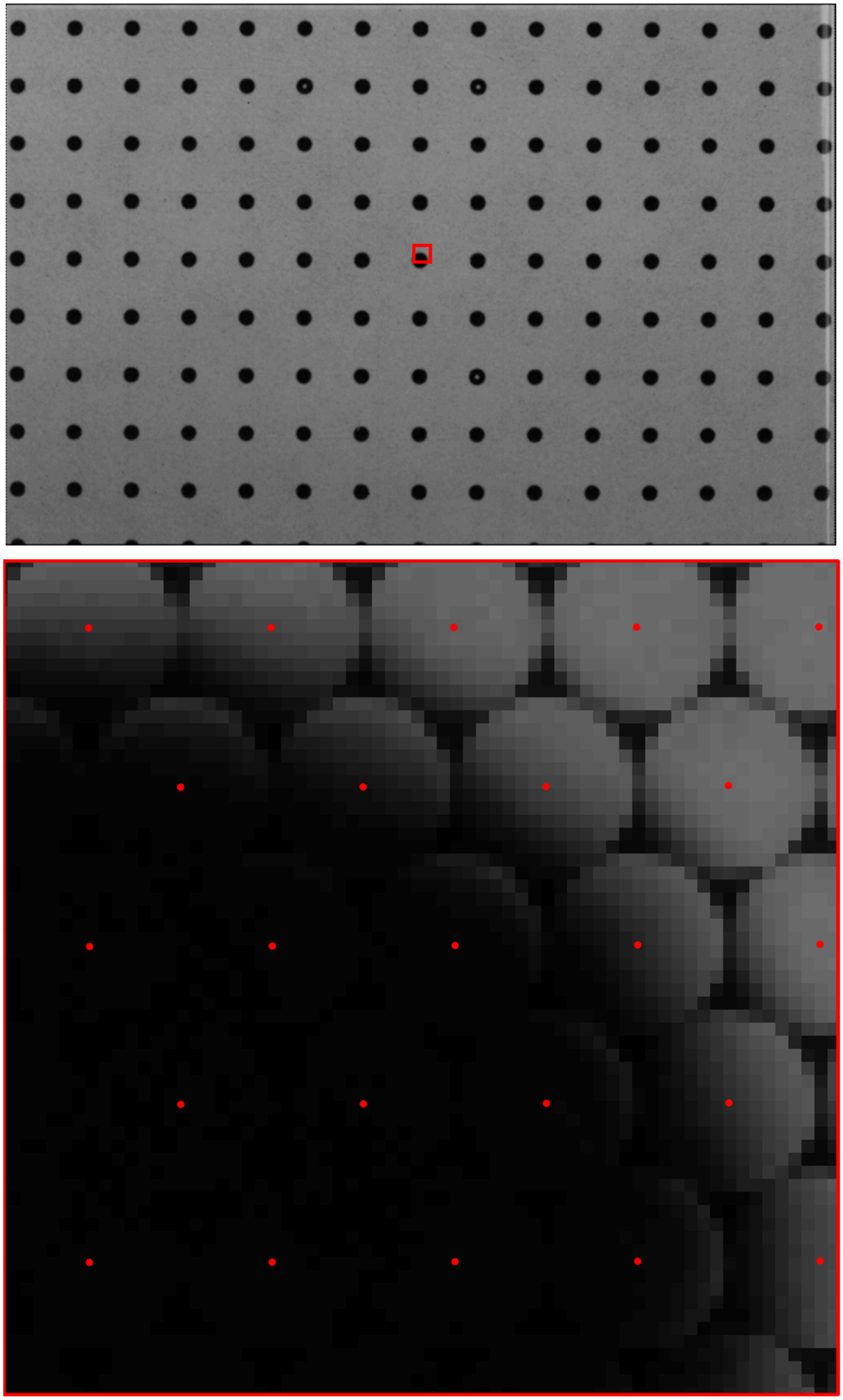

Figure 76. Perspective view (top) and enlarged section of raw image (bottom) of microlens centroid locations on *z* = 0 mm calibration target dot grid.

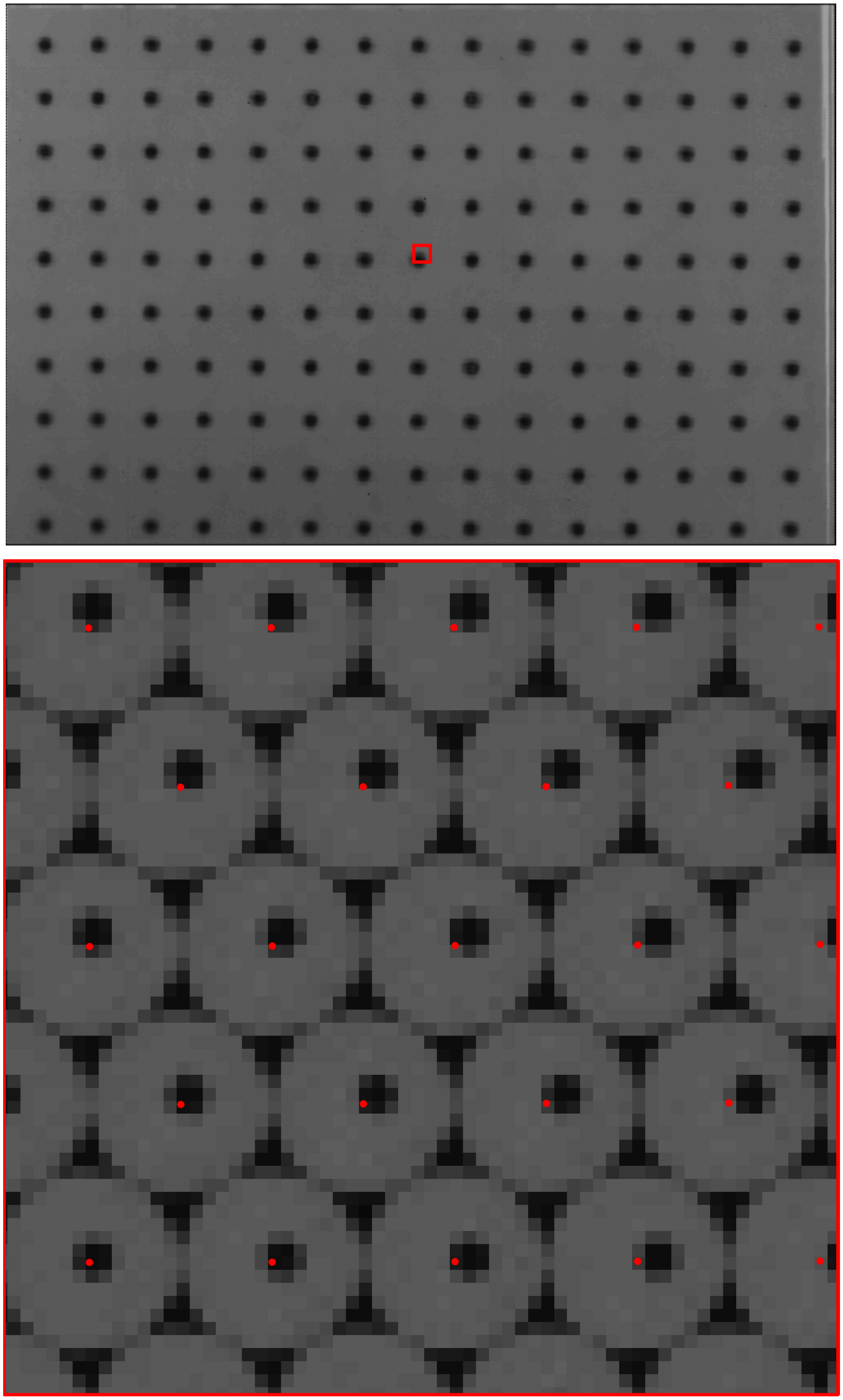

Figure 77. Perspective view (top) and enlarged section of raw image (bottom) of microlens centroid locations on z = 25 mm calibration target dot grid.

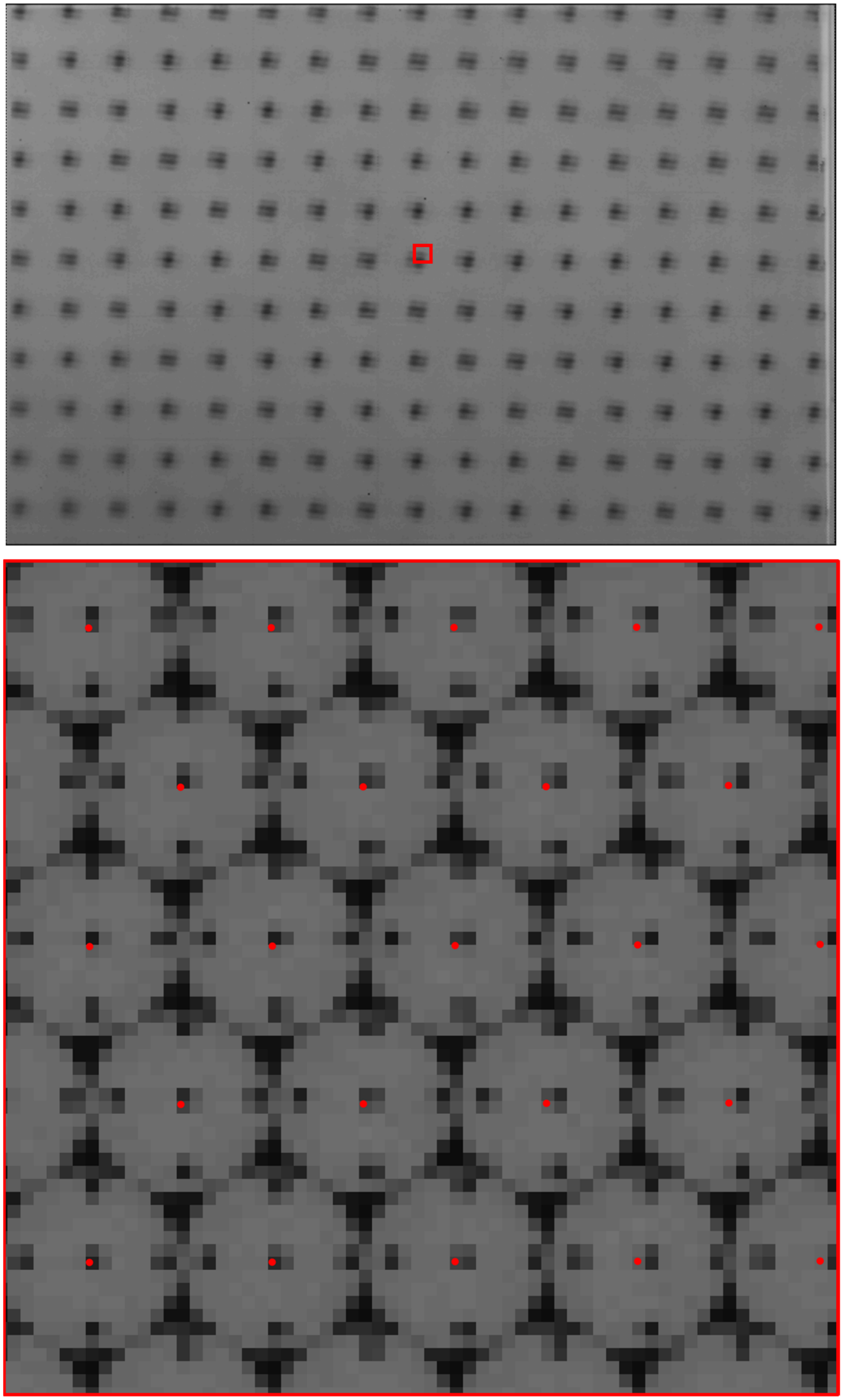

Figure 78. Perspective view (top) and enlarged section of raw image (bottom) of microlens centroid locations on $z = 50$ mm calibration target dot grid.

It should be additionally noted that the currently implemented interpolation scheme used to convert the raw hexagonal grid of microlens data to a rectilinear grid has been suggested as a source of this aliasing. However, this aliasing appears even in images created using the original hexagonal data, therefore allowing removal of this concern from consideration in analysis of this particular aliasing effect.

F. Image segmentation

The image segmentation scheme applied in this work and effects on the uncertainty of in-plane size and shape determination of particles has been discussed in previous chapters, however it may also affect particle centroid uncertainty. Specifically, in Chapter VI Section C Subsection iii diameter measurement errors of approximately 2 pixels were observed. Considering that the error propagation analysis in the current chapter suggests an expected centroid error of approximately 1 pixel, it is quite likely that the centroids are affected enough by errors in image segmentation to result in 3D position errors of the order observed in experimental data. Given that the true in-plane position of these particles is unknown in the experiments executed here, it is difficult to quantify these effects, however they appear to be bounded by the diameter error. To qualitatively examine the effects of image segmentation on measured centroid position, a perspective view from a calibration target is examined. Shown in Figure 79 is one of the most extreme views used in the perspective shift implementation developed here. In this figure colored boxes identify three dots of interest which will be used to evaluate differences in segmentation resulting from vignetting along the left side of this view.

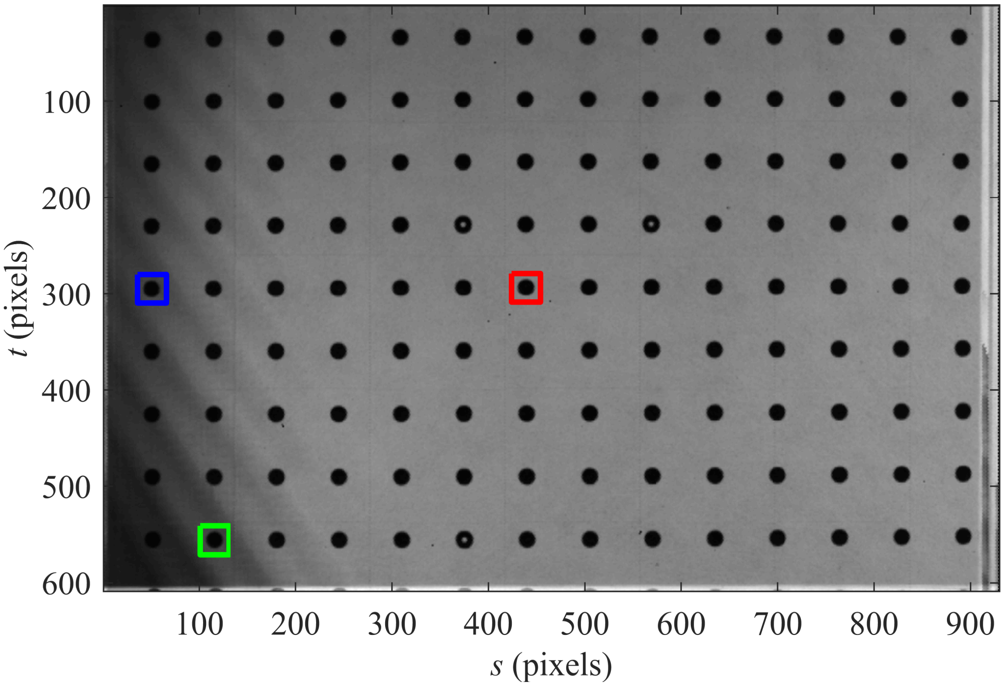

Figure 79. Calibration target perspective view overlaid with colored boxes indicating dots of interest.

First, consider the dot boxed in red as an example of a dot not expected to be affected by vignetting. Figure 80 (left) shows an enlarged image of this region (with increased contrast for clarity) overlaid with the measured particle centroid and a white circle indicating a reference radius of 9 pixels. This is not the measured radius of the dot but will be used here as a point of comparison between the different dots. Visual examination of this image shows a qualitatively symmetric dot and the white circle appears well-centered with the image intensity. Figure 80 (right) shows a plot of the filtered image intensity at the *t* value of the centroid as a function of *s* position, the dotted line indicates the threshold used to binarize the image. Details on the filtering and thresholding process were given in Chapter V Section A Subsection i. These intensity profiles show the expected symmetry given the known dot symmetry and a significant difference between the intensity of the dot and background, this results in a binarization relatively insensitive to changes in the threshold. The symmetry is key because even if a significant error in threshold selection was made (as is expected based on the discussion in Chapter VI Section C Subsection iv), each side of the dot would be affected equally, and the centroid would be unchanged. Similar results are present in the vertical direction, the following discussion is limited to analysis of the horizontal centroid position.

Figure 81 shows a similar image and plot for the dot boxed in blue which is near the vignetted edge of the image. The enlarged image of the region still shows a qualitatively centered measured centroid and reference radius, however, the difference in background and foreground pixels is less distinct. Examination of the filtered intensity plot confirms the smaller intensity difference. Additionally, the intensity profile shows less symmetry in this case, with the right side of the dot resulting in slightly higher filtered intensities. This asymmetrical profile in combination with the smaller intensity separation means that changes in the threshold will have a different effect on each side and result in a change in the centroid. Given that previous results in this dissertation suggest inappropriate threshold selection, it follows that the centroid measured here is incorrect.

Figure 82 provides a more extreme example of this effect and displays the results of the green boxed dot near the corner of the image. In this case, careful visual examination of the enlarged image shows a discrepancy in the location of the reference radius circle and the dot location based on intensity. Specifically, the circle (and therefore centroid measurement) appear shifted to the right compared to the dot image in visual examination of the intensities just outside the circle. This is verified by the filtered intensity profile shown on the right which shows a more extreme asymmetrical tendency than in the case of the blue boxed dot. This asymmetrical result also allows easier visualization of the difference changes to the threshold would have on the right and left sides of the dot.

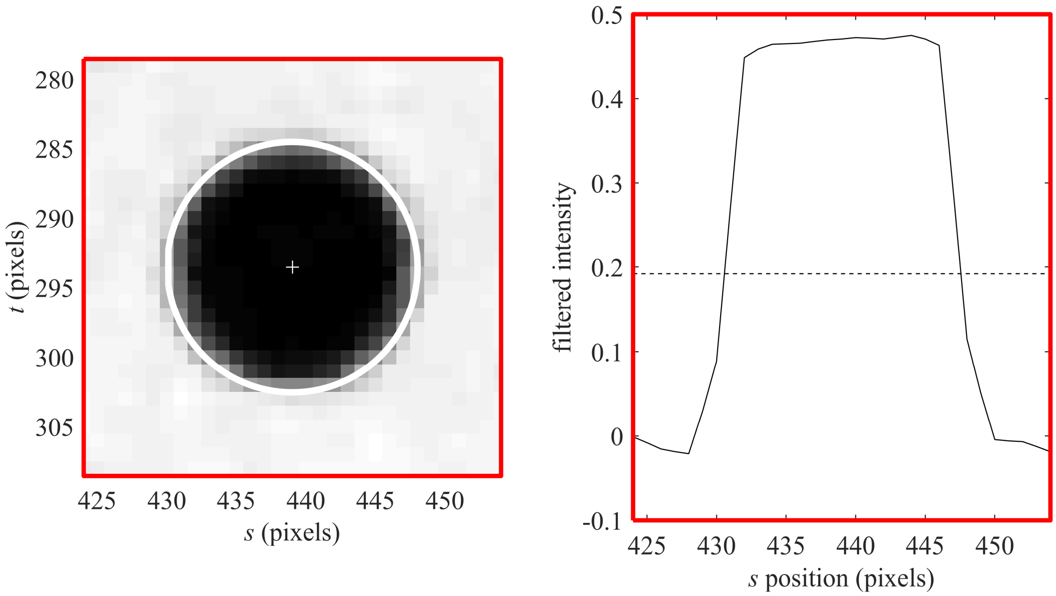

Figure 80. Red boxed example dot with measured centroid and metric radius (left), filtered image intensity at the *t* coordinate of the centroid as a function of *s* position (right).

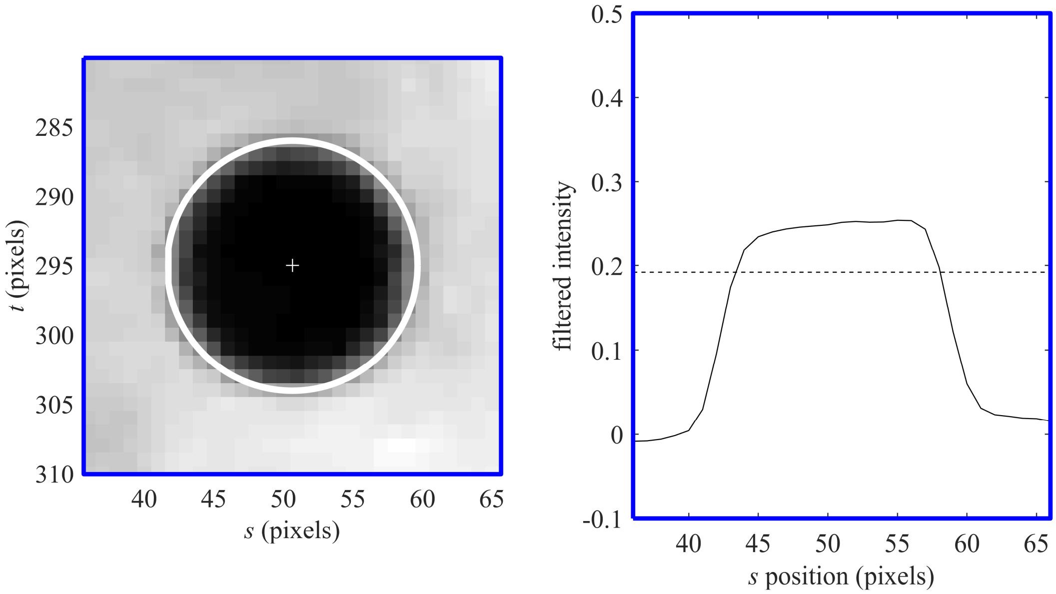

Figure 81. Blue boxed example dot with measured centroid and metric radius (left), filtered image intensity at the *t* coordinate of the centroid as a function of *s* position (right).

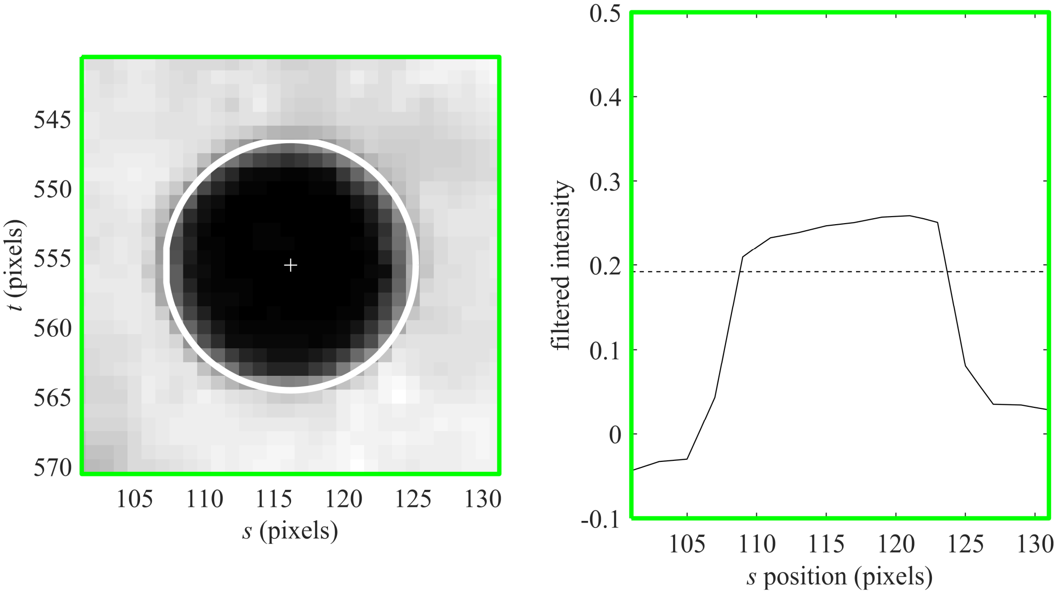

Figure 82. Green boxed example dot with measured centroid and metric radius (left), filtered image intensity at the *t* coordinate of the centroid as a function of *s* position (right).

Despite the fact that many centroid measurements, such the red boxed dot, may not be negatively affected by errors in image segmentation the overall impact of image segmentation may be severe for several reasons. First, the discussion here uses the measurement of calibration target dots as example cases, but particle measurements use the same image segmentation, effectively doubling any effect on final measurements. Second, in these examples both the red and blue boxed dot were included in the volumetric calibration. As discussed in the assessment of centroid error inherent to the calibration polynomial, any error in the blue dot would have effects throughout the calibration, therefore, the calibration in the region of the red dot could be degraded despite a high-quality measurement of the red dot centroid. It should be additionally noted that errors resulting from the image segmentation as shown here are not directly included in the calibration error discussion of the previous subsection but do result in degraded volumetric calibration. Specifically, those calibration errors were measured with respect to the positions defined in the calibration by the measured centroids. Therefore, in the context of calibration, error from image segmentation results in an error in the defined relationship to real space, though given the use of a single polynomial for all dots at all depths, these two sources of error are closely linked.

Though the differences in segmentation shown in this subsection are a result of vignetting, other image artifacts likely also affect segmentation. In future work, if a more advanced image segmentation scheme was implemented which was assessed to improve in-plane measurements those results could be compared to the current work to measure the contribution of image segmentation to centroid measurement error.

G. Error propagation and effects

This section examines how errors in the (*u*,*v*,*s*,*t*) measurements propagate through to the 3D particle measurements using the method of synthetic error generation described at the beginning of this chapter. Several variations of error addition, listed in Table 7, are considered in the following subsections to examine variables of interest based on suspected error distributions which may exist in the system.

Table 7. (*u*,*v*,*s*,*t*) error variations.

Error variation	Description
Uniform random error	Uniform random distribution of noise added to each (*s*,*t*) for a range of maximum values
Direction dependent error	Increased error in the *t* direction as compared to the *s* direction for a range of maximum values
Spatial radially increasing error	Error magnitude scaled with (*s*,*t*) coordinate
Angular radially increasing error	Error magnitude scaled with (*u*,*v*) coordinate
Depth dependent error	Uniform random error over an extended depth range

i. Uniform random error

A uniform random distribution of errors was added to the (*s*,*t*) coordinates and varied noise levels were examined with maximum errors ranging from 10^{-8} to 2 pixels to represent a range of noise from negligible (near machine precision) to larger than the largest reasonably expected errors in centroid measurements. 50 different logarithmically spaced noise levels within this range each with 10000 simulated points were examined.

Figure 83 shows the effect of these varied levels of noise on the error in (*x*,*y*,*z*) position. On the left is a plot of the average error in (*x*,*y*,*z*) as a function of the noise in the (*s*,*t*) coordinates, demonstrating a logarithmic relationship between error in (*s*,*t*) and (*x*,*y*,*z*). At very small noise levels the error reaches an asymptote at approximately 2 nm in the z direction and 3.3 nm in the in-plane directions indicating the level of the inherent error resulting from the least squares fit used to create the calibration. Based on the linear region of this plot, relationships between noise and position error in each dimension can be determined as,

$$e_x = 0.0053n^{0.9857}\,, \tag{18}$$

$$e_y = 0.0054n^{0.9850}\,, \tag{19}$$

$$e_z = 0.1088n^{0.9848}\,, \tag{20}$$

where *e* is the error in the subscripted dimension and *n* is the noise in pixels. These equations show that the relationships in the in-plane dimensions are very similar and the expected larger error in the *z* dimension. All dimensions show a nearly linear relationship as indicated by the exponent on the noise value. From Equation (20), it appears that approximately 1 pixel of error in the measured (*s*,*t*) positions corresponds to the depth error observed experimentally.

Similarly on the right of Figure 83, is a plot of the standard deviation of error in (*x*,*y*,*z*) as a function of the noise in the (*s*,*t*) coordinates demonstrating similar trends, though the difference in standard deviation between the in-plane and depth direction is more significant and at the smallest noise levels the standard deviation is larger in the in-plane directions. Considering the small magnitude of the error values for noise levels of less than approximately 10^{-5} pixels, it is hypothesized that the difference in the in-plane and depth direction standard deviations is the result of a numerical limitation rather than a meaningful measurement characteristic.

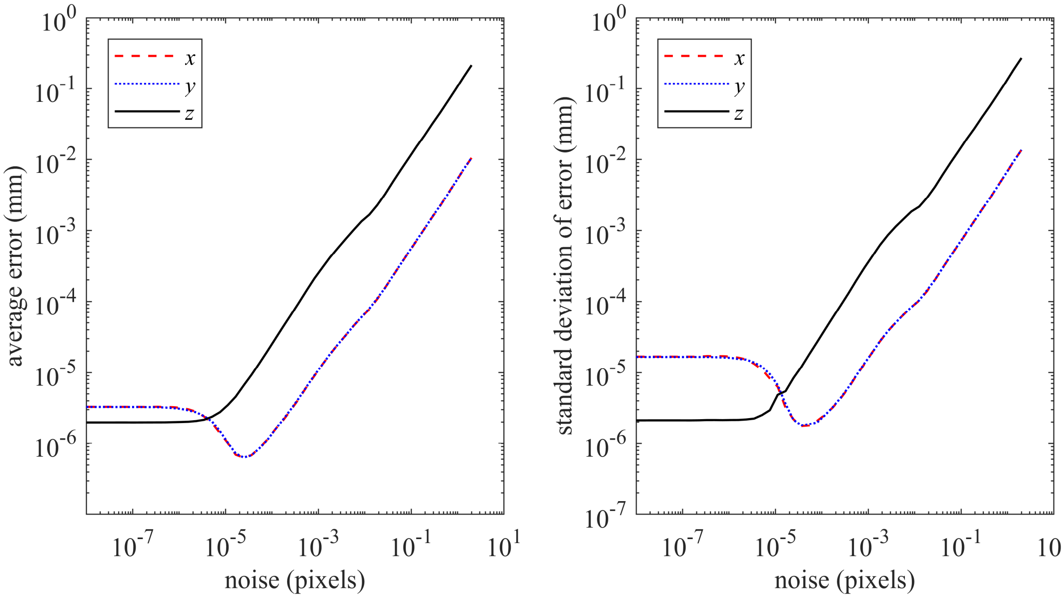

Figure 83. Average and standard deviation of error in (*x*,*y*,*z*) position as a function of noise addition to (*s*,*t*) positions.

ii. Direction dependent error

The error propagation analysis in the previous subsection considered statistically equal amounts of added noise in the *s* and *t* (horizontal and vertical) directions as this is the expected noise present in the measurement of spherical particles. It is expected that in some cases, such as the large aspect ratio particles examined in Chapter VI Section C Subsection i, that the error in the direction of elongation is more significant due to the large aspect ratio and segmentation effects. To assess this, a similar noise addition procedure was conducted as above, with noise of five times the magnitude added in the *t* direction as compared to the *s* direction reflecting higher uncertainty in the vertical than horizontal direction. For clarity, in the following discussion and figure the noise levels noted are those in the *s* direction. Figure 84 shows the resulting average and standard deviations of error as a function of noise for this case. These results show similar trends as the equal noise case, but larger magnitudes of error in all directions. The errors do appear to reach a similar asymptote as in the equal noise case, substantiating that this is indeed a numerical limit of the least squares fit. The logarithmic relationships between noise and position error are in this case,

$$e_x = 0.0150n^{1.0063}, \tag{21}$$

$$e_y = 0.0266n^{1.0115}, \tag{22}$$

$$e_z = 0.4925n^{1.0193}. \tag{23}$$

Comparison of these equations to Equations (18) - (20) shows the propagated error in all dimensions was significantly affected by changes in only the added noise in *t*, a result of the single polynomial function which couples the coordinates in all dimensions. Considering that these relationships all remain nearly linear, examination of the leading coefficient becomes of primary interest. Predictably, the in-plane dimensions show more separation in error magnitude as a result of separation in added noise. The *y* coefficient is approximately 4.9 times the value in the equal noise case, a logical result indicating a direct relationship between added noise and error when all other variables are held constant. The *x* coefficient however, is approximately 2.8 times the value in the equal noise case, again logical that the coupled nature of the polynomial results in errors in all object space dimensions as a result of differences in noise in a single image space centroid dimension. The change in the depth direction is more complex; the *z* coefficient is approximately 4.5 times the value in the equal noise case. This indicates that when the measurements in one of the in-plane dimensions is significantly less reliable, that noise level overwhelms the measurement error and becomes the primary controller of depth error. These dimensionally coupled error effects motivate further investigation of the effects of different calibration configurations, specifically the creation of independent calibrations for the each in-plane dimension or consideration of different calibration functions for different perspective views.

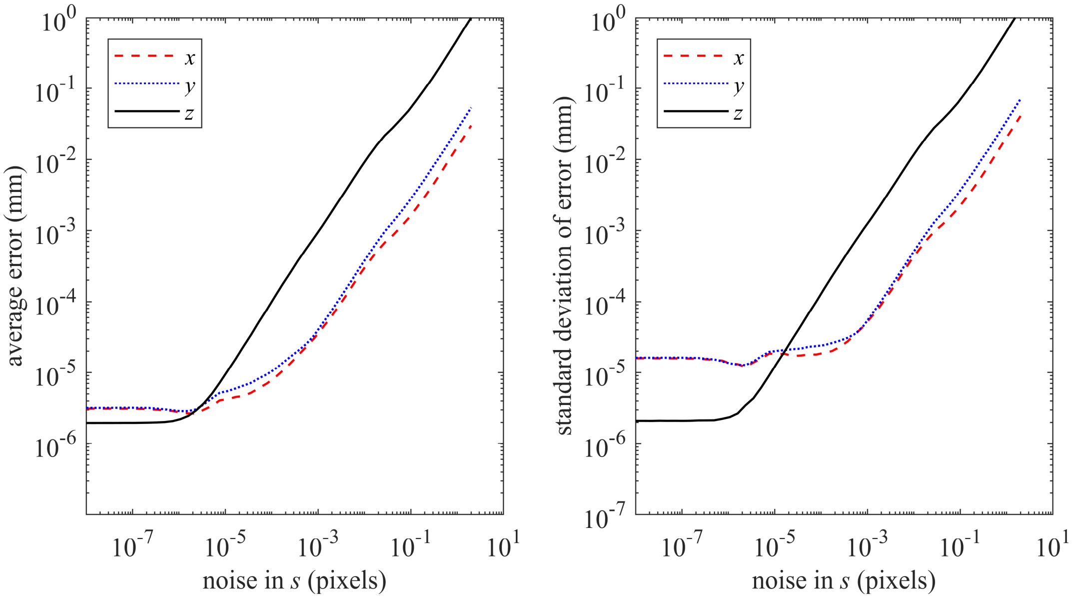

Figure 84. Average and standard deviation of error in (*x*,*y*,*z*) position as a function of noise addition to (*s*,*t*) positions when the added noise in the *t* direction is 5x that in the *s* direction.

iii. Spatial radially increasing error

To consider the effects of error increasing radially at the microlens plane, 1000 randomly located points were simulated and, errors were added based on the spatial position of each particle in a given views as,

$$s_{error} = s + \left(x / x_{\max} \right) p , \tag{24}$$

where s is the original horizontal microlens coordinate of the particle in the view of interest, x is the horizontal spatial coordinate of the particle, x_{max} is the maximum horizontal spatial coordinate in the volume, p is a constant value equal to one pixel of error, and s_{error} is the resulting error added horizontal microlens coordinate of the particle in the view of interest. A similar procedure was executed to add error in the vertical direction. This gives an error distribution as might be expected to result from the difference in the view of the aperture from different positions across the microlens array. Figure 85 displays the resulting errors projected to the (*x*,*y*) plane where color and scatter size indicates the magnitude of the measured depth error for each particle. A distinct increase in depth error with increasing distance from the center of the (*x*,*y*) plane is evident, however, is should be noted that the magnitudes of these errors even at the edges are on the order of 10 nm, suggesting that radially increasing error at the microlens plane does not have a significant impact on the overall error measurement.

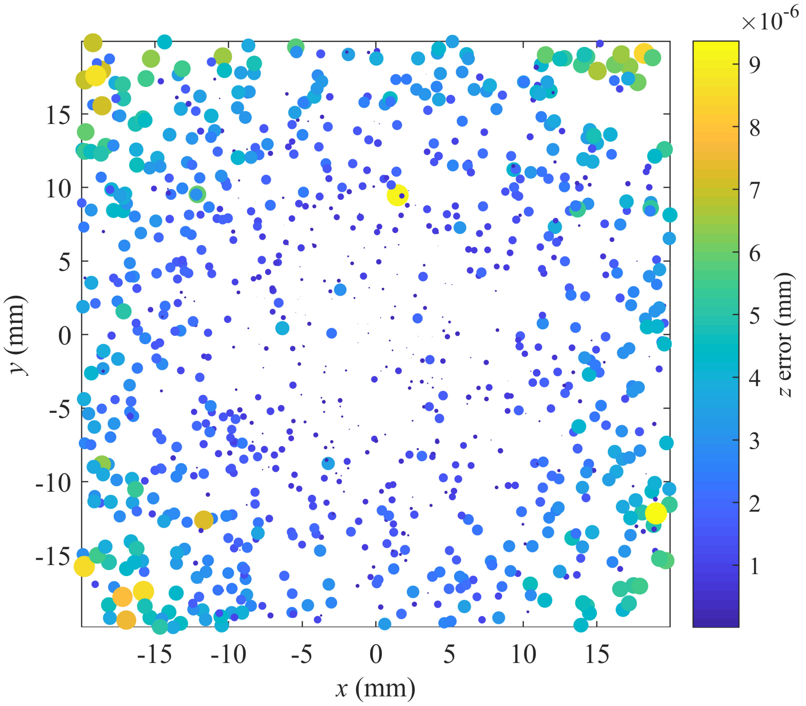

Figure 85. Depth error distribution resulting from (*s*,*t*) dependent radially increasing error.

iv. Angular radially increasing error

To consider the effects of error increasing radially from the center of the main lens aperture, 1000 randomly located points were simulated and errors were added based on the angular position of each particle in a given view as,

$$s_{error} = s + \left(u / u_{\max} \right) p \, , \qquad (25)$$

where s is the original horizontal microlens coordinate of the particle in the view of interest, u is the horizontal angular coordinate of the view of interest, u_{max} is the maximum horizontal angular coordinate within the aperture, p is a constant value equal to one pixel of error, and s_{error} is the resulting error added horizontal microlens coordinate of the particle in the view of interest. Again, a similar procedure was executed to add error in the vertical direction. Figure 86 displays an isometric view of the resulting depth error indicated by color and scatter size. Figure 87 displays a 2D view of the volume collapsed in the y direction which more clearly illustrates the increase in depth error that is present with increasing distance from the camera.

This is a logical result since the effect of a given angular displacement also increases with distance from the camera due to the decreased spatial sampling rate as shown in Figure 88. This schematic demonstrates the trapezoidal region of object space that is imaged. All depths contained in a perspective view are represented with the same number of pixels, essentially, a perspective view is a representation of the entire imaged volume projected to the focal plane. Therefore, as distance from the camera increases, so does the physical region represented by each pixel, indicated in Figure 88 at two different depths by the red arrows. These angular errors result in depth errors on the order of 1 mm, indicating that if this type of radial distortion is present, it could have a significant impact on measurement error.

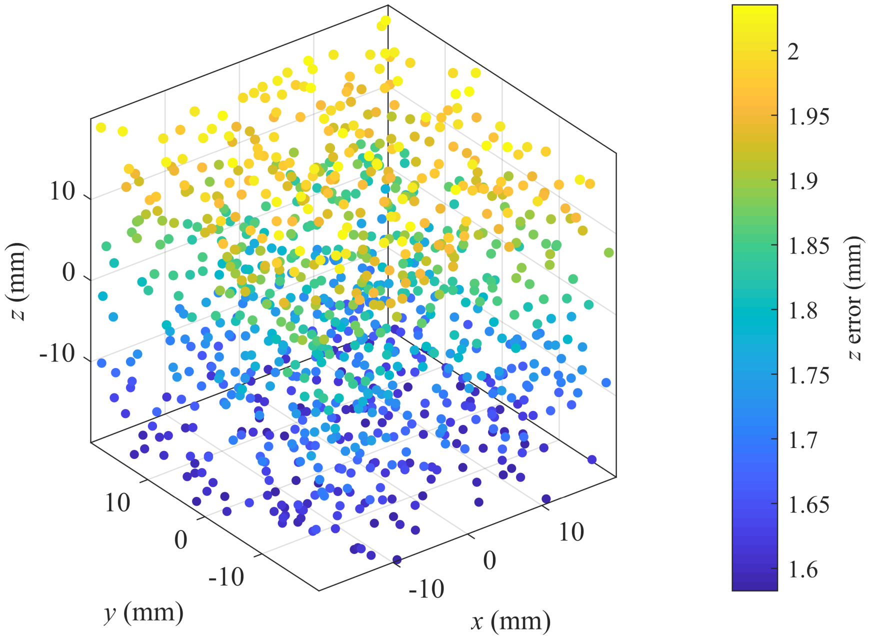

Figure 86. Isometric view of depth error distribution resulting from (*u*,*v*) dependent radially increasing error.

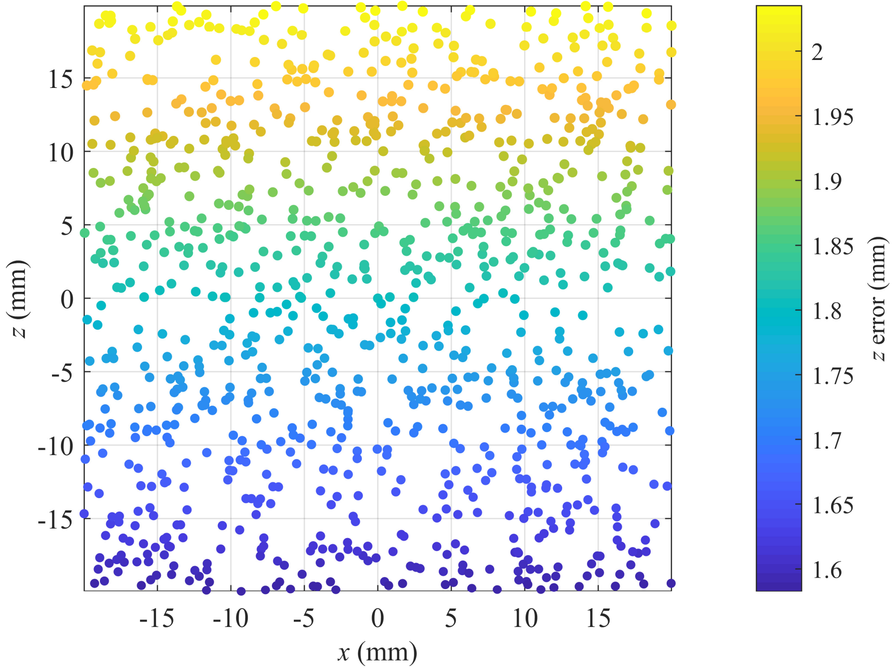

Figure 87. 2D view of depth error distribution resulting from (*u*,*v*) dependent radially increasing error.

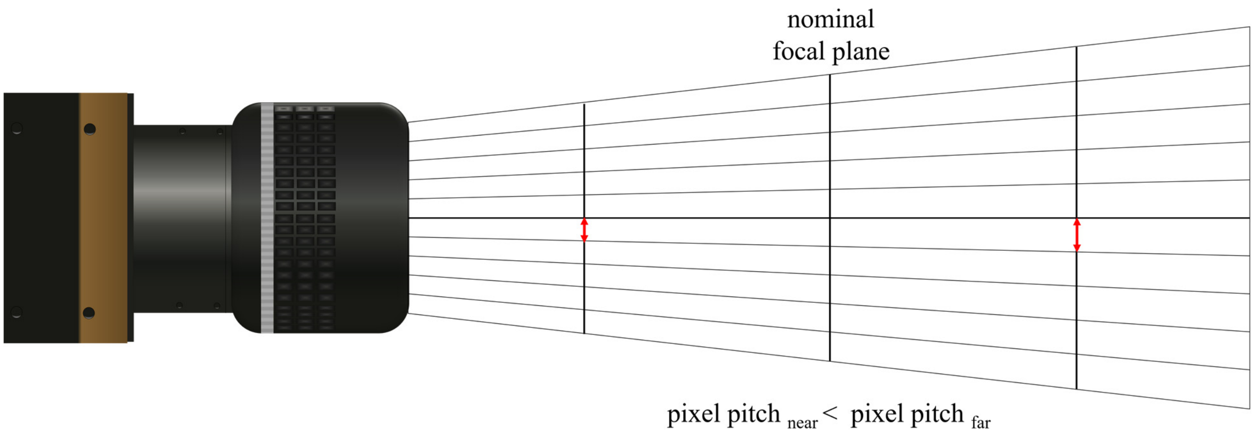

Figure 88. Schematic depiction of the depth dependent change in sampling rate.

v. *Depth dependent error*

The effect of particle depth on error magnitude is also of interest given the observed impact of the depth of field in experimental assessments. It should be noted that this synthetically generated calibration and uniform noise addition is not technically affected by DOF, however, any effects at extreme depths identified here would be compounded on DOF limitations. Figure 89 displays an isometric view of the resulting depth errors when a uniform random distribution of noise with a maximum of 1 pixel, was added to the (s,t) coordinates. This noise addition is equivalent to a single noise level of those examined in Subsection i above except that particles in a larger volume of $z = \pm 100$ mm are included. From this plot it is evident that the error magnitudes increase at distances farther from the camera ($+z$) and decrease slightly at distances closer to the camera. Figure 90 displays a 2D view collapsed along the y direction of the same results to more clearly demonstrate the depth dependency. This is likely the result of the relative available parallax and spatial sampling rate at a given depth. Objects closer to the camera are measured from a larger effective range of angles than objects farther from the camera and again pixel size increases with distance from the camera. This indicates that measurements from a larger range of angles and at a higher spatial sampling rate result in smaller measurement error.

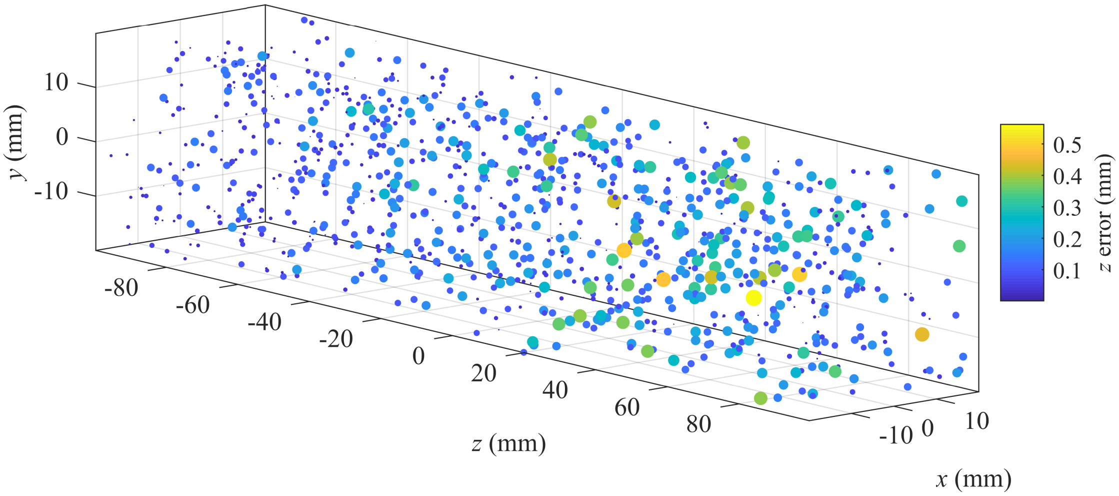

Figure 89. Isometric view of depth error distribution resulting from uniform random noise in an extended depth volume.

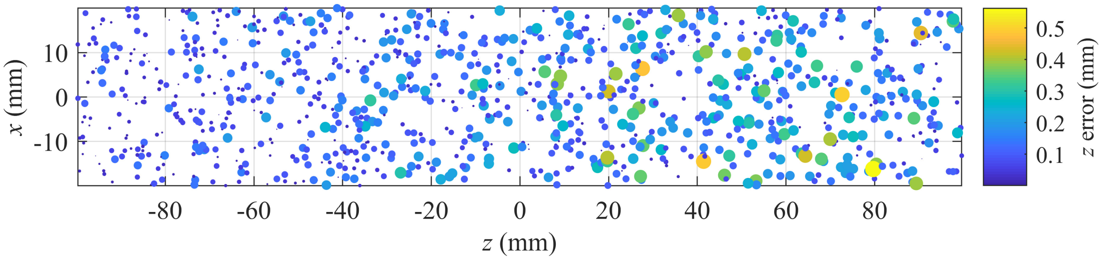

Figure 90. 2D view of depth error distribution resulting from uniform random noise in an extended depth volume.

H. Summary

The propagation of error from (*u*,*v*,*s*,*t*) light field coordinates to the resulting 3D particle position measurements is examined by consideration of various systematic and random additions of error. This provides an expected magnitude of error that would result in the measured experimental errors. The mechanisms contributing to this error are then considered to determine the relative impact of each. In general, it appears that the choice of image segmentation method introduces the most error and may be improved by the use of a more advanced method.

VIII. Experimental applications

This chapter examines the application of the perspective shift algorithm to two experiments to provide context for the practical applications and limitations of the algorithms developed in this work. Unlike the uncertainty characterization experiments discussed in the previous chapters, the particle positions measured are not known a-priori, therefore statistical and qualitative assessments of algorithmic quality are made based on known characteristics of the experiments. In the first experiment, the secondary droplet field created by the impact of a drop of water on a thin film of water is measured. In the second, the fragment field created by a lab-scale detonator is examined.

A. Drop impact

Example results from the previous analysis of the drop impact experiment using refocusing are shown in Figure 15 and provide a general idea of the experimental configuration. The secondary droplet field, or splash, is a well characterized and controllable phenomenon and therefore provides a reliable test case for the developing optical diagnostics. In this experiment, the 3D size, location, and three-component velocity of the secondary droplets are quantified. Overall error is estimated based on expected flow symmetry about the point of impact and statistical measurements of location and velocity are compared to published values for a similar drop impact configuration studied using DIH [58]. Displacements in the in-plane direction were assumed to have negligible uncertainty and any additional scatter in the depth direction was assumed to be measurement error. The remainder of this section demonstrates the application of the perspective shift algorithm to the measurement of these droplets and compares the results to those previously achieved using refocusing and DIH as appropriate. Details of the experimental configuration as well as in depth results of the refocusing based implementation can be found in Munz [84].

Two parameters used to characterize the experimental configurations examined in this study and allow comparison to other similar experiments are the impact Weber number, *We*, and non-dimensional time, τ. The Weber number is a non-dimensional parameter which relates the inertia to the surface tension of a fluid to describe a gas-liquid interface and is defined as,

$$We = \frac{\rho v_0^2 d_0}{\sigma}. \tag{26}$$

Non-dimensional time, used here as a normalization of the time since drop impact, is defined as,

$$\tau = \frac{t v_0}{d_0}. \tag{27}$$

In these equations and the following discussion, ρ is the drop density assumed to be 1000 kg/m^3, σ is the surface tension, t is the time since impact, v_0 is the impact velocity, and d_0 is the initial drop diameter. Due to the slow rate of droplet generation (about 0.06 Hz) it is assumed that each drop impact occurred on a quiescent surface. Here, the same plenoptic data set that was examined in Hall et al. [13] using the refocusing processing method described in Chapter IV is reexamined using the perspective shift based method developed and examined in Chapters V and VI. The results of the perspective shift based processing are compared to those previously published results. In examination of these measurements it should be noted that while the two plenoptic methods examine the exact same data set, the DIH results consider a similar data set, however there is variation in some experimental parameters between the two implementations.

In each experiment the initial height from which the drop was released as well as the delay time at which images were captured was varied resulting in data sets at several different experimental conditions. For brevity, a single similar condition from each is examined here. The parameters of this condition for each diagnostic implementation are presented in Table 8 along with some of the resulting measurements. Given that the drop heights in both experiments are similar, varying by only approximately 0.6 percent, the initial conditions which are measured directly before impact are expected to match as well. Examination of the measured values of initial diameter and velocity shows better agreement of the plenoptic results with DIH when processed using perspective shift than using refocusing. These improved measurements of initial conditions also result in the calculation of a Weber number closer to that calculated in the DIH data set. The mean measured secondary droplet diameters, $\overline{d}$, provide less definitive insight, because the delay time at which the plenoptic data set was collected is larger than the DIH data set. The secondary diameter measured using plenoptic perspective shift was larger than that measured by DIH which agrees with the relationship established by Cossali et al. that $\overline{d}/d_0 = q\tau^n$, where q and n are constants [85]. Despite the agreement in this general trend, since the values of these constants used in literature are not widely agreed upon, it is difficult to define how much the secondary droplet diameters are expected to vary with the non-dimensionalized time.

Table 8. Drop impact parameters and results.

	DIH	Plenoptic refocusing	Plenoptic perspective
Drop height (mm)	905	900	900
Initial diameter (mm)	3.18	3.29	3.19
Initial velocity (m/s)	4.05	4.24	4.09
Weber number	722	783	706
Mean secondary diameter (mm) (at τ)	0.151 (1.7)	0.152 (2.6)	0.227 (2.6)
σ_x	0.224	0.682	0.879
σ_z	1.036	0.702	1.014

Figure 91 shows histograms of the secondary droplet diameters measured using the previous refocusing implementation as well as the perspective shift based method. Comparison of the general shape of the histograms shows a more gradual decrease in the number of measurements at small diameters in the perspective shift based results as compared to the clipped shape in the refocusing case. The gradual decrease shows better agreement with the comparable DIH results and generally expected diameter distributions in literature. The minimum diameters measured using the perspective shift are also smaller than in the refocusing processing suggesting that smaller particles can be identified in perspective views that might be too blurry to identify using refocusing. A larger overall number of particles were also identified using the perspective shift method than refocusing; in this data set approximately 27% more particles were measured. This increase is likely most affected by the measurements of those smaller diameter particles.

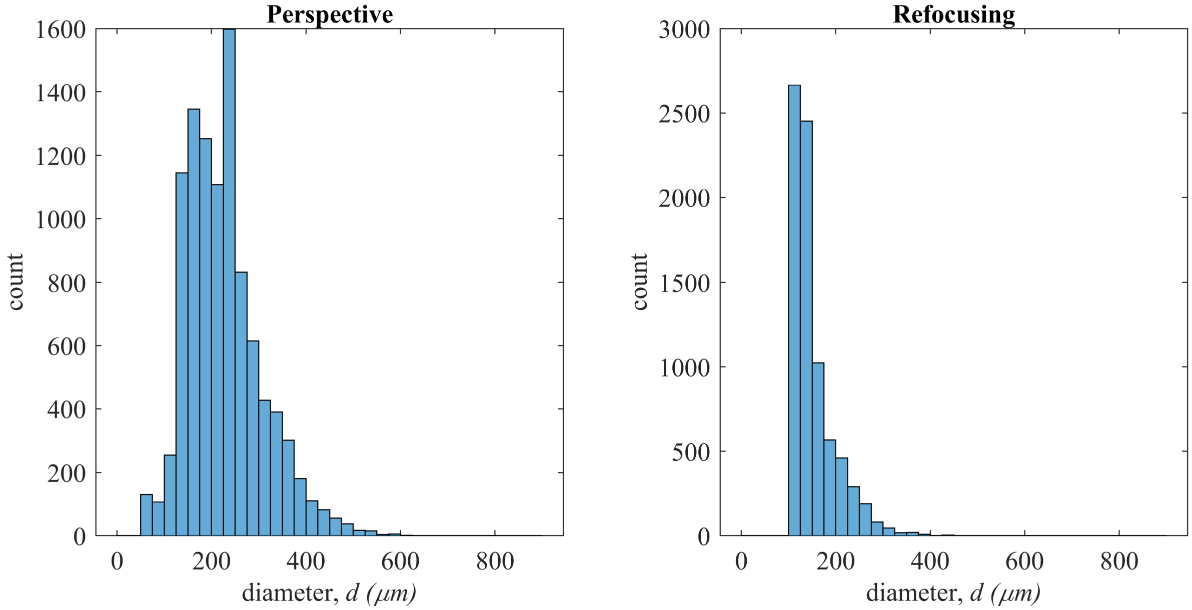

Figure 91. Histograms of measured secondary droplet diameters measured with perspective shift (left) and refocusing (right).

Figure 92 displays the x and z displacement components of the measured secondary droplets at this condition, again results are shown for both refocusing and perspective shifting.

Only 10% of the results are shown in these plots for clarity. Linear fits of the *x* and *z* displacements are also plotted in this figure. The agreement of these two linear fits shows that the mean measured displacements in the *x* and *z* directions are similar as expected due to flow symmetry, though the refocusing fits show slightly better agreement than the perspective results in this configuration. Model error is defined as the difference between the measured displacement component and the displacement component predicted by the linear fit at the measured position and is also given in Table 8 which shows larger average error in the perspective shift results in both dimensions, but still similar to the DIH results in the *z* direction. In general, the displacement measurements do not vary dramatically between the two methods.

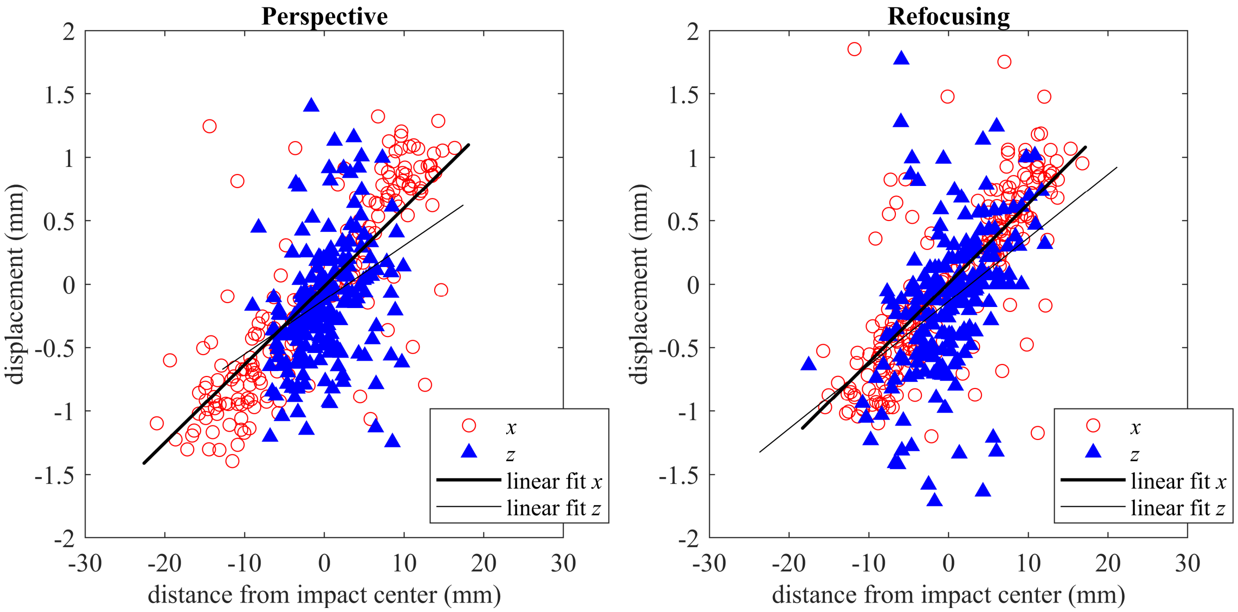

Figure 92. Scatter plots of particle displacement as a function of distance from impact center measured with perspective shift (left) and refocusing (right).

B. Detonator

As mentioned previously, this dissertation work is motivated by the need to instantaneously measure explosively generated fragment fields in 3D. For nearly a century, explosion analysis has been performed through assessment of pressure and acceleration measurements as well as examination of post explosion fragment locations, however, the resolution and accuracy of these techniques are limited [1–3]. More recently optical methods such as high-speed video and digital holography have been used to improve the information that can be obtained about these fragment fields [12,86].

Here, the fragment field from a lab-scale detonator (RP-80 from Teledyne RISI) is examined as an example of this type of application. Photos of the experimental configuration of the detonator testing are shown in Figure 93. The tests were conducted in a protective plexiglass box and backlit using a pulsed diode and diffuser. Plenoptic and high-speed images were captured simultaneously, both cameras are visible in the photos and were mounted to view the explosion at a 90 degree angle.

Figure 93. Photos demonstrating the lab-scale detonation experimental setup.

The top row in Figure 94 shows selected frames from a high-speed video of the same type of detonation demonstrating the development of the detonation and fragment dispersal. Here, rapid expansion of the detonating explosive causes the surrounding metal case to stretch until failure leading to the formation of sharp metal fragments traveling near one kilometer per second [86]. Accurate knowledge of the 3D location, size, shape, and velocity of these fragments is critical to understand and mitigate hazards from such explosives [87]. The images in the bottom row of

Figure 94 are two perspective shifted images created from a single instantaneous raw plenoptic image of the same detonator as shown in the top row. The circled fragments highlight the difference in relative position of fragments in the two views.

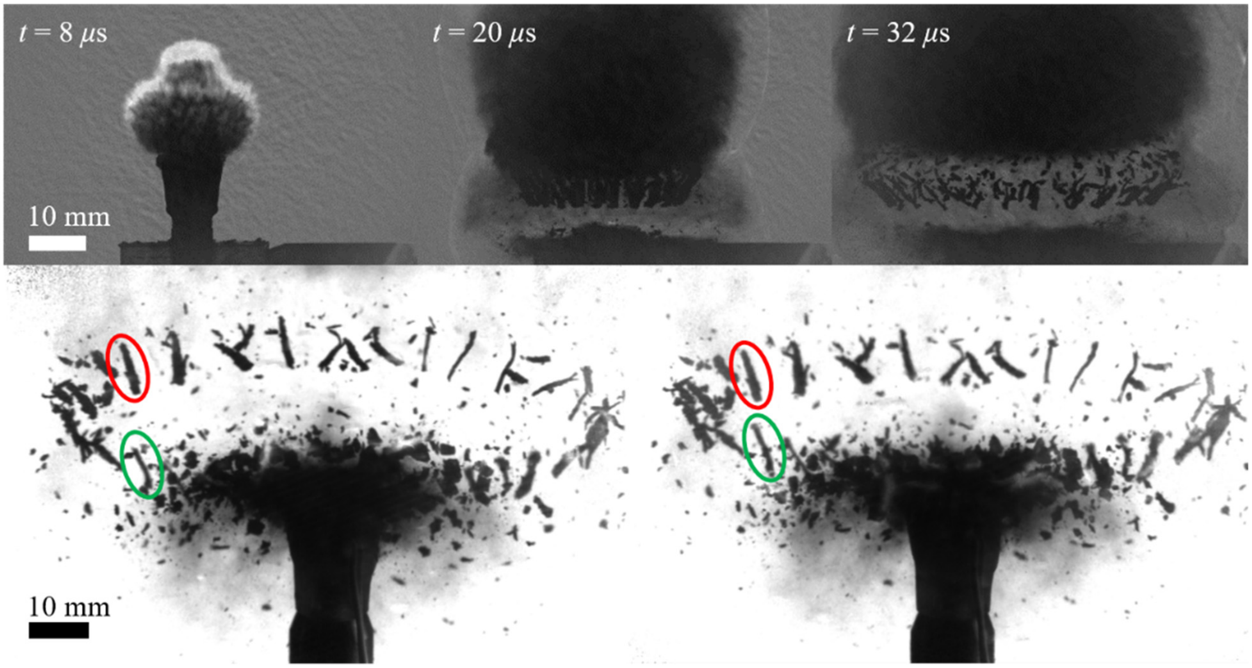

Figure 94. Selected frames from high-speed video of a lab scale detonation (top) and vertically shifted perspective views created from a simultaneously captured plenoptic image (bottom).

Figure 95 displays the results of applying the perspective shift method developed here to this detonator application. The bottom left shows a center perspective view which is overlaid with measured fragment shapes. Color indicates fragment depth, where red is farther from the camera and blue is closer to the camera. To the right of this is a reconstructed orthogonal side view while a top-down view is shown above. Finally, the top-right shows an isometric view of the measured 3D fragment locations. Grayscale as well as the scatter size indicates the measured fragment image area.

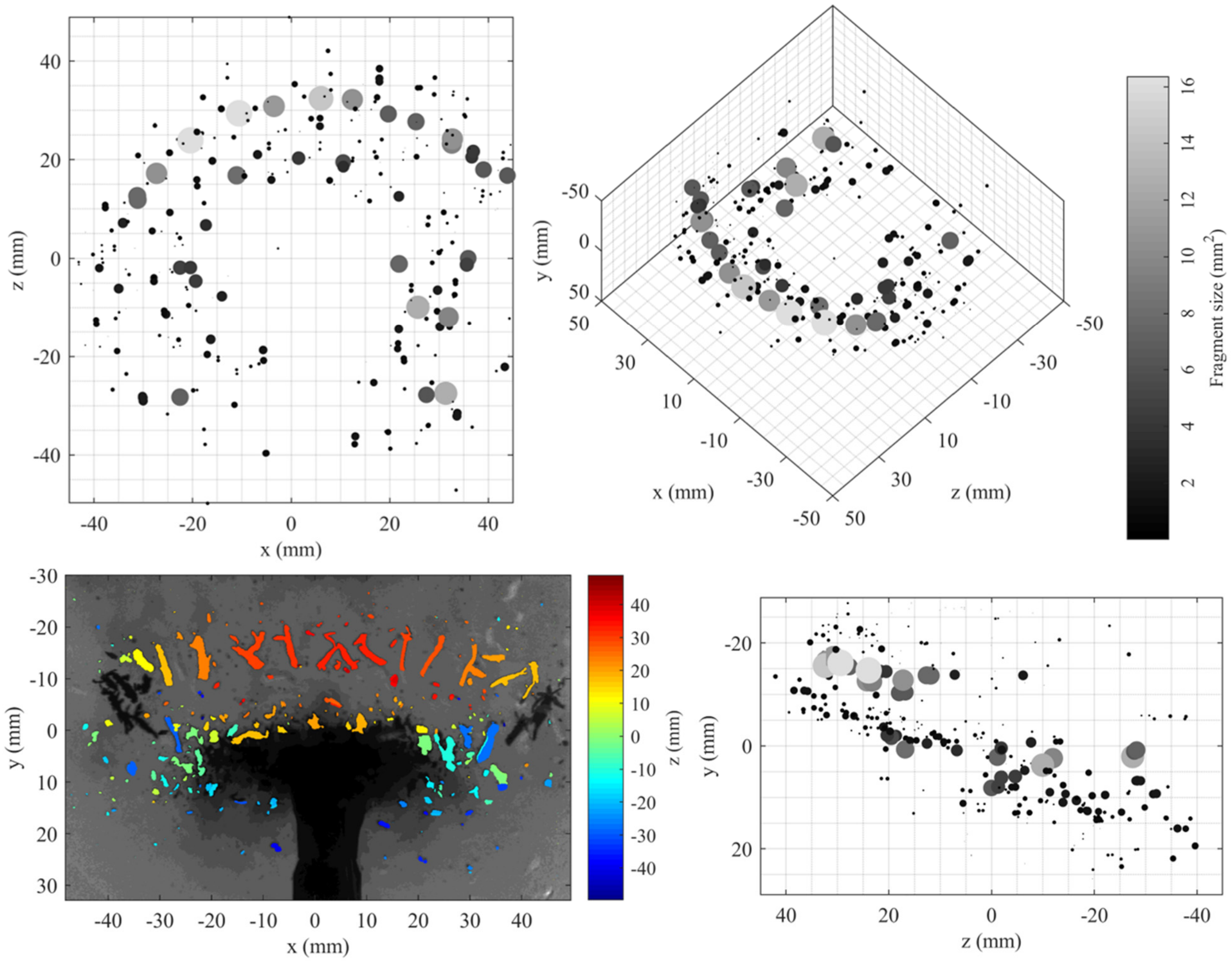

Figure 95. Plenoptic measurements of the lab-scale fragmenting explosive shown in Figure 8. Center perspective view, overlaid with measured fragment shapes colored by optical depth, z (bottom left). Reconstructed side (bottom right), top-down (top left), and isometric (top right) views showing the measured 3D fragment locations. Grayscale intensity and scatter sizes are proportional the measured fragment image area.

Though the detailed fragment locations and shape characteristics are not known *a priori*, a qualitative assessment of the effectiveness of this measurement can be made. First, as expected due to the cylindrical symmetry of the detonator, fragments are measured in an approximately circular ring pattern at this instant in time. Second, in this experiment, the detonator was placed at an angle tilted slightly towards the camera; therefore, it is known that the fragments in the upper portion of the ring are located farther from the camera compared those in the lower portion of the ring. The depth map shows agreement with this orientation. Additional validation is presented in comparison of scatter plot of the orthogonal side view (bottom right) with Figure 96, which is the frame of the simultaneously captured high speed video corresponding to the time the plenoptic image was captured. This scatter plot is oriented to display the scene from the same angle at which the high speed camera was physically located and demonstrates the ability of the plenoptic camera to provide a valid representation of a scene from a position perpendicular to the physical camera position. This example indicates that a plenoptic camera combined with the data processing algorithms developed here can resolve 3D fragment properties from lab-scale explosive events.

Figure 96. Frame of simultaneously captured high speed video of detonator explosion.

C. Summary

The analysis of these two experimental applications has shown the viability of the measurement of the motivating application of explosion analysis in this work by the use of perspective shifted plenoptic images. In the drop impact experiment, relative agreement between the plenoptic perspective and previously implemented DIH results for a similar experiment were shown. In the lab scale detonator experiment, the expected fragment distribution and morphology was qualitatively verified.

IX. Conclusions and contributions

The major takeaways of this work can be broken into four categories: volumetric calibration, 3D particle location algorithm development, uncertainty characterization, and application viability. This chapter will discuss the relevant conclusions which can be drawn concerning each of these topics, the contributions resulting from each, and the opportunities for future work which have been identified in related areas.

This dissertation detailed the development of two methods for the volumetric calibration of a plenoptic camera, each based on a 3D polynomial mapping function created using information gathered from a known set of calibration target images as well as a thin lens based calibration. The first was the Volumetric Dewarping method in which a polynomial mapping is used to correct an uncalibrated volume, and the second was the Direct Light Field Calibration method in which a polynomial mapping is used to create a calibrated volume directly from raw plenoptic data. An experiment was designed to test the reconstruction accuracy achievable using these methods in which images of a dot card were captured at a variety of angles. The results of this experimental comparison demonstrate a similar improvement in reconstruction precision using either of the volumetric methods and a larger improvement in accuracy using Direct Light Field Calibration. In the calibrated volumes created using each method, the depth locations of individual dots were measured on average to within approximately 0.25 mm of their actual known locations, representing a 0.5% error in the depth direction based on the reconstructed volume size. The errors in the *x* and *y* directions are approximately an order of magnitude smaller. In comparison, errors determined using the simple thin lens calibration averaged 0.51 mm in the depth direction, with some errors as large as 6.7 mm. Though the improvement in depth accuracy and precision achieved by application of these polynomial mapping based calibration methods is significant, further improvement may be possible through a detailed study of the order and organization of the mapping functions used in the volumetric calibration and how these choices affect the resulting calibration error.

Two methods of 3D particle location were developed in this work by exploitation of the refocusing and perspective shift capabilities of plenoptic imaging. First, refocused images were used by creation of a dense focal stack that could be post processed similarly to DIH data sets to determine particle location based on metrics of minimum intensity and maximum edge sharpness. This was the first approach in the attempt to determine 3D particle positions due to the natural volumetric representation of a scene created by a focal stack. Second, perspective shifted images were used to determine 3D position based on the apparent position of a particle in a variety of different subaperture images. Due to the significantly smaller computational requirements of the creation of perspective shifted as compared to refocused images this implementation resulted in a reduction of the total processing time for determination of particle positions by approximately two orders of magnitude. The perspective views were combined with the creation of a small portion of a single refocused image at the measured (x,y,z) position to determine the in-plane size and shape of a particle increasing the flexibility and application space of the technique. This work in the determination of in-plane characteristics also resulted in identification of avenues of related future work in image segmentation. As preliminary analysis has shown that small differences in thresholding parameters can have a significant impact on measured particle size suggesting that advanced image segmentation schemes could improve size and shape measurements. A second area of future work involves the measurement of extended objects as the current implementation defines an object at a single depth location, however, for larger particles or fragments, the raw light field data likely contains enough information to determine a 3D morphology of these objects.

The uncertainty of both methods was assessed using a static particle field in which particles were translated known distances to provide a well characterized data set. The perspective shift based approach allowed the removal of individual low-quality measurements which, in conjunction with the determination of particle location based on centroid rather than sharpness, resulted in reduced uncertainty over an extended depth range. Average depth precision within 0.4 mm and accuracy within 0.1 mm was achieved over a range of 50 mm using the perspective shift algorithm. This is reduced from those achieved using refocusing of precision within 1.7 mm and accuracy within 0.2 mm. The in-plane size and shape uncertainty of the perspective shift method was also assessed, and diameter errors of less than 0.5 mm were achieved. Objects with diameters of at least 2 microlenses in object space showed diameter errors of less than 0.3 mm. The future work in improvement of in-plane measurements described above will also warrant further uncertainty characterization.

Additionally, several possible sources of these uncertainties were examined and the expected relative contributions of each was considered. The results indicated that although several mechanisms have contributions to measurement error, improvements in image segmentation would likely allow the most significant improvements in uncertainty. Therefore, exploration of an advanced image segmentation technique for application to the perspective shift method is suggested as future work. It was also determined that errors resulting from the volumetric calibration are small within the DOF but may have a more significant effect in experimental configurations where measurement of a volume outside the depth of field is desired. This again motivates future study into better understanding of and improvement of the volumetric calibration.

Finally, the viability of perspective shift based measurements for specific applications was examined. The measurement of a secondary water droplet field with the perspective shift algorithm showed similar results statistically to those previously obtained using the refocusing based method in particle location and velocity measurements. The perspective shift method was also able to achieve measurements of more particles than previously identified using refocusing due to improved measurements at small diameters. The measurement of the motivating application of explosively generated fragments was also demonstrated using the perspective shift algorithm. Results showed qualitative agreement with the expected shape of individual fragments as well as the expected circular fragment ring orientation. These experimental applications have also highlighted the scales to which single camera light field imaging can be successfully applied and provide examples of a niche of explosion analysis where plenoptic cameras can provide significant benefits.

It has been shown in this dissertation that the combination of light field imaging applied with a single plenoptic camera with 3D particle location routines developed based on available multi-view information shows promise for a variety of experimental applications. The uncertainty characterization achieved and algorithms developed in combination with application of a volumetric calibration allows quantitative measurements using a compact single camera imaging system. This emphasis on post-processing results in a simple and flexible experimental system allowing rapid setup and data collection. 3D particle location using a plenoptic camera is expected to be particularly useful for proof-of-concept and small-scale testing of new apparatuses and experimental configurations at reduced experimental costs and requirements.

References

1. B. Hopkinson, "A method of measuring the pressure produced in the detonation of high explosives or by the impact of bullets," Philos. Trans. R. Soc. London **213**, 437–456 (1914).
2. J. M. Brett, G. Yiannakopoulos, and P. J. Van Der Schaaf, "Time-resolved measurement of the deformation of submerged cylinders subjected to loading from a nearby explosion," Int. J. Impact Eng. **24**, 875–890 (2000).
3. G. Yiannakopoulos, "Accelerometer adaptor for measurements of metal plate response from a near field explosive detonation," Rev. Sci. Instrum. **68**, 3254–3255 (1997).
4. S. O. Shelley, *Vulneravility and Lethality Testing System (VALTS)* (1972).
5. R. Barnard and P. Nebolsine, "Fragment-field analysis testing system," in *Second Biennial AIAA Weapon System Effectiveness Conference* (2001), pp. 27–29.
6. K. Hoyer, M. Holzner, B. Lüthi, M. Guala, A. Liberzon, and W. Kinzelbach, "3D scanning particle tracking velocimetry," Exp. Fluids **39**, 923–934 (2005).
7. G. E. Elsinga, F. Scarano, B. Wieneke, and B. W. Van Oudheusden, "Tomographic particle image velocimetry," Exp. Fluids **41**, 933–947 (2006).
8. G. E. Elsinga, B. Wieneke, F. Scarano, and B. W. Van Oudheusden, "Assessment of Tomo-PIV for three-dimensional flows," 1–10 (2005).
9. J. Katz and J. Sheng, "Applications of holography in fluid mechanics and particle dynamics," Annu. Rev. Fluid Mech. **42**, 531–555 (2010).
10. K. D. Hinsch and S. F. Herrmann, "Holographic particle image velocimetry," Meas. Sci. Technol. **15**, (2004).

11. D. R. Guildenbecher, M. a Cooper, W. Gill, H. L. Stauffacher, M. S. Oliver, and T. W. Grasser, "Quantitative, three-dimensional imaging of aluminum drop combustion in solid propellant plumes via digital in-line holography.," Opt. Lett. **39**, 5126–9 (2014).

12. J. D. Yeager, P. R. Bowden, D. R. Guildenbecher, and J. D. Olles, "Characterization of hypervelocity metal fragments for explosive initiation," J. Appl. Phys. **122**, 1–9 (2017).

13. E. M. Hall, B. S. Thurow, and D. R. Guildenbecher, "Comparison of three-dimensional particle tracking and sizing using plenoptic imaging and digital in-line holography," Appl. Opt. **55**, 6410–6420 (2016).

14. R. Ng, M. Levoy, G. Duval, M. Horowitz, and P. Hanrahan, "Light field photography with a hand-held plenoptic camera," Stanford Tech Rep. CTSR 1–11 (2005).

15. G. Lippmann, "La photographie integrale," Comptes-Rendus, Acad. des Sci. **146**, 446–551 (1908).

16. E. Adelson and J. Bergen, "The plenoptic function and the elements of early vision," Comput. Model. Vis. Process. 3–20 (1991).

17. E. H. Adelson and J. Y. A. Wang, "Single lens stereo with a plenoptic camera," IEEE Trans. Pattern Anal. Mach. Intell. **14**, 99–106 (1992).

18. M. Levoy and P. Hanrahan, "Light field rendering," Proc. 23rd Annu. Conf. Comput. Graph. Interact. Tech. - SIGGRAPH '96 31–42 (1996).

19. L. McMillan and G. Bishop, "Plenoptic modeling: An image-based rendering system," Proc. 22nd Annu. Conf. Comput. Graph. Interact. Tech. **95**, 39–46 (1995).

20. R. Koch, M. Pollefeys, B. Heigl, L. Van Gool, and H. Niemann, "Calibration of hand-held camera sequences for plenoptic modeling," Comput. Vision, 1999. Proc. Seventh IEEE Int. Conf. **1**, 585–591 vol.1 (1999).

21. D. Dansereau and L. Bruton, "Gradient-Based Depth Estimation From 4D Light Fields," in *2004 IEEE International Symposium on Circuits and Systems (IEEE Cat. No.04CH37512)* (IEEE, 2004), pp. 4–7.

22. M. Levoy, "Light Fields and Computational Imaging," IEEE Comput. Soc. 46–55 (2006).

23. T. W. Fahringer, K. P. Lynch, and B. S. Thurow, "Volumetric particle image velocimetry with a single plenoptic camera," Meas. Sci. Technol. **26**, 115201 (2015).

24. K. C. Johnson, B. S. Thurow, T. Kim, G. Blois, and K. T. Christiansen, "Volumetric velocity measurements in the wake of a hemispherical roughness element," AIAA J. **55**, 2158–2173 (2017).

25. H. Chen and V. Sick, "Three-dimensional three-component air flow visualization in a steady-state engine flow bench using a plenoptic camera," SAE Int. J. Engines **10**, 625–635 (2017).

26. T. T. Truscott, J. Belden, R. Ni, J. Pendlebury, and B. McEwen, "Three-dimensional microscopic light field particle image velocimetry," Exp. Fluids **58**, 1–14 (2017).

27. S. Ostmann, H. Chaves, and C. Brücker, "3D path tracking of particles in a swirling flow using a light-field camera," 17th Int. Symp. Appl. Laser Tech. to Fluid Mech. 7–10 (2014).

28. C. Skupsch and C. Brücker, "Multiple-plane particle image velocimetry using a light-field camera," Opt. Express **21**, 1726–1740 (2013).

29. A. Bajpayee and A. H. Techet, "3D Particle Tracking Velocimetry (PTV) Using High Speed Light Field Imaging of focus particles x dx dy," in *10TH Internationnal Symposium on Particle Image Velocimetry -PIV13* (2013).

30. H. Chen, P. M. Lillo, and V. Sick, "Three-dimensional spray–flow interaction in a spark-ignition direct-injection engine," Int. J. Engine Res. **17**, 129–138 (2016).

31. H. Nien, J. A. . Fessler, and V. Sick, "Model-based image reconstruciton of chemiluminesence using a plenoptic 2.0 camera," IEEE Int. Conf. Image Process. 359–363 (2015).

32. J. N. Klemkowsky, T. W. Fahringer, C. J. Clifford, B. F. Bathel, and B. S. Thurow, "Plenoptic background oriented schlieren imaging," Meas. Sci. Technol. **28**, (2017).

33. P. M. Danehy, W. D. Hutchins, T. W. Fahringer, and B. S. Thurow, "A Plenoptic Multi-Color Imaging Pyrometer," 55th AIAA Aerosp. Sci. Meet. 1–7 (2017).

34. J. Bolan, E. Hall, C. Clifford, and B. Thurow, "Light-field imaging toolkit," SoftwareX **5**, 101–106 (2016).

35. M. W. Tao, S. Hadap, J. Malik, and R. Ramamoorthi, "Depth from combining defocus and correspondence using light-field cameras," Proc. IEEE Int. Conf. Comput. Vis. 673–680 (2013).

36. T. C. Wang, A. A. Efros, and R. Ramamoorthi, "Occlusion-aware depth estimation using light-field cameras," Proc. IEEE Int. Conf. Comput. Vis. **2015 Inter**, 3487–3495 (2015).

37. R. J. Adrian and J. Westerweel, *Particle Image Velocimetry* (Cambridge University Press, 2011).

38. M. Raffel, C. Willert, S. Wereley, and J. Kompenhans, *Particle Image Velocimetry: A Practical Guide*, Second Edi (Springer-Verlag, 2007).

39. H. Kim, J. Westerweel, and G. E. Elsinga, "Comparison of Tomo-PIV and 3D-PTV for microfluidic flows," Meas. Sci. Technol. **24**, (2013).

40. F. Pereira, H. Stüer, E. C. Graft, and M. Gharib, "Two-frame 3D particle tracking," Meas. Sci. Technol. **17**, 1680–1692 (2006).

41. E. A. Cowen and S. G. Monismith, "A hybrid digital particle tracking velocimetry

technique," Exp. Fluids **22**, 199–211 (1997).

42. B. Wieneke, "Iterative reconstruction of volumetric particle distribution," Meas. Sci. Technol. **24**, (2013).

43. D. Bröder and M. Sommerfeld, "A PIV / PTV system for analysing turbulent bubbly flows," Unknown 1–10 (2000).

44. W. Zhang, Y. Wang, and S. J. Lee, "Simultaneous PIV and PTV measurements of wind and sand particle velocities," Exp. Fluids **45**, 241–256 (2008).

45. A. Stitou and M. L. Riethmuller, "Extension of PIV to super resolution using Adel Stitou and M L Riethmuller," Meas. Sci. Technol. **12**, 1398–1403 (2001).

46. Y. A. Hassan and R. E. Canaan, "Full-field bubbly flow velocity measurements using a multiframe particle tracking technique," Exp. Fluids **12**, 49–60 (1991).

47. K. Ohmi and H. Y. Li, "Particle-tracking velocimetry with new algorithms," Meas. Sci. Technol. **11**, 603–616 (2000).

48. S. P. Lloyd, "Least Squares Quantization in PCM," **I**, 129–137 (1982).

49. D. Arthur and S. Vassilvitskii, "K-means++: the advantages of careful seeding," Proc. Eighteenth Annu. ACM-SIAM Symp. Discret. Algorithms **8**, 1027–1025 (2007).

50. A. Vattani, "k-means Requires Exponentially Many Iterations Even in the Plane," Discret. Comput. Geom. **45**, 596–616 (2011).

51. H. G. Maas, A. Gruen, and D. Papantoniou, "Particle tracking velocimetry in 3-dimensional flows. 1. Photogrammetric determination of partacle coordinates," Exp. Fluids **15**, 133–146 (1993).

52. N. A. Malik, T. Dracos, and D. A. Papantoniou, "Particle tracking velocimetry in three-dimensional flows. 2. Particle tracking," Exp. Fluids **15**, 279–294 (1993).

53. G. Labonté, "New neural network for particle-tracking velocimetry," Exp. Fluids **26**, 340–346 (1999).

54. S. Kim and S. J. Lee, "Measurement of 3D laminar flow inside a micro-tube using micro digital holographic particle tracking velocimetry," J. Micromechanics Microengineering **17**, 2157–2162 (2007).

55. P. R. Bowden, J. D. Yeager, D. R. Guildenbecher, J. D. Olles, J. A. Hashem, and A. M. Schmalzer, "Characterizing the propensity of hypervelocity metal fragments to initiate plastic bonded explosives," in *Shock Compression of Condensed Matter* (AIP Publishing, 2017).

56. G. DR, O. JD, Y. JD, B. PR, and S. AM, "Characterization of hypervelocity fragments and subsequent HE initiation," in *16th International Detonation Symposium* (n.d.).

57. D. R. Guildenbecher, P. L. Reu, H. L. Stuaffacher, and T. Grasser, "Accurate measurement of out-of-plane particle displacement from the cross correlation of sequential digital in-line holograms," Opt. Lett. **38**, 4015 (2013).

58. D. R. Guildenbecher, L. Engvall, J. Gao, T. W. Grasser, P. L. Reu, and J. Chen, "Digital in-line holography to quantify secondary droplets from the impact of a single drop on a thin film," Exp. Fluids **55**, (2014).

59. O. Johannsen, C. Heinze, B. Goldluecke, and C. Perwaß, "On the calibration of focused plenoptic cameras," Lect. Notes Comput. Sci. (including Subser. Lect. Notes Artif. Intell. Lect. Notes Bioinformatics) **8200 LNCS**, 302–317 (2013).

60. D. G. Dansereau, O. Pizarro, and S. B. Williams, "Decoding, calibration and rectification for lenselet-based plenoptic cameras," Proc. IEEE Comput. Soc. Conf. Comput. Vis. Pattern Recognit. 1027–1034 (2013).

61. T. Svoboda, D. Martinec, and T. Pajdla, "A convenient multicamera self-calibration for virtual environments," PRESENCE Teleoperators Virtual Environ. **14**, 407–422 (2005).

62. V. Vaish, B. Wilburn, N. Joshi, and M. Levoy, "Using plane + parallax for calibrating dense camera arrays," Proc. 2004 IEEE Comput. Soc. Conf. Comput. Vis. Pattern Recognition, 2004. CVPR 2004. **1**, 2–9 (2004).

63. B. Wieneke, "Stereo-PIV using self-calibration on particle images," Exp. Fluids **39**, 267–280 (2005).

64. B. Wieneke, "Volume self-calibration for 3D particle image velocimetry," Exp. Fluids **45**, 549–556 (2008).

65. S. M. Soloff, R. J. Adrian, and Z.-C. Liu, "Distortion compensation for generalized stereoscopic particle image velocimetry," Meas. Sci. Technol. **8**, 1441–1454 (1997).

66. C. Bruecker, D. Hess, and B. B. Watz, "Volumetric Calibration Refinement using masked back projection and image correlation superposition," in *19th International Symposium on the Application of Laser and Imaging Techniques to Fluid Mechanics* (2018).

67. C. Heinze, S. Spyropoulos, S. Hussmann, S. Member, and C. Perwass, "Automated Robust Metric Calibration Algorithm for Multifocus Plenoptic Cameras," IEEE Trans. Instrum. Meas. **65**, 1197–1205 (2016).

68. N. Zeller, F. Quint, and U. Stilla, "Calibration and accuracy analysis of a focused plenoptic camera," ISPRS Ann. Photogramm. Remote Sens. Spat. Inf. Sci. **II–3**, 205–212 (2014).

69. N. Zeller, F. Quint, and U. Stilla, "Depth estimation and camera calibration of a focused plenoptic camera for visual odometry," ISPRS J. Photogramm. Remote Sens. **118**, 83–100 (2016).

70. K. H. Strobl and M. Lingenauber, "Stepwise calibration of focused plenoptic cameras,"

Comput. Vis. Image Underst. **145**, 140–147 (2016).

71. D. Cho, M. Lee, S. Kim, and Y. W. Tai, "Modeling the calibration pipeline of the lytro camera for high quality light-field image reconstruction," Proc. IEEE Int. Conf. Comput. Vis. 3280–3287 (2013).

72. D. R. Guildenbecher, J. Gao, P. L. Reu, and J. Chen, "Digital holography simulations and experiments to quantify the accuracy of 3D particle location and 2D sizing using a proposed hybrid method," Appl. Opt. **52**, 3791–3801 (2013).

73. E. A. Deem, Y. Zhang, L. N. Cattafesta, T. W. Fahringer, and B. S. Thurow, "On the resolution of plenoptic PIV," Meas. Sci. Technol. **27**, 084003 (2016).

74. M. Levoy, "Light field photography , microscopy , and illumination," in *International Optical Design Conference* (2010), pp. 6–8.

75. F. V Pepe, F. Di Lena, A. Mazzilli, G. Scarcelli, M. D. Angelo, M. Storico, R. Enrico, I.- Roma, S. Bari, and I.- Bari, "Diffraction-limited plenoptic imaging with correlated light," Cornell Univ. Libr. 1–8 (2017).

76. J. Gao, D. R. Guildenbecher, P. L. Reu, and J. Chen, "Uncertainty characterization of particle depth measurement using digital in-line holography and the hybrid method," Opt. Express **21**, 17512–17517 (2013).

77. T. Khanam, M. Nurur Rahman, A. Rajendran, V. Kariwala, and A. K. Asundi, "Accurate size measurement of needle-shaped particles using digital holography," Chem. Eng. Sci. **66**, 2699–2706 (2011).

78. E. M. Hall, T. W. Fahringer, and B. S. Thurow, "Volumetric calibration of a plenoptic camera," AIAA SciTech Forum, 55th Annu. Aerosp. Sci. Meet. 1–13 (2017).

79. E. M. Hall, D. R. Guildenbecher, and B. S. Thurow, "Uncertainty characterization of

particle location from refocused plenoptic images," Opt. Express **25**, 21801–21814 (2017).

80. N. Otsu, "A Threshold Selection Method from Gray-Level Histograms," IEEE Trans. Syst. Man. Cybern. **SMC-9**, 62–66 (1979).

81. J. C. Russ, *The Image Processing Handbook*, 4th editio (CRC Press LLC, 2002).

82. T. Fahringer, "On the Development of a Volumetric Velocimetry Technique using Multiple Plenoptic Cameras," Auburn University (2018).

83. R. Matsuoka, N. Shirai, K. Asonuma, M. Sone, N. Sudo, and H. Yokotsuka, "Measurement accuracy of center location of a circle by centroid method," Lect. Notes Comput. Sci. (including Subser. Lect. Notes Artif. Intell. Lect. Notes Bioinformatics) **6952 LNCS**, 297–308 (2011).

84. E. D. Munz, "A Comparison of Particle Tracking and Sizing Using Plenoptic Imaging and Digital In-line Holography," Auburn University (2016).

85. G. E. Cossali, M. Marengo, A. Coghe, and S. Zhdanov, "The role of time in single drop splash on thin film," Exp. Fluids **36**, 888–900 (2004).

86. D. R. Guildenbecher, J. D. Olles, T. J. Miller, P. L. Reu, J. D. Yeager, P. D. Bowden, and A. M. Schmalzer, "Characterization of hypervelocity fragments and subsequent HE initiation," in *16th International Deontonation Symposium* (2018).

87. A. M. Mellor, T. L. Boggs, J. Covino, C. W. Dickinson, D. Dreitzler, L. B. Thorn, R. B. Frey, P. W. Gibson, W. E. Roe, M. Kirshenbaum, and D. M. Mann, "Hazard initiation in solid rocket and gun propellants and explosives," Prog. Energy Combust. Sci. **14**, 213–244 (1988).

Appendix A: Thin lens plenoptic coordinate conversion

This appendix provides a detailed derivation of the relationship between the two plane parameterization of light field coordinates and object space coordinates based on thin lens assumptions. The derivation is based on the thin lens equation, and the plenoptic relationships defined in Chapters II and III. These relationships will be demonstrated independently in the depth and in-plane dimensions here, starting with the derivation of *z*, though of course the dimensions are related. First, the definition of magnification as a ratio of the image distance to the object distance, $M = l_i / l_o$, is substituted into the thin lens equation. This allows definition of the image distance, l_i and object distance l_o as,

$$l_i = f\left(1-M\right) \text{ and } l_o = f\left(1-\frac{1}{M}\right). \tag{28}$$

Then, consider the thin lens equation in terms of virtual image and object distances as,

$$\frac{1}{l_i'}+\frac{1}{l_o'}=\frac{1}{f}. \tag{29}$$

Substituting the definitions $l_i' = \alpha l_i$ and $l_o' = l_o + z$ into Equation (29) followed by substitution of Equations (28) results in,

$$\frac{1}{\alpha f\left(1-M\right)}+\frac{1}{f\left(1-\frac{1}{M}\right)+z}=\frac{1}{f}. \tag{30}$$

Finally solving for *z* and simplifying results in,

$$z = f\left[\frac{1}{M}+\frac{1}{\alpha(1-M)-1}\right]. \tag{31}$$

Moving on to the in-plane dimensions, first consider the definition of effective magnification, M_e, or the magnification at a given depth as,

$$M_e = \frac{-l_i'}{l_o'}. \tag{32}$$

Substituting the definitions of l_i and l_o,

$$M_e = \frac{-\alpha l_i}{l_o + z}. \tag{33}$$

Substituting Equations (28) and (31),

$$M_e = \frac{-\alpha f\left(1-M\right)}{f\left(1-\frac{1}{M}\right)+f\left(\frac{1}{M}+\frac{1}{\alpha(1-M)-1}\right)}. \tag{34}$$

Simplifying,

$$M_e = -\left(\alpha(1-M)-1\right). \tag{35}$$

Then based on the plenoptic geometry, x is defined s' scaled by the negative of the effective magnification M_e,

$$x = \frac{s'}{-M_e}. \tag{36}$$

Substituting the definition of s' and Equation (35) into Equation (36),

$$x = \frac{(s-u)\alpha - u}{\alpha(1-M)-1}. \tag{37}$$

A similar process can be followed for the y direction for a final complied relationship as given in Chapter III and repeated here for clarity,

$$(x,y,z) = \left(\frac{(s-u)\alpha+u}{\alpha(1-M)-1}, \frac{(t-v)\alpha+v}{\alpha(1-M)-1}, f\left[\frac{1}{M}+\frac{1}{\alpha(1-M)-1}\right]\right). \tag{38}$$

Appendix B: DLFC guide

This appendix details the implementation of DLFC in an experimental system and is intended to serve as a guide for the future application of this volumetric calibration technique. The procedure can be divided into three stages: collection of experimental calibration data (calibration target images), determination of the calibration mapping function, and application of the mapping function to experimental data. These steps are described in the following subsections.

A. Calibration target image collection

The collection of volumetric calibration data involves the capture of images of a calibration target composed of a of a dot grid with known dimensions at various depths through the volume of interest. First, an appropriate dot card must be selected based on the experimental parameters, specifically, the desired volume dimensions. A dot card that allows at least 10 dots in the smallest dimension to be visible with the field of view with a recommended spacing between dots of at least two dot diameters is recommended. Each dot should have a diameter spanning several microlenses, Figure 97 shows a small region around a single dot from a raw calibration target image, in this case, the diameter of a dot was approximately six microlenses in image space. An example of the center perspective view created from a calibration image is shown in Figure 98. Note the presence of dot locators, in this case 3 hollow dots, which will allow consistent association of dots between images at different depths. The example here shows a dot grid printed on adhesive paper and attached to a flat plate, however, a variety of dot grid configurations can be used. The AFDL calibration tools support targets of black or white dot grids. Additionally, the use of a multilevel dot grid calibration target is supported, however, the examples in this appendix will demonstrate the use of a single level target.

Second, the calibration target must be mounted to allow precise placement of the dot card at depths throughout the volume of interest, only the volume within which calibration target images are captured can be reliably calibrated. The calibration target should be placed as close to the nominal focal plane as possible. Exact alignment is not necessary, however, note that the location of the dots will define the measurement volume. An example of the experimental configuration for volumetric calibration is given in the photos in Figure 99 which shows the calibration target mounted on a translation stage in front of a plenoptic camera. In the example case, LED lamps and diffusers used to ensure even illumination are also visible in the photos.

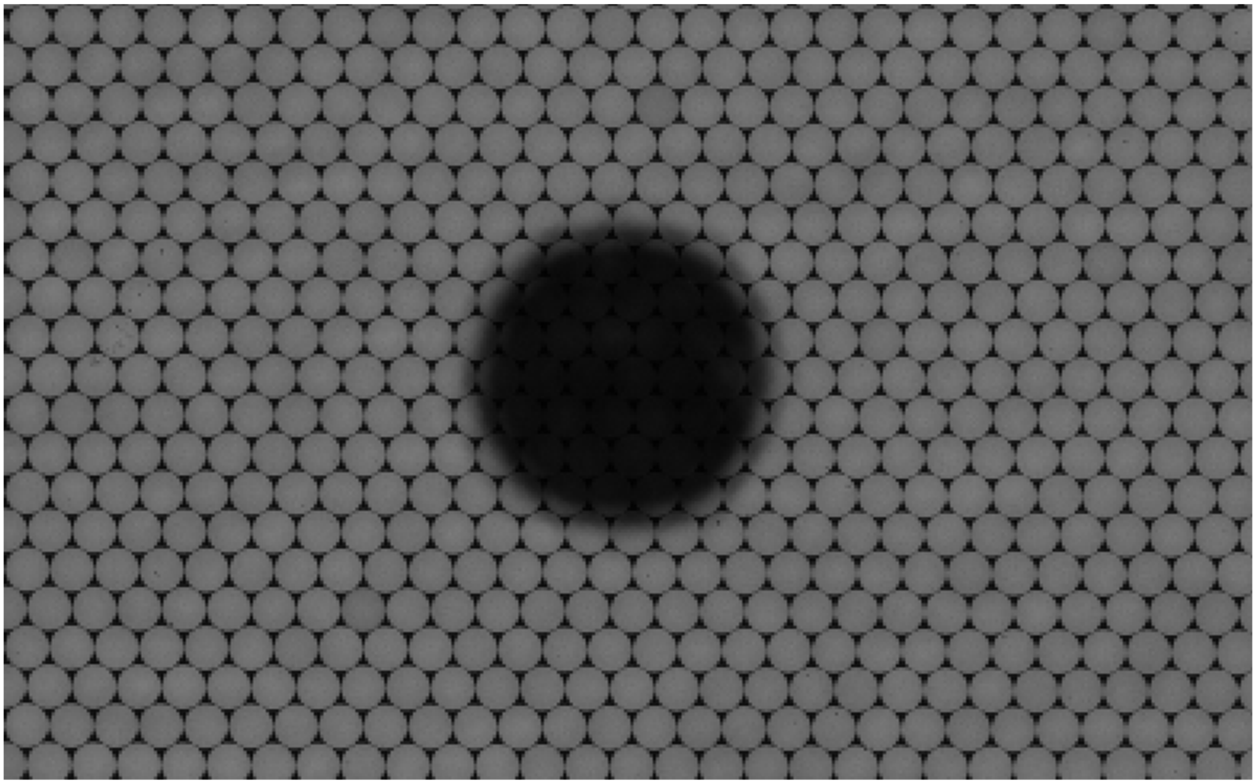

Figure 97. Portion of a raw calibration target image demonstrating the recommended dot diameter.

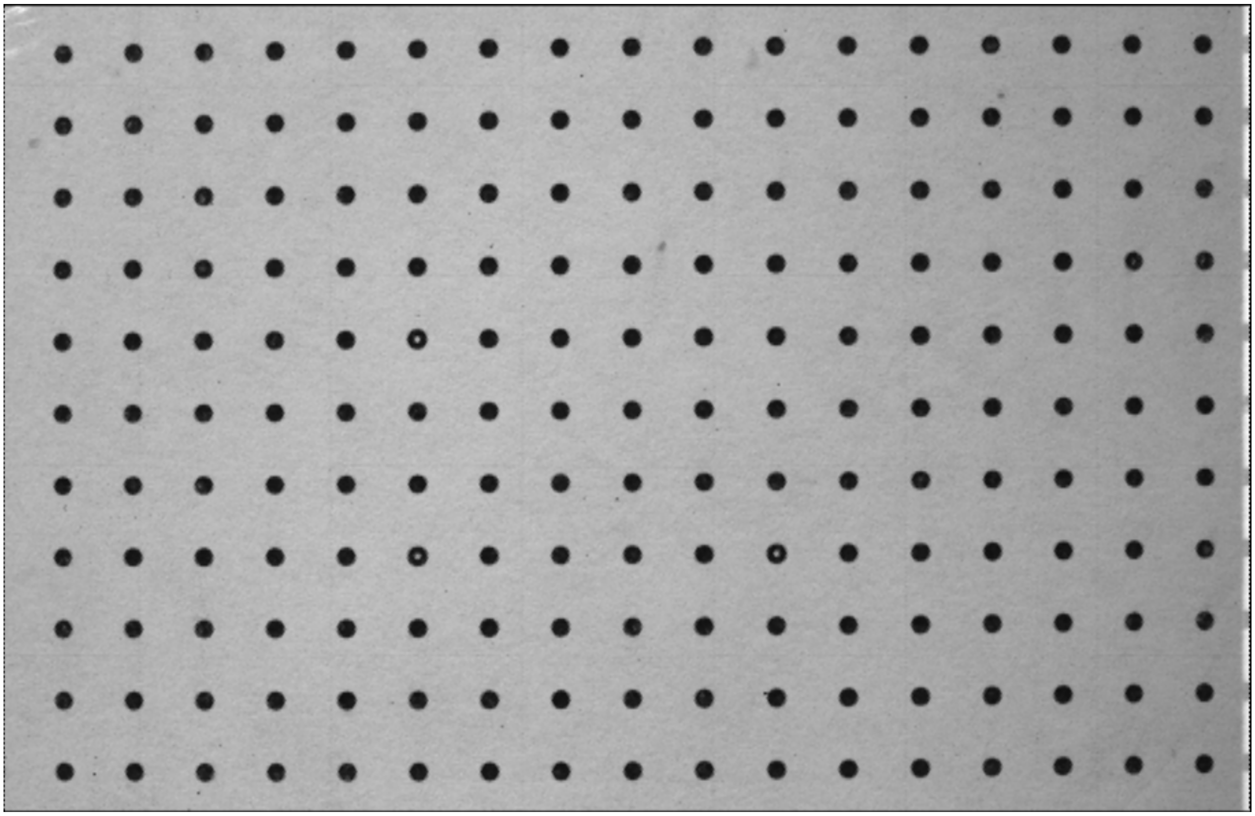

Figure 98. Example center perspective image from a calibration target image.

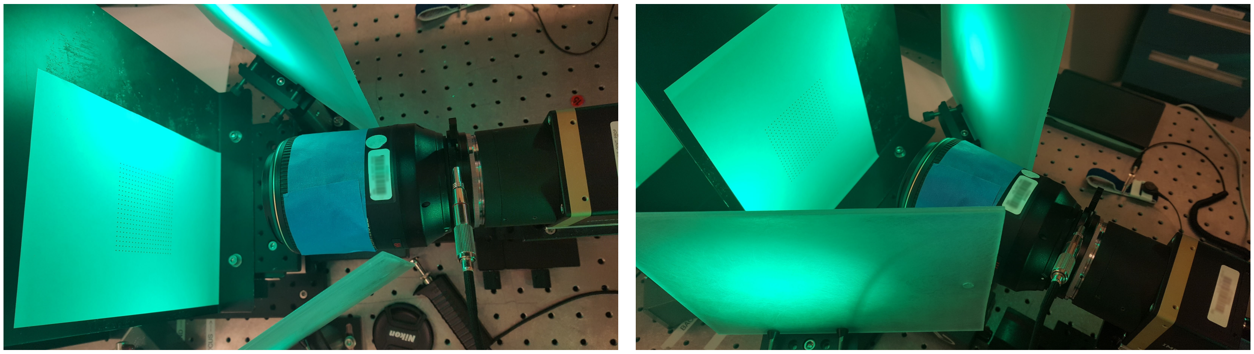

Figure 99. Experimental configuration photos depicting a calibration target mounted on a translation stage in front of a plenoptic camera.

Finally, images can be collected. Images should be captured with the dot card placed at a minimum of five depths, through 10 or more are recommended depending on the volume depth. The depth location at which each image is captured should be carefully recorded (preferably in the filename). Throughout the collection of images, care should be taken to ensure that the calibration target does not move except in the depth direction. The precision and accuracy of the dot card placement between each image will significantly affect the calibration quality.

B. Calibration mapping function

After the calibration target images are collected, the calibration mapping function must be determined. First, a range of perspective views of each dot card are created over a user defined range of views within the aperture. This range should be selected so that the dots can be clearly identified in all views, i.e., minimal vignetting. Note that the views that can be used to execute the perspective shift based particle location determination algorithm described in Chapter V is limited to the views that are used in creation of the calibration mapping function.

Next, the dot locations must be identified in each perspective view at each depth and control points must be selected by the user to correctly associate dots between depths. At each depth, the user must select control points including a center (this must be the same dot in each image and will become (0,0) of the calibration defined coordinate system) and four corner points (these are used to determine an expected dot spacing and can be different points at difference depths if necessary, but the user must also input the number of spacing intervals between the selected dots). The perspective view images are then thresholded and MATLAB region finding tools are used to determine the dot positions. The measured positions are then organized into the dot grid based on the user input center and corner dot locations. The dot positions and the user defined known physical spacing between dots is used to define the superpixel pitch, or the physical size represented by a pixel in a perspective view. The calculated value is a single estimate, however, the size does vary spatially throughout the 3D volume measured.

Finally, these values are used to form the transformation matrix as described in Chapter III Section B Subsection iii and the calibration coefficients are determined using a least squares fit.

The calibration mapping function can be mathematically satisfied by a number of dot card images one greater than the order of the calibration function (i.e., a third order fit can be produced using four depth planes), however, in practice this generally results a rank deficient transformation matrix solution as the use of the least squares procedure relies on an overdetermined system.

C. Application to experimental data

The application of the mapping function to an experimental data set is implemented in different ways depending on the desired output. In general, the coefficients relate positions on the microlens and aperture planes (encoded in the raw image) to 3D positions in objects space. In the calculation of a focal stack the coefficients are used to determine the appropriate (s,t) locations in a raw image from which to extract intensity data to form a volumetrically calibrated focal stack. In the determination of particle position from perspective shifted images the use of the DLFC coefficients is more directly integrated into the processing algorithm. The coefficients are used both to triangulate the 3D position of each particle from positions in a range of (uncalibrated) perspective views and to create a refocused image from which the in-plane size and shape of each particle is determined.

Appendix C: Perspective shift algorithm code reference

This appendix provides a detailed description of the MATLAB implementation of the perspective shift algorithm developed in this work and is intended to allow the reader to successfully use the code as well and make modifications or reimplement segments of the method as necessary. Use of this algorithm requires the PerspectiveDLFC code set as well as the open source LFIT code set. The first section describes the required and user adjustable optional input parameters including appropriate use and expected effect. The following sections provide pseudocode describing the operation of each function.

A. Required inputs and user adjustable optional input parameters

The only required user inputs are the filenames of the data, output, and calibration information as described in Table 9. The creation of the calibration files is described in the LFIT documentation [34] and DLFC code.

Table 9. Required inputs in perspective shift algorithm.

Input	Description
dataImageFilename	The filename of the raw plenoptic image to be processed
outputFilename	The filename where the resulting particle locations and other information will be saved
calSettingsFilename	The filename where the microlens calibration information is located (expects LFIT settings format)
coefficientFilename	The filename where the DLFC coefficients are located
superpixelFilename	The filename where the superpixel pitch is located

Due to the wide range of particle characteristics for which this code is intended to be used, a relatively large number of adjustable parameters have been included using the MATLAB ‘input parser’ functionality. For many data sets, it may be reasonable to use the default settings provided, however, for the more complex data set (or advanced user) adjustment of these additional parameters may be useful. Table 10 provides a list, the default values, and a description of each parameter.

Table 10. User adjustable parameters available in perspective shift algorithm.

Parameter	Default value	Description
zLim	[-25 25]	The minimum and maximum depth bounds in which a particle can be located (mm)
samples1D	11	Diameter of perspective views included in measurement, must be an odd integer, circular aperture region is used (i.e., only views with a (*u*,*v*) magnitude of <samples1D/2 are included)
radii	[0.01 2]	Minimum and maximum allowable particle radius, determination based on area (mm)
F	105	Estimate of main lens focal length, used in determination of acceptable cluster diameters
Fnum	4	Estimate of main lens f#, used in determination of acceptable cluster diameters
eccentricity	[0 0.8]	Minimum and maximum allowable eccentricity of particles, the default range generally performs well when spherical particles are expected
thresholdWindow	100	The window size applied in the averaging filter used in the segmentation of perspective views
numClusterPlanes	10	The number of planes at which clustering is executed
minNumViews	10	The minimum number of views in which a particle must be located to be considered valid, it is useful to raise this value to > half the number of possible views in data sets with problematic overlapping

restrictShape	[Inf Inf]	Restricts the allowable deviation between particle images in a cluster [area, eccentricity], input as decimal percent, defaults do not place any limit on shape similarity
backgroundNormalization	'No'	Indicates if background normalization of perspective views will be executed, input is the background image filename if affirmative

B. General overview: processImage.m

This is a wrapper function used to implement the entire perspective shift particle location algorithm starting from a raw image and resulting in 3D particle positions and in-plane parameters as in Table 11.

Table 11. Pseudocode: processImage.m.

```
define input parameters
load calibration files
call calcDataPerspectives.m
if backgroundNormalization = affirmative
    call calcDataPerspectives.m for background image and normalize data perspective
end if
call findParticleImages.m
while unassigned ($u$,$v$,$s$,$t$) exist and particles have been added
    call sortMeasured.m
    call calcParticles.m
    call calcConfidence.m
    call addParticleImages.m
end while
save particle parameters to file
```

i. Calculation of perspective images: calcDataPerspectives.m

This function calculates a range of perspective shifted images using the information in the calibration settings file and the input samples1D. This function is used for creation of perspective views from both data images and background images if required. The creation of individual perspective views within this function uses LFIT.

ii. Identification of particle images: findParticleImages.m

This function measures the locations of all particles in all views based on intensity thresholding resulting in a list of (u,v,s_m,t_m), or the measured light field coordinates of all identified centroids as in Table 12.

Table 12. Pseudocode: findParticleImages.m.

```
for each perspective view
    threshold perspective view
    find regions of connected pixels
    remove regions not meeting eccentricity and radius limitations
end for
```

iii. Clustering of particle images: sortMeasured.m

This function sorts the overall list of (u,v,s_m,t_m) particle image centroids into groups, each for an identified particle by executing *k*-means clustering at a range of depths within the volume of interest as in Table 13.

Table 13. Pseudocode: sortMeasured.m.

```
calculate cluster diameter limits
while not all cluster planes have been examined & some $(u,v,s_m,t_m)$ are unassigned
    project all $(u,v,s_m,t_m)$ to the current cluster plane
    execute clustering with $k$ = max(number of particles in a single view)
    accept as particles any clusters with a diameter < current plane diameter limit
    move to the next cluster plane
end while
if overlapping particles may remain
```

```
    for 1: max(number of particles in a single view)
        $k = k + 1$
        while not all cluster planes have been examined & some $(u,v,s_m,t_m)$ are unassigned
            project all $(u,v,s_m,t_m)$ to the current cluster plane
            execute clustering with $k$
            accept as particles any clusters with a diameter < current plane diameter limit
            move to the next cluster plane
        end while
    end for
end if
for each of the identified particles
    identify any clusters that have been assigned multiple particle image from 1 view
    remove repeated particle images
end for
if there are size and shape restrictions
    for each of the identified particles
        find the median area and eccentricity of all assigned particle images
        calculate minimum and maximum allowable area and eccentricity
        remove any particle images outside restrictions
    end for
end if
find the number of views in which each of the identified particles is located
delete particles with < minimum required number of views
```

iv. Triangulation of 3D positions: calcParticles.m

This function uses the DLFC coefficient mapping and the list of (u,v,s_m,t_m) coordinates iteratively (to allow removal of substandard measurements) for each particle to determine the (x,y,z) positions as in Table 14.

Table 14. Pseudocode: calcParticles.m.

```
for each of the identified particles
    while the maximum discrepancy between measured and calculated $(s,t)$ > allowable
        solve DLFC mapping in a non-linear sense to find $(x,y,z)$ from $(u,v,s_m,t_m)$
        solve DLFC mapping directly to find $(u,v,s_c,t_c)$ from $(x,y,z)$
        find discrepancies between measured and calculated $(s,t)$
    end while
end for
```

v. *Calculate particle confidence: calcConfidence.m*

This function calculates a confidence value for each of the identified particles based on the number of views in which the particle is identified and the magnitude of the discrepancies between the measured and calculated light filed coordinates. Particles identified in more views and with smaller discrepancy magnitudes result in higher confidence values.

vi. *Add missing particle images and in-plane determinations: addParticleImages.m*

This function examines the existing particle measurements and searches any remaining unassigned (u,v,s_m,t_m) for additional measurements of these particles. Then, a modified version of refocusing is used to determine the in-plane characteristics of the particle as in Table 15.

Table 15. Pseudocode: addParticleImages.m.

```
for each of the identified particles
    identify which (if any) views the particle was not identified in
    while some particle images are missing & some have been added
        find expected coordinates of missing particle images
        determine if any of the unassigned particle images are within an allowable radius of the
            applicable expected coordinates
        add any identified missing particle images
```

```
    end while
    recalculate particle confidence
    determine bounding region for particle shape
    calculate refocused image in bounding regions at measured depth using applicable views
        threshold refocused segment
    define binarized region as particle and calculate shape parameters
end for
```